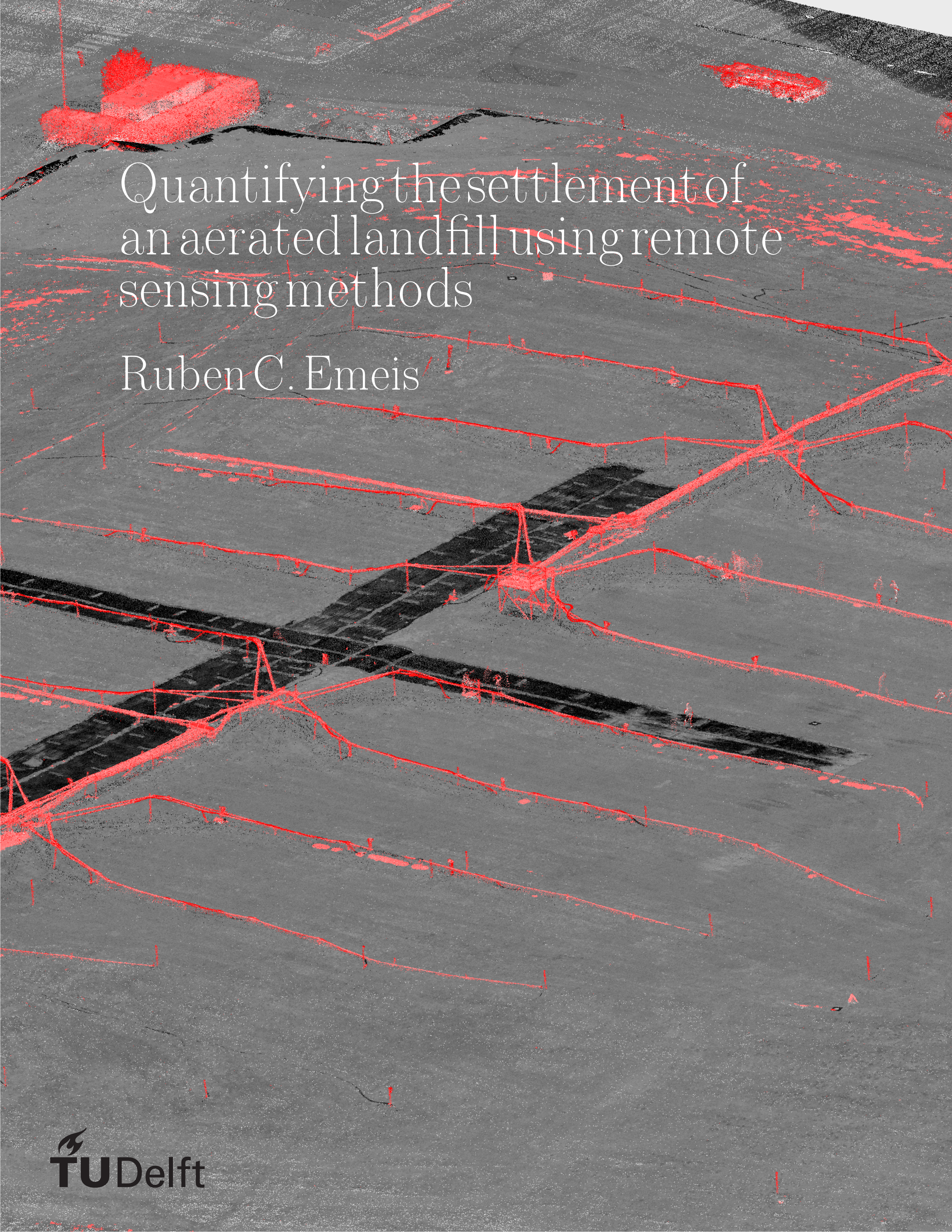

Quantifying the settlement of an aerated landfill using remote sensing methods

Ruben C. Emeis

TU Delft

Quantifying the settlement of an aerated landfill using remote sensing methods

by

Ruben C. Emeis

to obtain the degree of Master of Science

at the Delft University of Technology,

to be defended publicly on August 26th, 2022 at 11:00.

Student number:	4598563	
Project duration:	January 17th, 2022 – August 26th, 2022	
Thesis committee:	Dr. J. Gebert,	TU Delft, chair
	Dr. R.C. Lindenbergh,	TU Delft, supervisor
	Ing. H. Kramer	Wageningen Environmental Research (WENR), supervisor
	Dr. Ir. S. Mücher	Wageningen Environmental Research (WENR)

An electronic version of this thesis is available at http://repository.tudelft.nl/.

Cover image from cloth simulation filter applied to 2022 ALS data.

TUDelft

Preface

This master thesis represents the final product of my master studies at the Geo-Engineering section of the TU Delft. When facing the difficult decision of choosing my master track I was torn between Geo-Engineering and Geoscience & Remote Sensing. Whilst Geo-Engineering came out on top, I have always maintained my interest in the field of remote sensing. This thesis therefore was an amazing opportunity to bridge the gap between the two fields and spend 8 months working in both. I am immensely grateful to close my time at the TU Delft with a research that fit my interests so well. It also provided the opportunity to work with the CURE project, allowing me to contribute to the fight against climate change by reducing landfill emissions.

I would like to sincerely thank my supervisors Julia, Roderik, Henk and Sander for their time, energy and continued support during this study, the guidance I received from them was invaluable. Julia was deeply involved throughout the research and was always there to offer kind support or necessary feedback. She swept me up in her enthusiasm for landfills, something I did not held possible! Roderik allowed me to hit the ground running by partaking in his course on surveying, providing structure to the uncertain first months of research. Henk and Sander gave valuable insights into remote sensing processes, helping me utilise the data to its fullest extent.

Furthermore I would like to thank the academic staff and fellow students from the CURE project and OLRS research group. They helped both academically as well as socially. The weekly meetings helped maintain structure and provided distraction from the sometimes lonesome research work. I want to thank Nathali Meza Ramos, Cristhian Andrade Corona, Firat Pulat, and Linh Truong-Hong in particular for their efforts in improving my thesis. My gratitude goes to Carmen Cruz, Hans Lammen and Dennis van den Helder from Afvalzorg for their assistance and knowledge on the Wieringermeer landfill. Hans van der Marel helped me numerous times with the handling of the GNSS devices, as well as the subsequent processing, something I could not have done alone.

Last but not least I would like to thank the ones I hold dear for supporting me through this sometimes arduous process, both in the cheerful and stressful times. I could not have done it without them.

Ruben C. Emeis
Delft, August 2022

Abstract

As part of the Dutch sustainable landfill project iDS, two compartments of the Dutch landfill Wieringermeer have been treated by in-situ aeration since 2017. The chosen method of aeration is over-extraction, where suction pressure is created causing ambient air to intrude into the landfill. Aeration induces enhanced settlement due to the acceleration of aerobic degradation of the waste. The aeration infrastructure comprises 110 wells, separated by around 10 to 15 m, covering an area of approximately 5 ha. This study analysed the spatial and temporal variability of settlement of the landfill, and aimed to correlate this with the carbon extracted by the wells. In order to quantify the settlement of the landfill various remote sensing methods have been utilised and compared. The methods include an Aerial Laser Scanner (ALS), Terrestrial Laser Scanner (TLS) and Global Navigation Satellite System (GNSS) measurements from a rover. In total 11 GNSS surveys, 4 TLS point clouds, and 2 ALS point clouds were available to this study.

Ground settlement plates have been measured using the GNSS rover since the start of aeration, showing a maximum settlement of $\sim$1.17 m on the western slope from August 2017 to June 2022. The slopes of the landfill experience more settlement than the top of the landfill, as a plate installed on the top only experienced $\sim$ 0.09 m over this same time period. This is due to the increased surface area of the landfill exposed to the outside air at the slopes. The UAV-based ALS and TLS point clouds were able to measure spatial and temporal variations in settlement. Whereas the trends in settlement are consistent between the methods, the absolute values show notable variance. The ALS and TLS data contain significant uncertainty due to the effect of vegetation on the landfill, to which this variance can almost entirely be attributed. At its peak the vegetation contributed to a difference of 0.95 m in settlement, compared to the GNSS measured settlement. Several processing steps were taken to help negate the effect, but these were not able to fully filter vegetation out. ALS data was impacted to a lesser extent due to the high angle of incidence of its laser signals as it flies overhead, because of this the signals generally penetrated the vegetation to a deeper depth than the TLS.

The aeration wells extracted 2583 tonnes of carbon from August 2017 to March 2022. Both visually and through the Pearson Correlation Coefficient clear correlations were observed between the variability of settlement and carbon extraction by the wells. The highest correlation coefficient reached was 0.503 using GNSS and gas data from August 2021 to March 2022, signifying a strong correlation.

Contents

1 Introduction **1**
1.1 Research relevance . . . 1
1.1.1 Project iDS & CURE . . . 2
1.2 Research aim . . . 3
1.3 Research questions . . . 4
1.4 Research outline . . . 5

2 Background **6**
2.1 Study Site: Pilot Landfill Wieringermeer . . . 6
2.2 Landfill Aeration . . . 8
2.2.1 Monitoring the landfill . . . 9
2.2.2 Emission Testing Value . . . 10
2.3 Biodegradation . . . 11
2.3.1 Settlement Mechanics . . . 12
2.4 Remote Sensing Methods . . . 14
2.4.1 Global Navigation Satellite System (GNSS) . . . 14
2.4.2 Photogrammetry . . . 15
2.4.3 Light Detection and Ranging (LiDAR) . . . 15
2.4.3.1 Intensity . . . 16
2.4.3.2 Terrestrial Laser Scan (TLS) . . . 17
2.4.3.3 Aerial Laser Scanning (ALS) . . . 18

3 Description of data **20**
3.1 Global Navigation Satellite System (GNSS) . . . 21
3.2 Terrestrial Laser Scan (TLS) . . . 23
3.3 Aerial Laser Scan (ALS) . . . 24
3.3.1 Actueel Hoogtebestand Nederland . . . 24
3.3.2 Riegl . . . 24
3.4 Gas flow and composition . . . 26
3.5 Historical . . . 26

4 Methodology **28**
4.1 Pre-processing . . . 28
4.1.1 Conversion and subsampling . . . 28
4.1.2 Registration . . . 28
4.2 Terrain extraction . . . 30
4.2.1 Cloth Simulation Filter . . . 30
4.2.2 Rasterize . . . 32
4.3 Settlement Analysis . . . 32
4.4 Gas measurements . . . 33

4.4.1 Extracted carbon 33
4.4.2 Comparison with settlement 34

5 Results **38**
5.1 GNSS measurements on settlement plates 38
5.2 Registration 43
5.3 Comparison of acquisition methods 48
5.3.1 Elevation obtained from method 57
5.4 Settlement from LiDAR 62
5.4.1 Comparing GNSS against LiDAR settlement 70
5.5 Settlement and carbon extraction correlation 73

6 Discussion **81**
6.1 GNSS discrepancy 81
6.2 Registration 81
6.3 Acquisition methods 82
6.3.1 Elevation obtained from method 83
6.4 Settlement from LiDAR 83
6.5 Settlement correlation to carbon extraction 84

7 Conclusions and recommendations **85**
7.1 Conclusions 85
7.1.1 Sub-questions 85
7.2 General conclusion 87
7.3 Recommendations 89

A Photographs **95**

B Tables **100**

C Figures **104**

Nomenclature

Abbreviations

ALS	Aerial Laser Scanner
CC	CloudCompare
CSF	Cloth Simulation Filter
CSR	Coordinate Reference System
CSV	Comma-Separated Value
CURE	Coupled Multi-process Research for Reducing Landfill Emissions
DOC	Dissolved Organic Carbon
DOM	Dissolved Organic Matter
DSM	Digital Surface Model
DTM	Digital Terrain Model
ETV	Emission Testing Value
GCP	Ground Control Point
GIS	Geographic Information System
GLONASS	Global'naya Navigatsionnaya Sputnikovaya Sistema
GNSS	Global Navigation Satellite System
GPS	Global Positioning Service
HDPE	High Density Polyethylene
HHE	Human Health and the Environment
iDS	Dutch Sustainable Landfill Management Project
IDW	Inverse Distance Weighting
IMU	Inertial Measurement Unit
IPCC	Intergovernmental Panel on Climate Change

ISL	Iterative Surface Lowering
LFG	Landfill Gas
LiDAR	Light Detection and Ranging
MSW	Municipal Solid Waste
ppm	Parts per million
PTDF	Progressive TIN Densification Filtering
PTD	Progressive TIN Densification
RGB	Red, Green, Blue
RINEX	Receiver Independent Exchange Format
RMSE	Root Mean Square Error
RTK	Real Time Kinematic
SDS	Sustainable Landfill Foundation
TIN	Triangulated Irregular Network
TLS	Terrestrial Laser Scanner
TOF	Time-of-Flight
UARSF	Unmanned Aerial Remote Sensing Facility
UAV	Unmanned Arial Vehicle
WUR	Wageningen University and Research

1 Introduction

1.1 Research relevance

As IPCC (Intergovernmental Panel on Climate Change) Chair Hoesung Lee (2022) so strongly said: "We are at a crossroads. The decisions we make now can secure a liveable future. We have the tools and know-how required to limit warming". Limiting global warming will require actions in nearly all aspects of life. To limit warming to around 1.5 °C global greenhouse gas emissions need to peak before 2025 at the latest, and be reduced by 43% by 2030. Simultaneously methane emissions need to be reduced by about a third (Lwasa et al., 2022).

Methane (CH_4) has a global warming potential of 28 to 36, over a time period of a 100 years (EPA, 2021). As such it is no great surprise that methane has accounted for roughly 30% of global warming since pre-industrial times (Legg, 2021). Globally, in 2019 waste contributed 68 megatons of methane emissions annually. This comes in at nearly 18% of all methane originating from human activity (IEA, 2021). Reducing the emission potential of waste will be a significant step towards mitigating global temperature change and therefore should be investigated.

Besides the global implications of emissions from waste, there are also local ones. According to the most recent Klimaatnota, a paper from the Dutch government outlining the progress made towards achieving the goals set out in the European Green Deal, the Netherlands is at risk of falling short of the goal of a net 49% CO_2 reduction by 2030 (Rijksoverheid, 2021). In 2018 methane emissions of landfills in the Netherlands amounted to 1.3% of the total CO_2 equivalent emissions (Table 1), thus reducing landfill emissions might help in reaching the CO_2 reduction goal (Ruyssenaars et al., 2020).

Table 1: Overview of emissions from the Waste sector, by Ruyssenaars et al. (2020).

Category	**1990**	**2017**	**2018**	**Contribution to total in 2018 (%)**
	Emissions in Tg CO_2 equivalent			**(by total CO_2 eq)**
Waste (total)	14.2	3.1	3.0	1.6%
Managed Waste Disposal on Land	13.7	2.6	2.5	1.3%
Biological treatment of solid waste	0.0	0.2	0.2	0.1%
Wastewater treatment and discharge	0.5	0.3	0.3	0.2%
National Total GHG emissions	221.7	193.3	188.2	

Whilst waste mass can be reduced and recovered through recycling or composting, only 19% of global waste mass undergoes materials recovery. The rest is either incinerated (11%), openly dumped (37%) or disposed of in some type of landfill (37%). Even high-income countries are only able to recover around one-third of their waste (Silpa et al., 2018). Waste that is landfilled retains its emission potential, compared to when it is either recovered or incinerated. Where the emission potential is the total amount of emissions that can still be released from the waste in the form of Landfill Gas (LFG) and contaminants in the leachate.

Next to emissions, there is also the issue of eternal aftercare of landfills. After closure, the waste landfills must be managed and controlled to avoid negative effects on Human Health and the Environment (HHE). Once authorities deem the landfill to no longer be a danger to HHE the aftercare may end. But as it stands eternal aftercare is required for Dutch landfills. However, landfill operators may operate at a loss and introduce the risk that they may not be able to fulfil the financial obligations for closure and aftercare (Scharff, 2014). If landfill services stop being profitable, the burden will be shifted to society by the state having to take responsibility for the continued operation of aftercare. To avoid this, landfills need to be stabilised so that eternal aftercare is no longer a requisite.

A study performed by Laner et al. (2011) reviews a range of approaches for the long-term management of these landfills. The paper argues that whilst the use of landfills is decreasing globally, there still are thousands of landfills operating that will close within the next 10-30 years. These are in addition to the thousands of already closed landfills. This presents a global issue that is currently being managed locally, with significant variations in waste treatment and aftercare. A transparent and consistent set of procedures for defining the desired state of a landfill at the end of aftercare needs to be developed.

1.1.1 Project iDS & CURE

In 2010 the Dutch Sustainable Landfill Management Project (iDS) was established by the Sustainable Landfill Foundation (SDS) along with the Dutch Ministry of Infrastructure and the Environment. The project aims to create finite aftercare for landfills, i.e. by stabilising the landfill mass. The iDS has received interest from abroad as they are aiming to provide the answer to this issue in the framework of modern legislation (The Sustainable Landfill Foundation, 2022). The project encompasses three landfill stabilisation projects, plus various supportive research projects to understand and predict field results. The landfill operators, Afvalzorg and Attero, are supported by SDS. SDS has contracts with researchers to provide scientific guidance, or to investigate specific applied topics. All parties share and exchange data related to the projects.

As part of the core research team of iDS, TU Delft jointly launched project CURE (Coupled Multi-process Research for Reducing Landfill Emissions). It is a multi-institutional project that contributes to iDS and focuses on developing fundamental insights into landfill processes. This will deepen the understanding of the inner processes and allow for feasibility studies into waste body stabilisation methods. To achieve this an extensive monitoring campaign has been organised too gather as much information as possible. It is funded by NWO Open Competitie ENW – GROOT, totalling €2.5 million (Webredactie CITG, 2020).

The iDS is divided into 2 phases. First in 2010 an inventory was made of existing relevant frameworks for assessing soil pollution, then a computational model was drawn up from the existing standards to determine the effect of leaching of substances from waste on the soil and groundwater (The Sustainable Landfill Foundation, 2022). In the second phase (2011-2014) a method was constructed to derive the emission testing values (ETVs) and three lists of landfill-specific proposed ETVs were made.

In 2014 the Dutch Government stimulated a full scale, ten year long, research program on the three pilot landfills. The focus of the program is to develop innovative techniques to reduce the emission potential and decrease the eternal after-care effort (Kattenberg et al., 2013). The Dutch Government was unable to launch the research program until it was assured the program had full public support. This support was achieved by following the main recommendations of a 2011 report by Kattenberg and Heimovaara (2011), namely to invest in creating a level playing field for all involved parties and to provide them with accurate and timely information and scientific analyses. The 10 year period of active treatment of the landfills began officially in 2016.

1.2 Research aim

The aim of this research is to quantify the settlement of a full-scale landfill. As part of iDS the Wieringermeer landfill is actively aerated to accelerate biodegradation. The enhanced biodegradation leads to increased settlement rates, which is monitored using three remote sensing methods. The data from a Terrestrial Laser Scanner (TLS), UAV-based ALS (Unmanned Aerial Vehicle, Aerial Laser Scanner) and GNSS (Global Navigation Satellite System) rover are combined and compared. Using these methods a best estimate of the settlement is made, whilst also comparing the methods between one another. Settlement data shall then be combined with measured waste degradation in the observation period to analyse the correlations between one another.

1.3 Research questions

The main research question of this study is as follows:

"To what extent can 3D remote sensing be used to measure the settlement and degradation of organic material in a landfill over time?"

Supported by the following hypothesis:

"The degradation of waste due to forced aeration enhances settlement of the landfill, this settlement can be measured using remote sensing techniques and linked back to waste degradation."

To answer the main question, the following sub-questions are addressed:

1. *What is the impact of factors such as vegetation and method uncertainty on retrieving the settlement quantified using UAV-based LiDAR, Terrestrial Laser Scanning, and GNSS receiver surveys?*

   Hypothesis: Method uncertainty and outside factors such as vegetation can either be corrected for, or be filtered out, as to make the landfill settlement retrievable.

2. *What are the differences between the LiDAR UAV and Terrestrial Laser Scan measurements, and how do these affect the uncertainty?*

   Hypothesis: Both methods have their own distinct characteristics, which translate into differences in accuracy of the extracted settlement.

3. *How does the settlement in the Wieringermeer landfill vary spatially and temporally?*

   Hypothesis: In the available surveying time series there are spatial and temporal variations in the settlement of the landfill.

4. *What spatial and temporal correlations exist between the variability of settlement and carbon extraction data?*

   Hypothesis: There is a statistically significant correlation between the variability of settlement and degradation of waste organic matter, reflected by extracted carbon.

1.4 Research outline

Chapter 2 provids an overview of the background behind this thesis, such as relevant theories related to the settlement of the landfill and more information on the remote sensing techniques utilised. In Chapter 3 a detailed overview is given of what data was available for use during this thesis, and any relevant characteristics of this data. Then in Chapter 4 the specific data processing methods used in this thesis are described in detail. Chapter 5 contains a description of the results which are discussed upon in Chapter 6. Finally the conclusions and recommendations are given in Chapter 7.

The performed work includes, but is not limited to:

1. Four field measurement campaigns to the Wieringermeer landfill to collect additional data. Three campaigns were focused on GNSS measurements, the fourth consisted of GNSS measurements as well as scans by a Riegl RiCOPTER LiDAR UAV and Leica P40 TLS.

2. An analysis and comparison of the point clouds generated by the Riegl UAV and Leica TLS. This data is also compared to GNSS data retrieved using RTK rovers.

3. Assessing the settlement of the landfill using the three aforementioned data sources. This was partially done during the TU Delft course CIE4614: 3D Surveying of Civil and Offshore Infrastructure.

4. The settlement is combined with known waste degradation data stemming from a 110 gas wells present on the landfill to analyse for potential correlations.

2 Background

This chapter introduces the study area in Section 2.1, after which the remediation measure applied to the landfill is explained in Section 2.2. Section 2.3 covers the theory behind the degradation of the waste within the landfill, as well as the mechanics behind settlement (Subsection 2.3.1). Finally Section 2.4 goes over all the remote sensing methods utilised in this thesis, with Subsection 2.4.1 covering the global satellite system and Subsection 2.4.3 the several laser-based systems used, as well as the underlying principles.

2.1 Study Site: Pilot Landfill Wieringermeer

Medemblik is a Dutch town located in the province North-Holland, next to which lies the Wieringermeer landfill under the care of Afvalzorg. Wieringermeer is one of the three pilot landfills of iDS. Afvalzorg takes care of the storage, recycling, recovery and landfilling of waste materials in the Dutch waste sector. For this location they are responsible for the aftercare of the landfill.

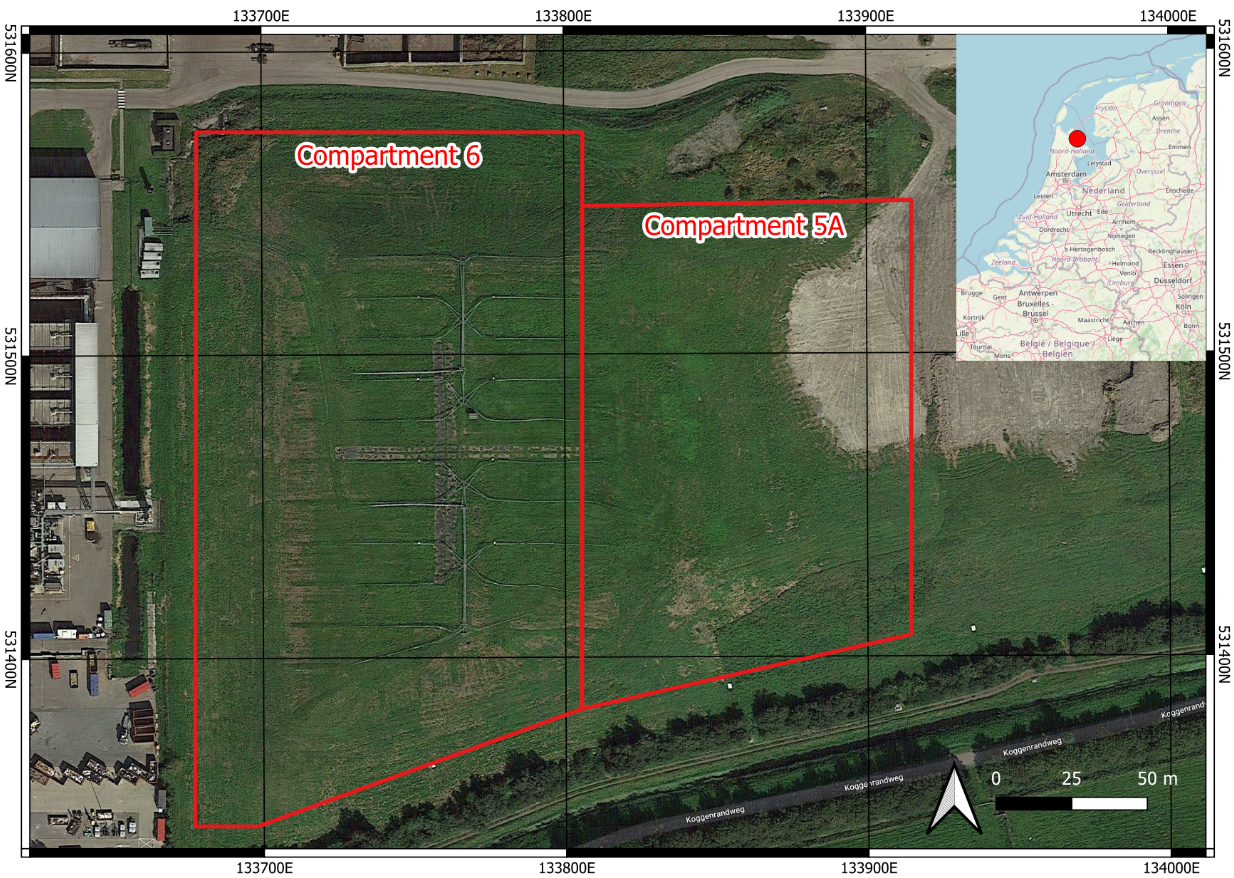

Figure 2.1: Aerial image of pilot landfill Wieringermeer with waste compartments marked. The network of lines present in compartment 6 is the aeration infrastructure that will be covered in Subsection 2.2.

The landfill was constructed with a bottom sealing layer comprised of 2 mm HDPE (High Density Polyethylene) foil (Oonk, 2012), on top of which the waste was deposited. The iDS project at the location Wieringermeer is focused on compartments 5a and 6 of the landfill. These compartments lack a top sealing layer to allow for rainwater infiltration, and instead have a layer of cover soil that is 1 to 1.5 meters thick. Compartment 6 totals 2.6 ha (26,000 m^2), contains 281,083 tons of waste and is the main area of study (Table 2). Compartment 6 was chosen as it only contained one leachate collection pit, and was therefore easy to disconnect from the leachate collection system of the rest of the landfill. Leachate is defined as any contaminated liquid that is generated from water percolating through a solid waste disposal site by contaminants (Cheremisinoff, 1997).

Table 2: Contents of the landfill compartments in tons (Vereniging Afvalbedrijven, 2014).

Waste type	**Compartment 6**	**Compartment 5a**
Contaminated soil	6,450	78,497
Construction and demolition waste	8,900	53,237
Industrial waste	201,772	99,925
Shredder waste	650	5,583
Household waste	2,300	15,227
Sludge and composting waste	61,011	15,938
Total	281,083	268,407

The part of the landfill under study was filled in the period 1992-2003 by mostly company, construction and demolition waste in addition to soil cleaning residues. The remaining amount of biodegradable material is limited. A feasibility study specific to this landfill was released in 2009 by van Meeteren et al. (2009b), which includes a current status report, a preliminary design and cost-estimate of the technical measures. Subsequently in 2014 a report was released containing a worked out final plan of action, describing in detail all the planned activities and how these are to be realised (Vereniging Afvalbedrijven, 2014). The experiment is to last 10 years at this site, with an evaluation after 5 years based on which changes may be made to the method of aeration.

The geometry of the landfill is visible in Figure 2.2. The flat top of the landfill is bordered by slopes on three sides in the compartments of interest (6 and 5A), westward of compartment 5A the flat top of the landfill continues. The aeration infrastructure seen in Figure 2.1 has been marked by a red arrow.

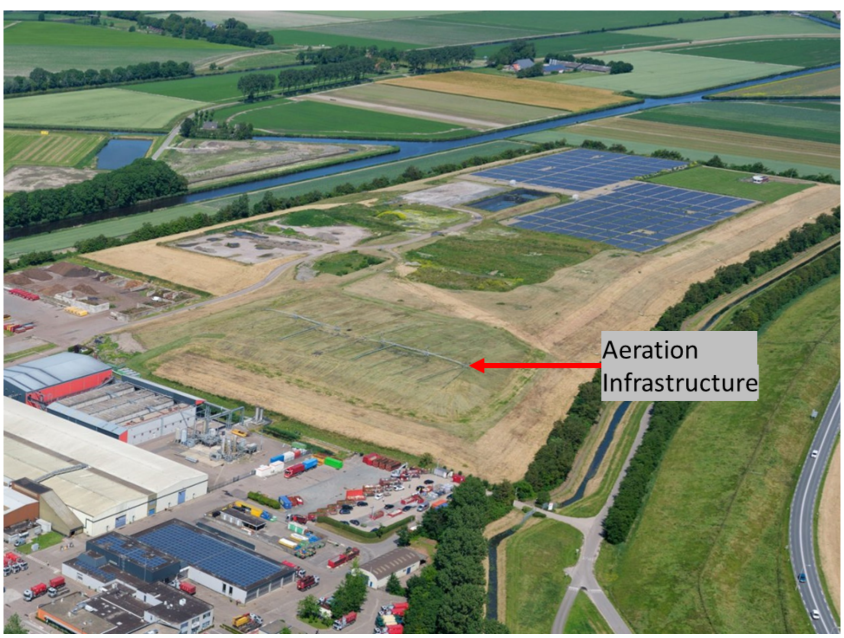

Figure 2.2: Side on perspective of the Wieringermeer landfill, image taken from the SW direction by Afvalzorg.

2.2 Landfill Aeration

By introducing aeration, the process of circulating air through a liquid or substance (in this case waste), biodegradation of organic matter is accelerated up, methane production reduces, and the removal of ammonia-nitrogen is enhanced (Agdag and Sponza, 2004). Two types of in-situ aeration systems are being piloted in the Netherlands, overextraction and injection-extraction. The decision was made to implement overextraction at the Wieringermeer landfill, which works by drawing air into the unsealed cover layer of the landfill through gas wells and extracting the LFG generated by the waste body. Injection-extraction applies the same principle except here air is injected into the landfill, instead of merely infiltrating through the cover layer. The extracted LFG is then either burned by an onsite flare, stored or treated by a bio-filter that converts methane to carbon dioxide using bacteria.

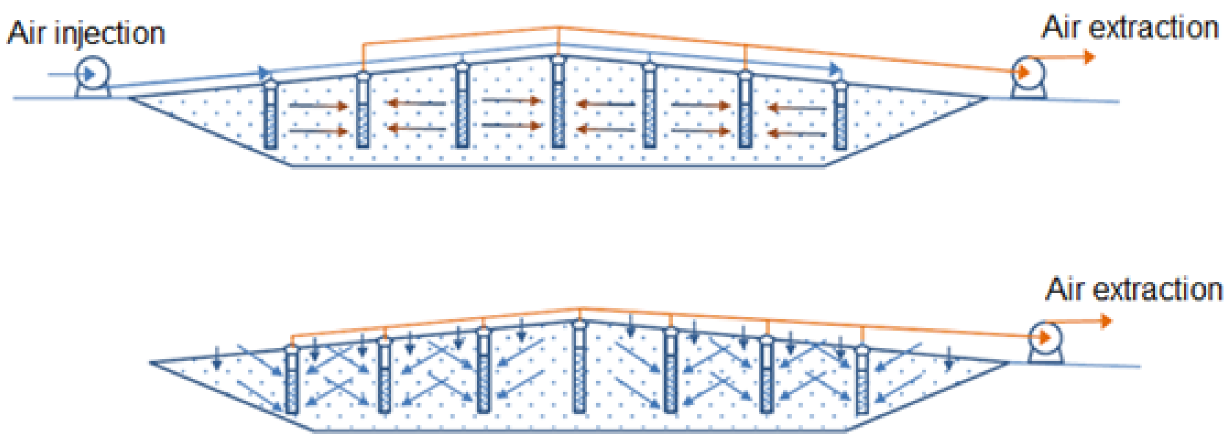

Figure 2.3: Schematisation of aeration strategies, injection-extraction (top) and overextraction (bottom) (Vereniging Afvalbedrijven, 2015).

By introducing oxygen the aerobic decomposition of the waste is enhanced, reducing the emission potential of both the LFG and of contaminants within the leachate. When organic material degrades Dissolved Organic Carbon (DOC) is generated, which in turn can mobilize heavy metals and organic contaminants (Rajammal, 2009). The metals and contaminants leech into the leachate, requiring it to be treated as to prevent these from entering the groundwater. Furthermore, the time required to decrease the landfill emission potential of the landfill is reduced. The distinction between aerobic and anaerobic decomposition will be further explained in Subsection 2.3.

Aeration is more than simply injecting or extracting air. Well design and spacing, selection of air volume and pressure, control of air distribution, temperature and moisture as well as the potential mobilisation of pollutants in the gaseous and liquid phases have to be considered (Ritzkowski and Stegmann, 2012). As such the aeration system has to be altered for each landfill, depending on characteristics such as the permeability of the waste body and water content.

As the Wieringermeer landfill was in an advanced stage of the methanogenic phase with less anaerobic degradable organic matter remaining, it was strongly recommended by the preliminary design report to directly start with in situ aeration (Meza, 2021). Compartment 5a is partially included in the aeration as it is adjacent to compartment 6 and therefore may introduce edge effects if left untouched. Aerating the entire landfill was not deemed financially achievable (Vereniging Afvalbedrijven, 2014).

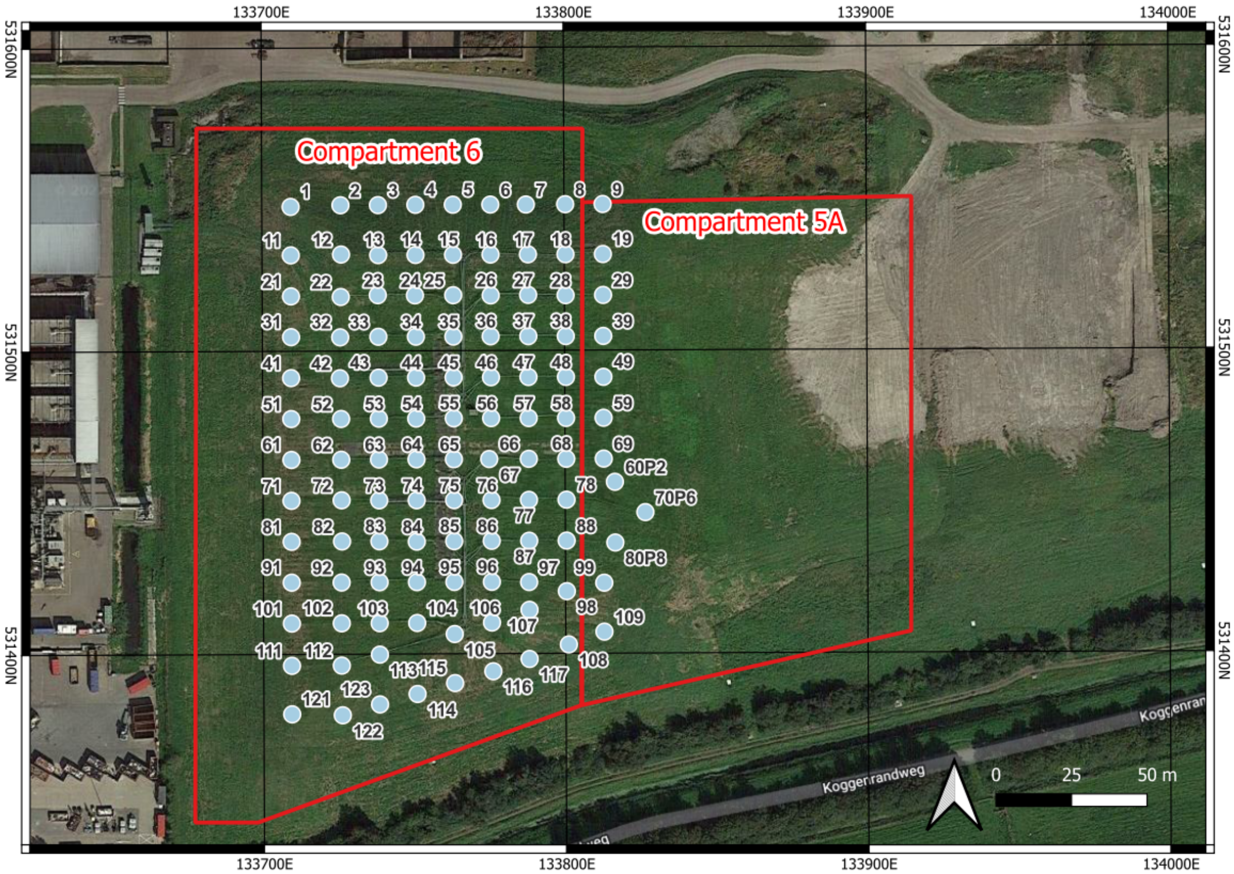

Figure 2.4: Map of gas well locations at the Wieringermeer landfill (red lines mark the compartments and the blue dots the gas well location).

The aeration through overextraction is realised by applying under pressure to the aeration wells, extracting gas from the waste package (Meza, 2021). The 110 wells consist of vertical tubes installed in the waste body, where the lower part is slotted. The wells are spaced around 10 to 15 m apart on a regular grid as shown in Figure 2.4, except for the southern most wells which follow the slope of the landfill. As more gas is extracted than the amount of LFG produced by the waste body, outside air is sucked into the body through the slots. The final, and implemented, design is based on a maximum flow rate of 1000 m^3 per hour, which was based on the landfill gas formation that was calculated in 2016. After the beginning of aeration the flow rate was decreased to approximately 400 m^3 per hour. From December 2019 onwards the flow rate was ramped up to a 100% capacity from 80%, bringing flow rates back to above 700 m^3 per hour (Meza, 2021).

2.2.1 Monitoring the landfill

To monitor the effectiveness of the stabilization measure applied a monitoring strategy is devised in a report by Vereniging Afvalbedrijven (2014). The leachate amount is continuously measured in the wells, and the composition and fraction DOC are analysed in a lab monthly and quarterly respectively. The groundwater composition is measured using piezometers according to the existing permits. The volume and composition of the produced gas was measured four times during the zero-measuremente, after which it is measured through the aeration wells and blower station. The gas measurements are explained in detail in Subsection 3.4. Settlement plates are installed to aide in monitoring the settlement of the landfill, these are covered in detail within Section 3.1. To assess the effectiveness of the infiltration and aeration additional testing is done using geoelectric and seismic measurements, tracer testing at the percolate collection, and gas traccer testing at the gas injection system. Finally, waste samples are analysed in a laboratory before and after the experiment.

2.2.2 Emission Testing Value

As a baseline, prior to any aeration and remediation measures taken, ETVs (Emission Testing Value) were determined that would result in an acceptable level of load on the local soil (Brand et al., 2014). As such there are value's for acceptable concentration levels of contaminants at the end of the 10 year experiment, location specific to Wieringermeer. If these ETVs can be reached the need for aftercare of the landfill is nullified, as these ETVs are based on the assumption that no waste insulating measures are in place. There are some conditions, namely that the bottom insulating seal must remain intact during the duration of the experiment. Next to this the leachate drainage system must be properly functioning during and after the experiment. The landfill emissions during the experiment must satisfy local air quality regulations, after the experiment it is not expected that the emissions will breach the local regulations (Brand et al., 2014).

2.3 Biodegradation

The organic matter within a landfill can be biodegraded by micro-organisms. Solid organic matter dissolves into soluble materials, and subsequently partially turns to biogas. Biogas is a mixture of methane and carbon dioxide. There are several processes which combine into the effect known as biodegradation, the solid organic materials (e.g. hemicellulose and cellulose) hydrolyse into soluble organic molecules, fermentation of organic acids and methanogenesis (Heimovaara et al., 2010). A hydrolysis reaction is a chemical reaction in which a molecule of water breaks chemical bonds (IUPAC, 2019), fermentation is a metabolic process through the action of enzymes, and methanogenesis is the final step in the anaerobic degradation of organic carbon (Vincent et al., 2021).

On the scale of a piece of waste, for instance a piece of wood, biodegradation can be seen as a reactive front which slowly eats through the biodegradable matter. Outer parts that degrade will open up the inner parts of the piece to further hydrolysis. The organic matter in waste can comprise of easily degradable components (sugars) up to slower or non degradable components (e.g. lignin and humic substances) (van Meeteren et al., 2009b). As such biodegradation is not a process that occurs at a constant speed, but is dependant on the composition of the waste and other parameters such as temperature and water content.

Water and air flows within the landfill drive or limit degradation. Methods to speed up biodegradation include adding supplemental water, or to recirculate leachate back into the waste (Benson et al., 2007). The increased moisture enhances the anaerobic degradation processes by the redistribution of substrates and nutrients, spreading of microorganisms, and the dilution of organic acids; which inhibit hydrolysis and methane production (Barlaz et al., 1990).

In aerobic conditions waste can rapidly decompose. Ritzkowski and Stegmann (2013) summarized the general aim of a landfill experiencing in situ aeration into four distinct goals. First, the methane formation potential of the landfill is to be reduced to the greatest possible extent. Second, is improving the leachate quality by reducing the emission of contaminants through the leachate. Third, the acceleration and completion of the main landfill settlements, easing further development of the landfill such as installing solar panels on top. Fourth and last, the creation of bio-stabilized landfills, ending expensive perpetual landfill aftercare, as explained in Section 1.1.

Although aeration causes a slight decrease in moisture content, it engendered lower leachate production, much lower methane concentration and a greater decrease in organic matter contents for both the organic solid waste and the leachate (Sang et al., 2008). Furthermore, oxygen inclusion can lead to oxidation of problematic compounds such as NH_4^+, which is non-reactive under anaerobic conditions (Bolyard and Reinhart, 2016). Oxidation can also lead to the immobilization of compounds that co-precipitate with oxidized dissolved organic matter (DOM) (van Turnhout et al., 2020).

Waste is considered completely biologically stabilized by Heimovaara et al. (2010) when all the organic material that is biodegradable under anaerobic conditions within is converted. As such complete biological stabilization does not mean the complete biodegradation of all organic matter in the waste following the reasoning from Heimovaara et al. (2010). In a Municipal Solid Waste (MSW) landfill, where the waste remains relatively dry, stabilization may take several hundred years (Hall et al., 2004). In a bioreactor landfill, stabilization can instead occur within decades (Reddy and Bogner, 2003). A different classification of landfill stabilization is linked to settlement and assumed to correspond to 99% of the potential degradation settlement having occurred. Thus, settlement may provide an indication to the level of stabilization of the landfill. This classification is a better fit for this study as it is focused on quantifying the settlement of the landfill.

2.3.1 Settlement Mechanics

The degree of biological stabilization of the landfill can be assessed using several methods, such as carbon balances, or LFG generation measurements. In addition, indirect parameters such as settlements can be used as indicators for the degree of stabilization and estimating how much further aeration of the waste body will be required.

Experiences from previous in situ aerated landfills show that the major part of settlement appears in the first 18 months of operation (Ritzkowski and Stegmann, 2013). When aeration is continued further significantly lower settlement rates occur, after this initial phase of high settlement the average values are assumed to be below 0.2% per year. (Ling et al., 1998)

Powrie et al. (2019) focused on the mechanisms behind settlement in municipal solid waste landfills, and also the phases at which they occur. The principal mechanisms of waste settlement from Powrie et al. (2019) are as follows:

1. Rearrangement of the solid matrix by sliding, reorientation or distortion of waste particles as vertical stresses are increased. This occurs either during compaction or as further material is deposited. If the waste is unsaturated or highly impermeable the settlement will occur nearly immediately on loading. Else, if the waste is saturated and of low permeability the process of consolidation occurs. The rate of settlement is then limited by the rate at which voids can reduce in volume, and thus at the rate at which pore water can escape.

2. Compression of the pore fluid. Normally, in conventional soil mechanics, pore water is viewed as incompressible. But as the pores may contain air or an air/water mix this effect must be considered.

3. The compression or crushing of waste particles, which depends on the composition of the waste.

4. Breakage of particles as stresses are increased, or softening of particle contacts on wetting which causes a loss of strength and/or structure.

5. Degradation of the material due to biological decomposition, and the physico-chemical processes of corrosion and oxidation of the waste in the longer term. The degradable material in the waste body is transformed into LFG and leachate. When the degraded waste matrix can no longer resist the applied stress settlement will occur. This mechanism is key to this study as an attempt will be made to correlate settlement to the LFG extracted by the aeration infrastructure.

6. Conventional mechanical creep, as in continuing settlement at constant effective stress. This is caused by erosion and sifting of the finer materials into voids in between the larger particles (identified as ravelling by Edi and Ranguette (1990), material moving into voids as a result of degradation, and continued plastic deformation (Leonard et al., 2000).

The mechanisms occur in three distinct phases, first an initial immediate compression occurs due to the compression or expulsion of air, and the compression or crushing of compressible particles (Powrie et al., 2019). Then consolidation causes settlement of the waste, governed by the hydraulic conductivity. In conventional soil mechanics this is termed primary settlement. Then settlement continues at a constant effective stress after consolidation has ceased and the pore pressures have reached hydraulic equilibrium. This continued settlement is caused by degradation and creep and is referred to as secondary settlement. Due to the age of the landfill being studied and measured settlement trends, as covered in Chapter 3, it is thought to be in the final phase.

The degradation induced waste settlement relationship is difficult to model as it depends on factors such as water content and the amount of degradable matter remaining. Accurately modelling this behaviour requires coupled models such as those bench marked by Bareither and Kwak (2015). A coupled approach allows the settlement and gas production rates to be linked to waste composition, water content, and operational regime (aeration, leachate). The parameters needed to run these models are obtained from laboratory testing and field experiments.

2.4 Remote Sensing Methods

2.4.1 Global Navigation Satellite System (GNSS)

Global Navigation Satellite System (GNSS) refers to a constellation of satellites that provide signals from space that transmit both positioning and timing data to receivers (The EU Space Programme, 2021). The GNSS receiver can subsequently use this data to determine its location. GNSS provides global coverage, operational systems include Europe's own Galileo system, the US's Global Positioning System (GPS), Russia's Global'naya Navigatsionnaya Sputnikovaya Sistema (GLONASS) and finally China's BeiDou Navigation Satellite System. Each of these systems have their own particular weak and strong points, but the reason so many independent systems exist is largely due to political and redundancy reasons (Winkless, 2016). If for example the US Department of Defense, who operates GPS satellites, decides to shut down GPS due to war or political turmoil most of the developed world would be severely impacted. Especially political adversaries such as China and Russia have a vested interest in developing their own independent satellite constellation. Both GNSS devices used for this study are capable of tracking GPS, GLONASS, Galileo and BeiDou satellites.

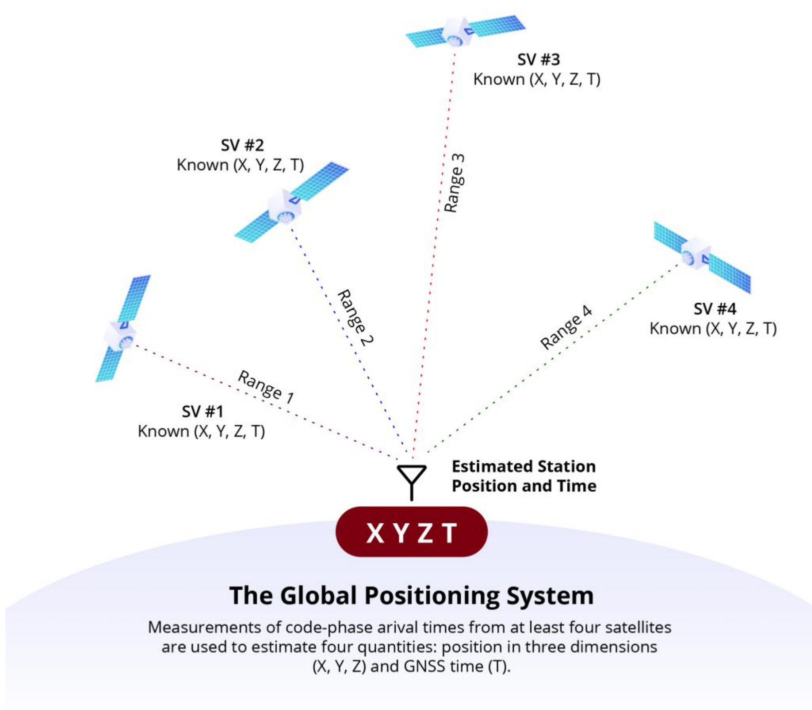

Figure 2.5: Illustration of a GNSS measurement (Tallysman, 2022). Four quantities are estimated, the position in three dimensions (X, Y, Z) and GNSS time (T). Four satellites are used, denoted as SV #1 through #4.

GNSS is based on the concept of trilateration, as illustrated in Figure 2.5. This is a method to determine the location of a stationary, or moving point in space using the ranges (distances) between the point and multiple spatially-separated known locations. The satellites within the constellation act as these known locations (Lee, 1973). First the range, r, is determined between the point (x, y) and both satellites (r_1 and r_2). U is the separation between the satellites.

$$\begin{aligned} r_1^2 &= x^2 + y^2 \\ r_2^2 &= (U - x)^2 + y^2 \end{aligned} \tag{2.1}$$

From there the x coordinate of the point can be determined,

$$x = \frac{r_1^2 - r_2^2 + U^2}{2U} \tag{2.2}$$

Note that with only two satellites there are two potential locations, as can be seen in equation 2.3. Adding a third satellite removes this ambiguity, whilst adding further satellites beyond the third help to add redundancy. Outlying measurements can be identified and then rejected using additional satellites, plus through averaging over more measurements the effect of slight errors can be reduced.

$$y = \pm\sqrt{r_1^2 - x^2} \tag{2.3}$$

2.4.2 Photogrammetry

A commonly used 3D remote sensing method, like LiDAR, is photogrammetry. Photogrammetry is a 3D coordinate measuring technique that uses photographs as the fundamental medium for metrology or measurement (Horswell, 2013). The fundamental principle on which the method is based is triangulation by taking photographs from at least two different locations, providing different lines of sight to the object. The lines of sight are mathematically intersected to produce the three-dimensional coordinates of the point of interest (Horswell, 2013). Photogrammetry has not been included in this thesis as 3D remote sensing method, as surveying with this method is less suited to working with areas of high vegetation. The landfill is in essence a grassy hill, where depending on the season and time since last mowing vegetation can reach up to a meter in height. LiDAR data is able to more accurately reflect the true ground surface in areas of dense vegetation, especially when the ground is invisible to photogrammetric operators (Gil et al., 2013).

2.4.3 Light Detection and Ranging (LiDAR)

LiDAR (Light Detection And Ranging) is a technology used to easily acquire spatial data, resulting in a point cloud. A point cloud is a set of discrete points in 3D space with an x-, y- and z- coordinate. Depending on the device used in addition to the coordinates the point can have an intensity value and number of returns. Numerous techniques have been developed to obtain 3D imagery, divided into three main categories: triangulation, time-of-flight (TOF), or interferometry (Vosselman and Maas, 2010). Triangulation relies on the spatial geometry between the source, target, and detector. TOF relies on the finiteness of the speed of flight and the ability to measure it. Interferometry is dependant on the ability of waves to interfere, such as light.

The TOF method relies on laser signals being reflected back to the laser scanner, and is the one utilised by the devices in this study. The reflected laser beam is detected by a sensor on the laser scanner (detector), together with the time since the original laser beam was emitted (timing module). The distance (R) of the object from which the laser beam bounced back is then simply half the measured time (t), multiplied by the speed at which the beam travels (c) (equation 2.4). As the landfill is not a solid surface, but is covered by vegetation at varying lengths the measurement scenario becomes more complex.

$$R = \frac{1}{2} \cdot c \cdot t \tag{2.4}$$

Theoretically, the distance measurement accuracy of TOF lasers is influenced by instrument mechanism, atmospheric conditions, scanning geometry (distance and incidence angle), and target surface properties (Soudarissanane et al., 2011). Note that the instrument mechanism is unchanged during the campaigns. However, differences may be observed when comparing different laser scanners. With the distance to the object and the known horizontal and vertical angle at which the measurement was taken, the point can be placed in a 3D space. Repeat this step thousands, or millions of times at different locations and angles and they will form a point cloud.

2.4.3.1 Intensity Besides the return time for discrete topography measurements, nearly all current laser scanning instruments simultaneously measure the power of the backscattered laser signal of each point and record it as an intensity value. The process is determined by the radar range equation (Equation 2.5), which describes the relationship between the transmitted and received signal power.

$$\mathrm{P_r} = \frac{\mathrm{P_t D_r^2}}{4\pi \mathrm{R}^4 \beta_\mathrm{t}^2} \eta_\mathrm{sys} \eta_\mathrm{atm} \sigma \tag{2.5}$$

where P_r, the received laser power, is a function of the transmitted power P_t, the receiver aperture diameter D_r, the distance between the sensor and target R, the width of the laser beam β_t, the system transmission factor η_sys, the atmospheric transmission factor η_atm, and the target cross-section σ. Considering that the data is collected by the same sensor all sensor-related factors (P_t, D_r, η_sys) can be assumed as constant during one campaign.

When performing a campaign on a homogeneous surface using the same sensor, assuming the instrumental effect is constant and atmospheric changes are negligible, the major changes in the intensity data will be caused by the scanning geometry (and target surface type) (Tan and Cheng, 2016). The effects of scanning geometry can be attributed to the incidence angle and distance (range), where based on the radar range equation the intensity is directly proportional to the cosine of the incidence angle, and inversely proportional to the range squared (Fang et al., 2015). Here the incidence angle is the angle between the beam propagation direction and surface orientation.

Lambert's cosine law has been widely employed in existing intensity correction applications. It provides a satisfactory estimation of light absorption modeling for rough surfaces, allowing for it to correct the incidence angle effect (Abed et al., 2012). Under the assumptions of a constant power emitted for each pulse, and under the conditions for Lambertian targets the laser range equation can be rewritten as (Pfeifer et al., 2007):

$$i = C \times \rho \times \cos\theta \times R^{-2} \tag{2.6}$$

where i is intensity and C is calculated using

$$\mathrm{C} = \mathrm{P_t D_r^2} \eta_{\mathrm{sys}}/4 \tag{2.7}$$

which is a constant parameter for a specific scanner. The backscattered optical power is converted to voltage and amplified internally in the system. It is then transformed into a digital number, intensity, a scaled integer value. Spectral information associated with surface properties can be sourced from the intensity value, such as the reflectance, roughness, moisture, brightness, and grain size of the scanned object (Tan and Cheng, 2016). Studies can adopt the intensity data as a major or complementary data source. Applications include visualization, segmentation, classification, and multi-temporal analysis.

Whilst you can not irrevocably state that e.g. a red brick has an intensity value of 2000, or grass 500. The values depend on the wavelengths of the LiDAR sensor. One can make comparative observations, such as that water absorbs infrared, thus wet or saturated ground will have lower intensity compared to unsaturated ground or soil. In this study intensity is used to create a color scale for the point clouds to better distinguish objects and structures.

2.4.3.2 Terrestrial Laser Scan (TLS) TLS data is collected from fixed-positioned tripods within the area of interest. The TLS rotates horizontally and vertically to provide full coverage of the surrounding area, reducing the need to reposition the tripod. A detailed 3D point cloud (x, y, z, intensity) is created based on the emitted pulses reflected from surfaces visible to the scanner. An object close to the scanner can thus occlude surfaces behind this object, this is known as the shadowing effect and causes a point cloud to be incomplete (Kankare, 2015), as illustrated in Figure 2.6.

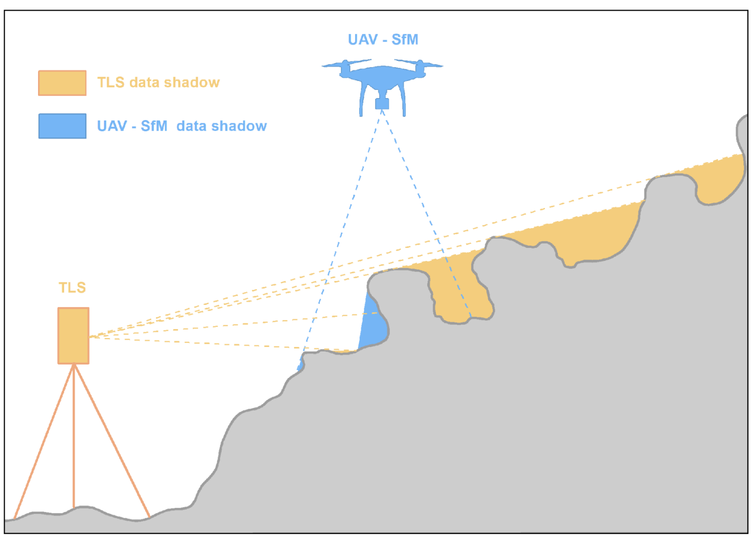

Figure 2.6: Viewing geometry and coverage of terrestrial laser scanning (TLS) and unmanned aerial laser scanning (structure from motion) from a single position (Šašak et al., 2019).

This effect is shown as gaps in data, behind occluded objects, as shown in Figure 2.7a. A remedy is to perform multiple scans of the area, which can be aligned to form one cohesive point cloud using artificial reference targets distributed over the target area, as shown in Figure 2.7b. This is called the registration process, where the point clouds to be registered are rotated and translated without changing the relative positions of points within them (Schrott et al., 2013).

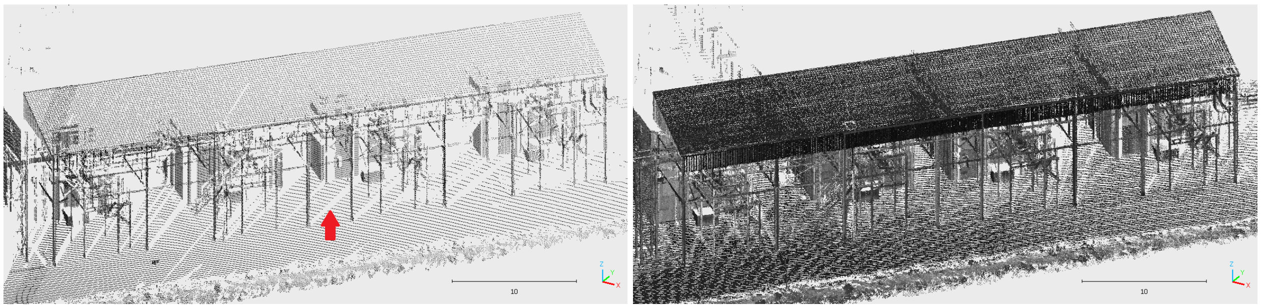

(a) Single-scan **(b)** Multi-scan

Figure 2.7: Example from Wieringermeer of stitching multiple scans to (partially) eliminate shadowing. The red arrow indicates shadowing behind some of the building's metal posts.

Point density is highest near the scanner position and decreases as a function of distance from the scanner due to surface area increasing at further distances, as seen in the inverse-square law.

2.4.3.3 Aerial Laser Scanning (ALS) Recent developments in ready-to-use drone systems have made it possible, and economically feasible, to mount LiDAR systems to Unmanned Aerial Vehicles (UAV's). They allow for high mapping speeds compared to surface-based methods such as TLS, whilst not boasting the enormous costs of airborne laser scanning using a manned aircraft. The UAV and scanner combination used for this study is classified as Aerial Laser Scanning.

The system consists of some critical components. At the center of any UAV platform is the system controller unit, which serves the same purpose as a motherboard and processor in a laptop or smartphone. Next there is a flight controller which connects the sensors to the motors. Sensors include a barometer for height, distance sensors for the detection of obstacles, and critically for mapping or scanning use an Inertial Measurement Unit (IMU) and/or GNSS device. Information from the sensors is also sent to the pilot, such as battery level, velocity, position and oftentimes the feed of a camera.

An IMU is responsible for determining the angular speed and acceleration of the UAV. The IMU works by detecting the rate of acceleration using accelerometers, and detects changes in the rotational attributes pitch, roll and yaw using gyroscopes. Higher end IMU's include a magnetometer to assist calibration against orientation drift (Corrigan, 2020). The data from the IMU is fed back to the flight controller which signals the electronic speed controllers which level of thrust is required from the motors to maintain the pilots input or preset flight path. The data from the IMU is also used to calculate its current position using the velocity. Depending on the size and complexity of the UAV it can be piloted by a smartphone, handheld controller, or ground station.

Using the IMU data, as well as data from GNSS antennas on the UAV, the flight trajectory is reconstructed. The trajectory and scanner mounting orientation are interpreted to produce the first point clouds, one per flight line (Brede et al., 2017). Across flight-line registration is done using tie-planes and overlap in between the individual flight lines, as seen in Figure 2.8 (note ALS data in figure not from Wieringermeer). When the study area lacks planar surfaces or other easily identifiable structures, ground control panels can be utilised as tie points to allow for fine registration. These panels are distributed across the study area and provide additional control surfaces. In addition these panels can be measured using a Real Time Kinematic (RTK) GNSS device for additional redundancy and validation.

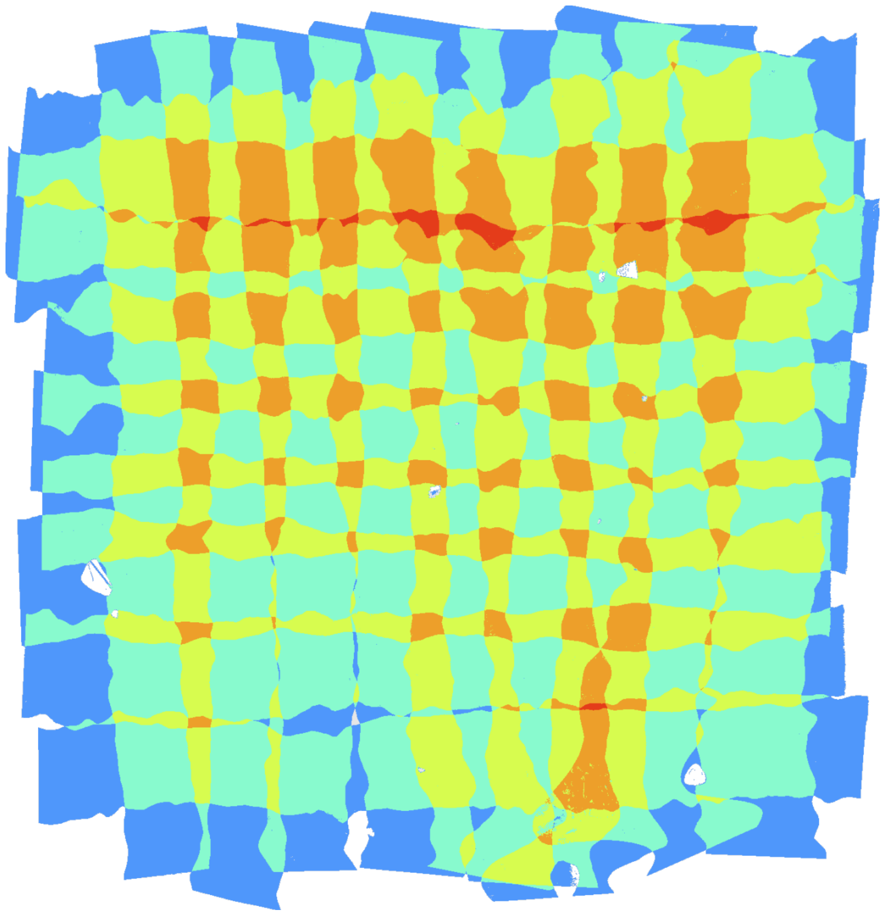

Figure 2.8: ALS flight strip overlap (Isenburg, 2022). The colours range from blue (no overlap) to red (the most overlap).

3 Description of data

The data of this study was retrieved during several field measurement campaigns at the Wieringermeer landfill. The majority of the GNSS measurements were performed by Afvalzorg, the landfill operator. The Terrestrial Laser Scanner, a Leica P40, is owned by TU Delft and for each of the four scans was operated by Dr. L. Truong-Hong, a member of the Optical and Laser Remote Sensing Group at the TU Delft department of Geoscience & Remote Sensing. The two UAV flights were performed by the Unmanned Aerial Remote Sensing Facility (WUR-UARSF), a shared facilities program of Wageningen University and Research (WUR). Figure 3.1 shows a graphical overview of all the available measurements, and their temporal distribution.

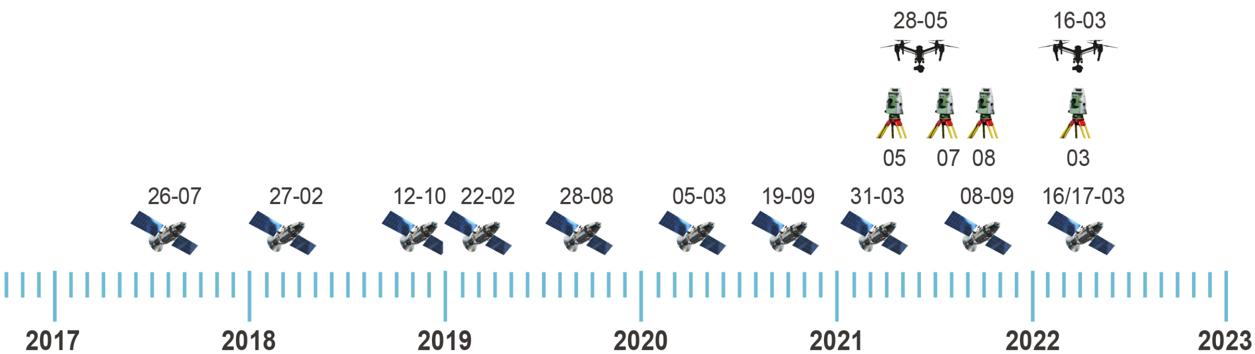

Figure 3.1: Timeline of the data available to this study (top: UAV-based LiDAR, middle: TLS, bottom: GNSS Rover). The TLS scans date from 28-05-2021, 09-07-2021, 18-08-2021, and 16-03-2022.

The following software tools were utilised to process and analyse the data, as described in Chapter 4:

1. CloudCompare (CC), an open-source software for registration and analysis of point cloud data. Version v2.12 beta, retrieved from https://cloudcompare.org. CloudCompare was heavily used in this study for the registration, processing and analysis (M3C2) of the point clouds.

2. QGIS, a user friendly open-source geographic information system (GIS) application. Version 3.24.1, retrieved from https://qgis.org/. QGIS was used for the generation of some maps and figures.

3. Python, using Spyder which is an open-source scientific environment for Python. Version 5.1.5 and Python 3.9.7, retrieved from https://www.spyder-ide.org/. A number of open-source packages and libraries were used, including but not limited to: Pyntcloud, GeoPandas, Shapely, SciPy, sklearn and PyKrige. The main use of Python within this study was for the Kriging interpolation and subsequent correlation calculations as described in Subsection 4.4.2.

4. Microsoft Excel, for its useful and convenient spreadsheet visualization and analysis tools. Excel was mainly used for processing the GNSS and gas well data.

3.1 Global Navigation Satellite System (GNSS)

The available GNSS information is comprised of data from two different devices. Afvalzorg operates a Stonex S10N GNSS to perform their routine survey. TU Delft performed three scans using a Trimble R8 Rover Receiver. Both of the utilised devices are capable of sub-centimeter precision, as can be seen in Table 3. Accuracy and reliability are subject to satellite geometry, atmospheric conditions and obstructions. The sub-centimeter precision ranges listed are only reached when a networked physical base station is present, a fixed base station sends out correctional data to a moving receiver. For the precision statistics *ppm* expresses a standardized measurement of error, in millimeters per 1,000 meters.

Table 3: Trimble R8 and Stonex S10N GNSS rover characteristics (Trimble, 2020)(Stonex, 2021).

Device Characteristics Trimble R8	
Precision Static Surveying (Horizontal)	3 mm + 0.1 ppm RMS
Precision Static Surveying (Vertical)	3.5 mm + 0.4 ppm RMS
Fixed RTK (Horizontal)	8mm + 0.5 ppm RMS
Fixed RTK (Vertical)	15 mm + 0.5 ppm RMS
Positioning rate	20 Hz
Device Characteristics Stonex S10N	
Precision Static Surveying (Horizontal)	2.5 mm + 0.1 ppm RMS
Precision Static Surveying (Vertical)	3.5 mm + 0.4 ppm RMS
Fixed RTK (Horizontal)	8mm + 0.8 ppm RMS
Fixed RTK (Vertical)	15 mm + 1 ppm RMS
Positioning rate	20 Hz

The GNSS devices were used to precisely measure the elevation of 28 ground settlement plates (Figure 3.3a) that were installed on the landfill in July 2017, these are anchored in place using a steel rod extending down into part of the waste body. Using the Trimble as example, the raw data from measurements are converted to RINEX (Receiver Independent Exchange Format) files. These are subsequently processed by the NETPOS processing service, which returns the cartesian X-, Y- and Z-coordinates in the ETRS89 coordinate system. Using web-based services these can then be converted to geographic coordinates (RD), and into heights with respect to NAP. The Stonex S10N surveyed these 28 points a total of 10 times, as shown in Figure 3.1. Besides the 10 sets of measurements from the Stonex S10N, the Trimble R8 was used to measure the settlement plates twice. In addition, during the final measurement campaign a Trimble R7 GNSS base was used for post-processing which will be further touched upon in Section 5.1.

Figure 3.2: Image of the Trimble R8 GNSS during fieldwork (06-06-2022).

(a) Settlement plates

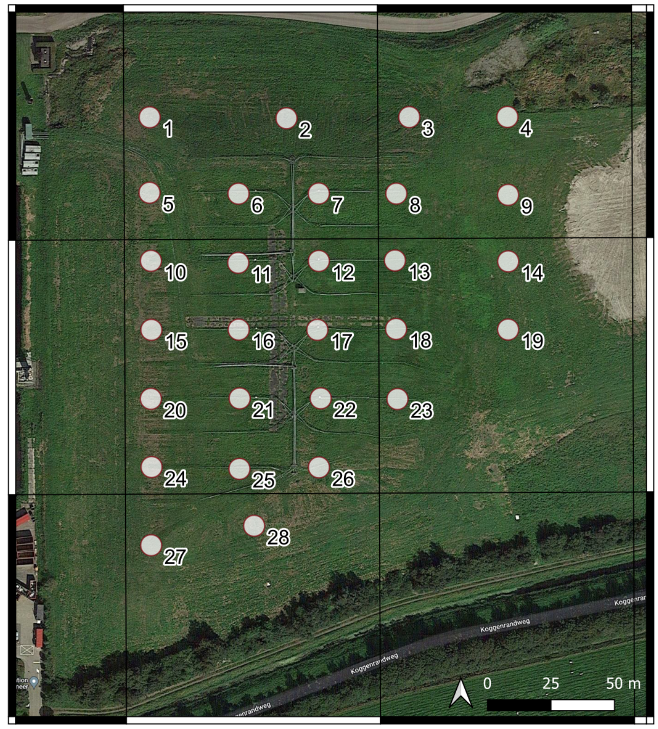

(b) Overview of settlement plates

Figure 3.3: Photograph of a settlement plate installed on the landfill and an aerial overview of all 28 plates.

In addition to the settlement plates a survey was performed as part of the course Environmental Geotechnics in December 2021. This survey measured each of the 114 gas wells present on the landfill using the Trimble R8. For these measurements some additional processing was required as the wellheads slightly extend out of the landfill. A total of 5 cm was removed to account for this, 10 wells had an additional 5 cm removed as there was an additional T-piece (T-shaped pipe connector) present. For further information on this refer to Section 5.5.

3.2 Terrestrial Laser Scan (TLS)

Data from a Leica P40 Terrestrial Laser Scanner is used, totalling four surveying campaigns of the landfill. The operator for each campaign was Dr. L. Truong-Hong from the TU Delft, who also processed the data. A surveying campaign is comprised of multiple scans that are 'stitched' together using the bundled Leica Cyclone 360 software package. For each scanner survey station three temporary Leica GZT21 HDS Black and White Scanning Targets were utilised to register single point clouds to the common coordinate framework. The Leica TLS survey can be characterized by a high point density, in the thousands of points per m^2 depending on the scanner settings and scanning geometry, and accuracy of the raster of measured points (Kovanič et al., 2020). The characteristics of the Leica scanner can be read from Table 4.

Table 4: Leica P40 laser scanner characteristics (Leica Geosystems, 2022).

Device Characteristics	
Distance System	Time-of-flight laser scanner
Scan Rate	Up to 1,000,000 points per second
Field of View	Horizontal - 360; Vertical 290
Accuracy	
Distance Measurement	1.2 mm + 10 ppm over full range
Target Acquisition	2 mm standard deviation at 50 m
3D Position	3 mm at 50 m; 6 mm at 100 m
Angular Measurement	8" horizontal; 8" vertical

An overview of the point clouds generated by the TLS can be seen in Table 5. Note that each of the point clouds have been downsampled, or subsampled. What this entails is the number of points is decreased, either sampled randomly or through some other method, to both decrease the file size and make it more suitable for running on consumer computer processors. Even very high end desktop computers with plenty of memory and cores may often experience crashes when running the point clouds at full size. In this case the 'spatial' mode built into CloudCompare is utilised , which picks points from the original point cloud so that in the output no point is closer to another point than the specified value (CloudCompare, 2015). A balance has to be found between performance gains and a loss of data, which was 50 mm as input of spatial subsampling for the TLS point clouds used. If a more powerful machine was available for this research then more points could have been preserved.

Table 5: Leica P40 produced point cloud information, supplied in the .laz format.

	Before downsampling		**After downsampling 50 mm**)	
	File size (GB)	Number of points	File size (GB)	Number of points
2021 May	4.359	171 Million	0.717	39 Million
2021 July	3.364	172 Million	0.796	51 Million
2021 August	4.243	217 Million	0.817	52 Million
2022 March	4.996	262 Million	0.977	62 Million

3.3 Aerial Laser Scan (ALS)

3.3.1 Actueel Hoogtebestand Nederland

The use of AHN (Actueel Hoogtebestand Nederland) data was considered as an additional source of settlement data. AHN is a digital height map of the Netherlands created by the Dutch water authorities, Rijkswaterstaat and provincial governments. The four AHN products (AHN1, AHN2, AHN3, and AHN4) are produced using ALS data that was retrieved by a small aeroplane. AHN1 is comprised of data ranging from 1996 to 2022, AHN2 from 2007 and 2012, and finally AHN3 from 2014 to 2019. Data acquisition for AHN4 started in 2020 and is as of 2022 nearly complete. It was decided that the error and standard deviation of the height data was such, that it obfuscated the settlement observed by other methods like the GNSS measurements, and thus was dropped from this study.

Table 6: AHN height characteristics (AHN, 2022).

	AHN1	**AHN2,3,4**
Systematic Error	5 cm	5 cm
Stochastic Error	15 cm	5 cm
Minimum 68.2% of points has a height accuracy within:	5 + 1 * 15 = 20 cm	5 + 1 * 5 = 10 cm
Minimum 95.4% of points has a height accuracy within:	5 + 2 * 15 = 35 cm	5 + 2 * 5 = 15 cm
Minimum 99.7% of points has a height accuracy within:	5 + 3 * 15 = 50 cm	5 + 3 * 5 = 20 cm

3.3.2 Riegl

An UAV operated by the Unmanned Aerial Remote Sensing Facility (WUR-UARSF) from Wageningen University performed two scans of the Wieringermeer landfill. The UAV platform used is a RIEGL RiCOPTER aircraft (Figure 3.4a); boasting a max operating altitude of 3000 meter, 30 minutes of flight time, 30 km/h of wind resistance and a max coverage of 100 ha per day. Mounted on the UAV is a lightweight and compact RIEGL VUX-SYS laser scanner (Figure 3.4b), its characteristics can be read from Table 7.

(a) RIEGL RiCOPTER

(b) RIEGL VUX-SYS (Image: Aeroscan)

Figure 3.4: UAV platform and laser scanner used to create 2 point clouds of the landfill.

First the laser scans are corrected using the built in IMU, as explained in Section 2.4.3.3. 06gps data, a GNSS correctional service, is used to correct the trajectory of the UAV using POSPAC. The corrected trajectory is then brought into RiPROCESS, where the flight strips are aligned either automatically or using

Table 7: RIEGL RiCOPTER UAV and VUX-SYS laser scanner characteristics (RIEGL, 2016).

Device Characteristics	
Distance System	Time-of-flight laser scanner
Scan Rate	350,000 points per second
Field of View	330 degrees downwards
IMU Accuracy	0.015 degrees Roll, Pitch. 0.035 degrees Heading
IMU Sampling Rate	200 Hz
Accuracy	
Max distance to target	550 m
Target Acquisition	Up to 10 mm accuracy
Position Accuracy	0.02 - 0.05 m

GCP's. In this study the data was aligned by manually locating and marking the GCP's in each flight strip. These GCP's are also used to correct the LiDAR data to the correct X- ,Y- and Z-position. The points are measured using a GNSS device such as the ones mentioned in Section 3.1, which is deemed more accurate than the measurements from the built in GNSS on the UAV. Figure 3.5 shows the processing pipeline of the RiCOPTER data.

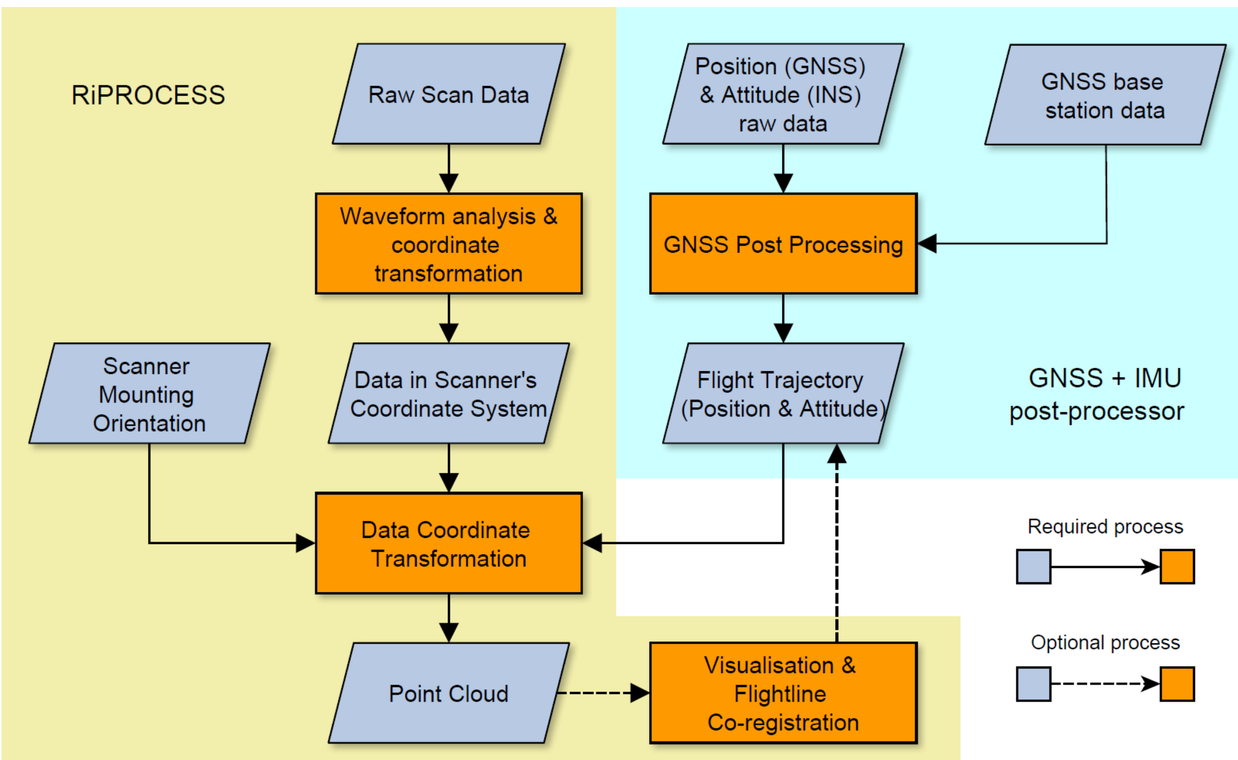

Figure 3.5: RiCOPTER processing flowchart from Brede et al. (2017).

An overview of the point clouds generated by the RIEGL UAV can be seen in Table 8. Two scans were performed by WUR-UARSF, one year apart from each other, with a final scan planned in spring 2023.

Table 8: RIEGL UAV produced point cloud information in the .e57 format.

Date	File size (GB)	Number of points
2021 May	0.650	110 Million
2022 March	0.835	105 Million

3.4 Gas flow and composition

The landfill is monitored through the 110 gas wells mentioned in Subsection 2.2. At each of these wells the volume percentages of $CH_4\%$, $CO_2\%$ and $O_2\%$, the gas velocity (m/s), pressure ($mbar$), and temperatures ($^{\circ}C$) are measured, as shown in Table 9. The measurements are performed on a monthly basis since 2017. The data for well 69 is not available, as such a 109 wells are utilised in this study.

Several devices were utilised:

1. A 'Geotech BIOGAS 5000 Portable Biogas Analyser' for gas compositions.
2. A 'Höntzsch U426 flowtherm Ex' for flux and temperature measurements.
3. A 'Blueline S4600 ST' for pressure measurements.

The gas velocity measurements are performed at each well. To convert these measurements to the flow rate the data from the gas blower station is used. The bulk flow rate at this station is measured on a 15-minute interval, separate from the manual monthly measurements of the gas velocity at each well. For more information on this conversion, and further steps performed on the data please refer to Subection 4.4.

Table 9: Excerpt of gas measurement data at each individual well (data from 09-01-2020).

				Gas composition			
Well-id	**P (mbar)**	**Flux (m/s)**	**T (C)**	**CH4%(9-1)**	**CO2%(9-1)**	**O2%(9-1)**	**Balance% (9-1)**
1	-35.4	0.4	12.0	7.0	21.6	0.5	70.9
2	-34.0	10.6	11.0	7.7	20.6	2.3	69.4
3	-35.5	1.3	11.0	10.8	22.9	0.3	66.0
4	-35.0	2.1	11.0	5.8	21.4	0.5	72.3
5	-34.0	10.3	10.5	16.6	25.7	0.8	56.9

3.5 Historical

Prior to the period of aeration the settlement of the landfill was already measured using settlement plates, however these are different plates than the set of 28 plates described in Section 3.1. The yearly measurements are from the period 2001-2008, in which the average settlement decreased from nearly 30 cm per year to around 6 cm per year (Vereniging Afvalbedrijven, 2014), as shown in Figure 3.7. The settlement was averaged over 17 plates, with 2 plates on compartment 6 spread over the entirety of the landfill. An additional 28 plates were installed in August 2012, with 9 on compartment 6. This set of plates was measured twice from August 2012 till January 2014 and it was found that the average yearly rate of settlement had further decreased to around 2.5 cm per year.

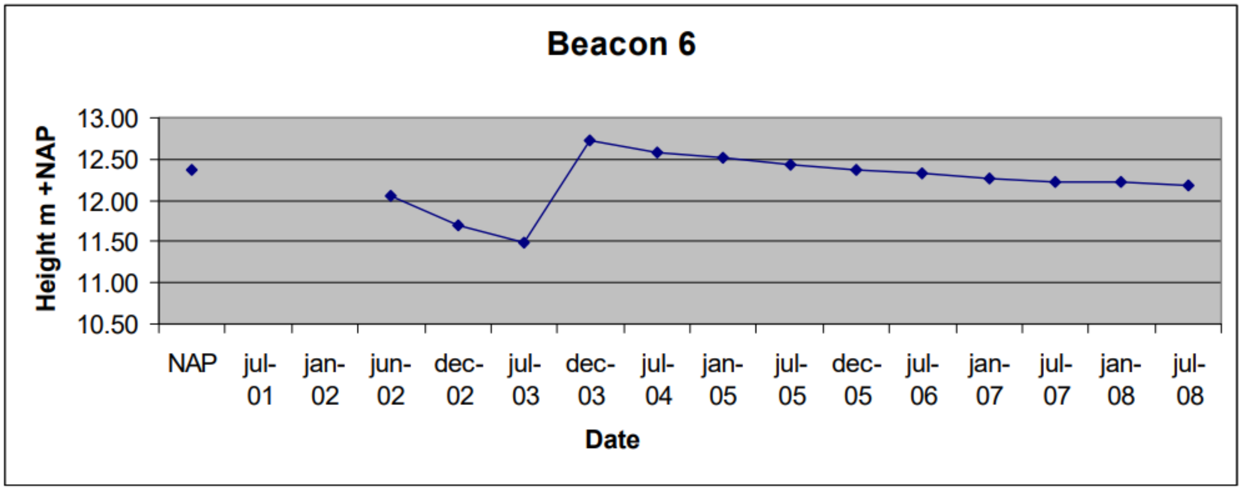

Figure 3.6: Settlement graph of plate 6 in cell 6 from July 2001 to July 2008 (van Meeteren et al., 2009a).

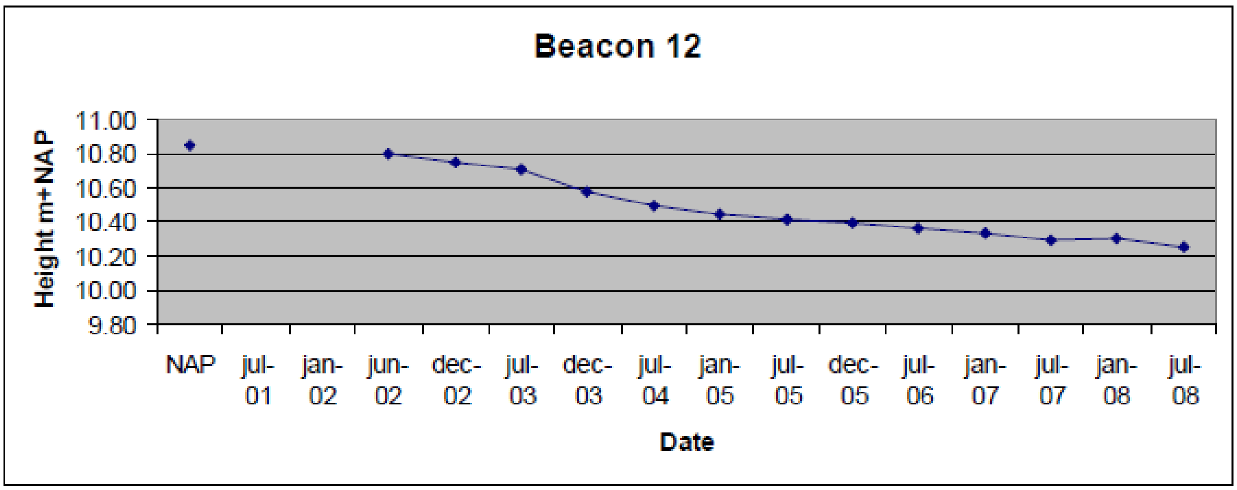

Figure 3.7: Settlement graph of plate 12 in cell 6 from July 2001 to July 2008 (van Meeteren et al., 2009a).

4 Methodology

This chapter will cover the methods used during this study. Section 4.1 covers the point cloud conversion and subsampling process (Subsection 4.1.1), and the registration (Subsection 4.1.2. Next, in Section 4.2 the cloth simulation filter is covered (Subsection 4.2.1), and the rasterisation of data step (Subsection 4.2.2). Then in Section 4.6 the method used in the settlement analysis is explained. Finally in Section 4.4 the processing and analysis of the gas well data is covered. In Subsection 4.4.1 the manner in which the extracted carbon is covered, then in Subsection 4.4.2 the interpolation and correlation of the data is covered.

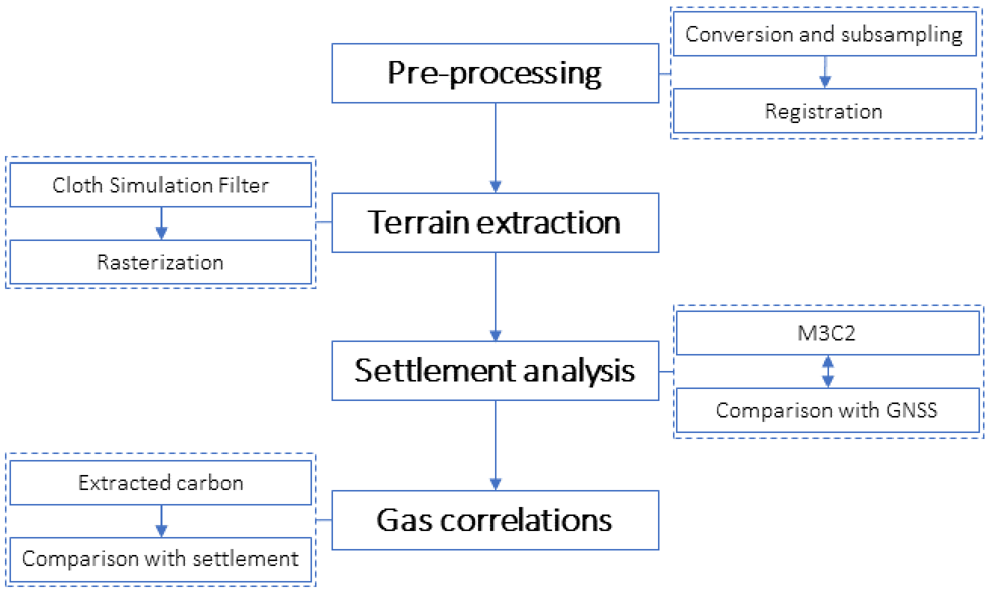

Figure 4.1: Flowchart of overall data work flow.

4.1 Pre-processing

4.1.1 Conversion and subsampling

The point cloud files are supplied in the .las or .laz file format. Unfortunately, these files are too large to be processed on a consumer desktop computer such as the one available during this thesis. Both the RIEGL UAV and TLS data are converted to the .e57 file format, a vendor-neutral ASCII format for storing point clouds and metadata produced by 3D imaging systems. It uses a subset of XML, extended to efficiently support storage of large amounts of data (Huber, 2011). Simultaneous with the format conversion the point clouds are also subsampled to 50 mm, greatly reducing the processing power required to run the files.

4.1.2 Registration

The point clouds produced by both the UAV and terrestrial laser scanner are manually aligned to allow for comparison. The registration (or alignment) of point cloud data is a key stage in the overall workflow of working with point clouds, and can have significant effects on the overall quality of results derived from the point clouds. Prior to registration the clouds are at vastly different coordinates, as shown in Figure 4.2, rendering them unusable for comparison or analysis.

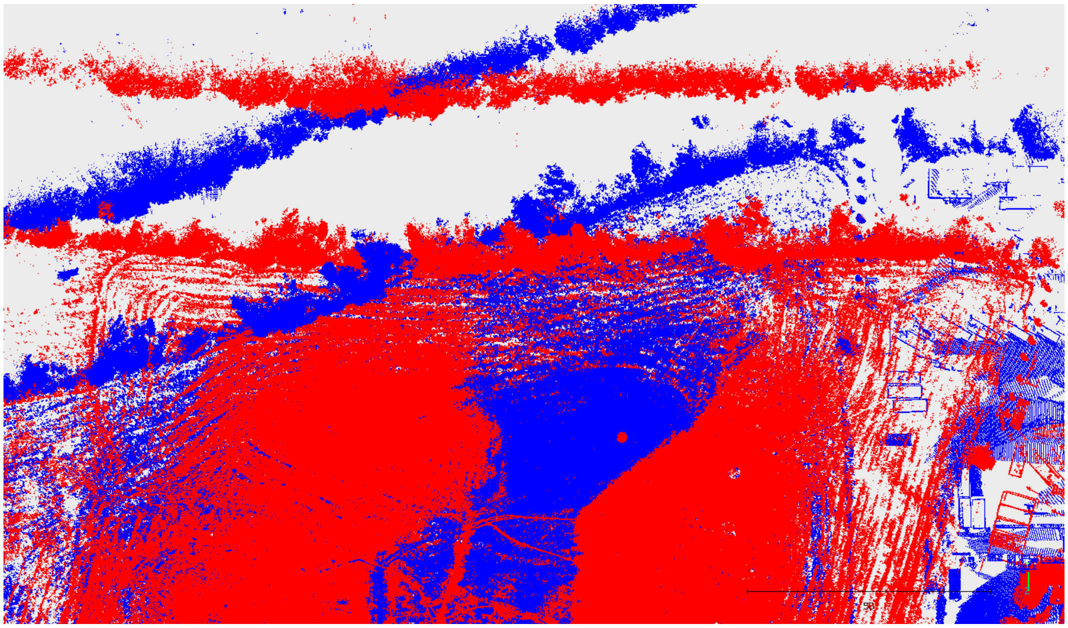

Figure 4.2: Example of unregistered Wieringermeer TLS data, note the mismatched tree lines in the upper half of the figure. The red point cloud is TLS data from August, and the blue is TLS data from July.

The registration of the TLS and ALS data is an iterative process, where each iteration should further reduce the distance between the point clouds. An initial coarse alignment is done after which an algorithm is applied to further refine the results.

The first rough registration is done using the *'Align (point pairs picking)'* tool built into CloudCompare. The user manually pick several pairs of equivalent points in each cloud as to register them. Whilst it is a manual process, the points are picked by eye, it is fast and can be quite accurate depending on the geometry available to the user (CloudCompare, 2016).

Next the ICP algorithm is run on the manual point pair registered point clouds. The ICP algorithm works in three phases: first it establishes correspondence between features that are to be aligned based on proximity, then a rigid transformation that best maps the first procedure is estimated and applied (Prokop and Panholzer, 2009). Once the iterative registration process is completed a quality check should be done on the alignment.

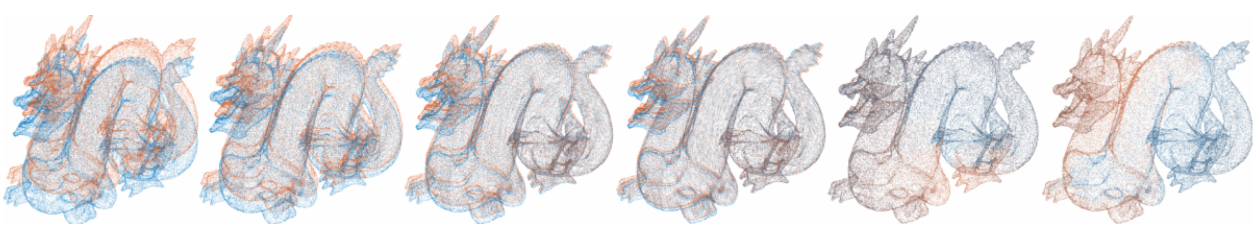

Figure 4.3: Example of ICP implementation, where the source and target point clouds are iteratively converging (Glira et al., 2015).

As the measurement campaigns are spread out over more than a year, the landfill will see both settlement and differences in vegetation at each measurement. This renders the landfill area unusable for registration purposes. Instead fixed objects, ones that should see no movements between the measurement dates, are extracted from the rest of the data and compared to determine the level of closeness of the alignment. This can be done using tools built into software such as cloud-to-cloud distances, or more manually by comparing the cross section of these objects.

4.2 Terrain extraction

Comparing the point clouds after registration can provide information on the movement of the landfill surface without issue, assuming the registration was performed using rigid stationary structures or objects. However, one must realise that by doing this prior to further processing, any (height) differences observed are not necessarily caused by settlement. Factors such as vegetation growth, or the movement of structures on the landfill will all influence the settlement data. To get to the real settlement of the landfill surface, the data needs to be processed in such a way that any external influences are removed.

In the case of the landfill this filtering can be described as separating the laser points on the terrain surface (ground-points) from the irrelevant points (non-ground-points). In essence a conversion has to be made from a Digital Surface Model (DSM), which captures both the natural and built/artificial features of the environment, to a vegetation-less Digital Terrain Model (DTM) which filters out non-ground points (both natural and artificial). This should be done very carefully as it can greatly influence the results.

There are a variety methods available to filter vegetation and non-ground-points out of the point clouds. Many of these methods use several iterations of interpolation, where points above the interpolated surface are classified as non-ground or vegetation, and then interpolated again with a new selection of potential ground points (Anders et al., 2019). Variations of this method are Triangulated Irregular Networks (TIN) densification implemented into LAStools, or the Iterative Surface Lowering (ISL) algorithm based on a raster with regularly spaced grid cells. A different approach is Cloth Simulation Filtering (CSF), which the next section will delve deeper into. Due to the ability to finely control the CSF algorithm through CloudCompare, as well as showing promising preliminary results, this method was chosen.

4.2.1 Cloth Simulation Filter

The Cloth Simulation Filter (CSF) is a method to separate point clouds into ground and non-ground points using a simple concept. When a rigid cloth is placed over an object it won't perfectly contour and drape every nook and cranny. This rigid cloth is draped over an inverted point cloud, covering the inverted surface as shown in Figure 4.4. By then analysing the interactions between the cloth nodes, and the corresponding points in the cloud, an approximation of the ground surface can be made. Then by comparing the original LiDAR points to the newly generated surface a distinction can be made between ground points and off ground points. This algorithm was proposed by Zhang et al. (2016) and subsequently implemented in CloudCompare and other point cloud processing software.

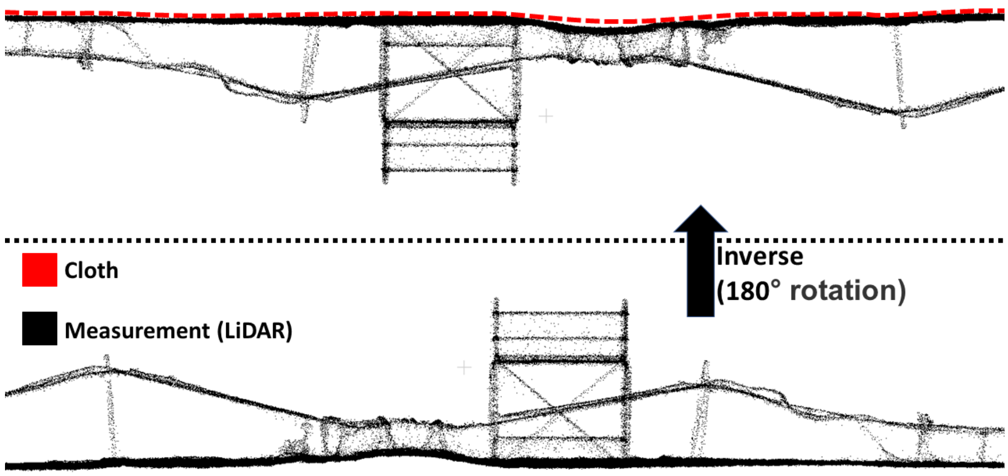

Figure 4.4: Schematisation of the cloth simulation algorithm in use on the landfill.

The characteristics of the cloth can be altered, allowing for control of the cloth simulation and the resulting ground point distinction. The grid size of the cloth nodes can be increased to save processing power, at the cost of a coarser DTM. To save additional processing power the number of iterations can be decreased. Finally by changing the classification threshold the sensitivity of the algorithm can be changed. Figure 4.5 shows the result of the CSF algorithm on the landfill, where the off-ground points such as the pipes and nearby people are separated from the landfill, note that in this figure the point size of the off-ground points was increased by a factor of 3 for easier visibility. One can also observe in the bottom left corner, marked by a blue box, that parts of the tri-pod and aeration infrastructure are incorrectly marked as ground points.

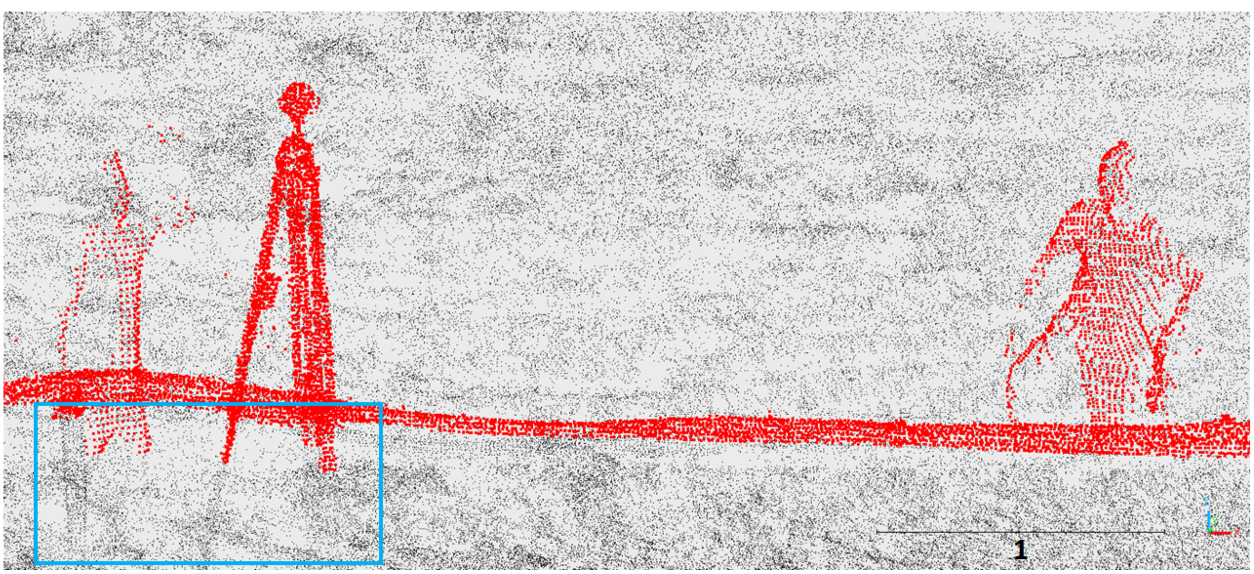

Figure 4.5: Example of the Cloth Simulation Filter (CSF) algorithm applied to a TLS point cloud of the landfill (off-ground points in red, ground points in black). Blue rectangle highlighting incorrectly marked ground points.

4.2.2 Rasterize

To further filter out vegetation an additional step is taken whilst processing the LiDAR data. The point clouds are rasterized, which subdivides the point cloud into a square grid. The size of the cells is user defined depending on the use case. Within these grids the minimum height of all points within the cell is computed, after which the grid is updated with this minimum value as height. The underlying assumption is that for a patch of vegetation, the points higher in elevation were caused by leaves or blades of grass. The lowest points were able to penetrate the vegetation either partially or fully. Thus by filtering out the high points one is left with a higher percentage of ground points versus off-ground points. The percentage of points to filter out depends on the point density and their distribution, which can be controlled by the grid size.

4.3 Settlement Analysis

Once the point clouds are in a processed state the differences between them can be found, which is done using the point cloud comparison method M3C2 (Multiscale Model to Model Cloud Comparison) built into CloudCompare. The underlying assumption is that differences between point clouds scanned at different dates are caused by settlement of the landfill. This method was developed by Lague et al. (2013) and works by first performing a surface normal estimation and orientation at a scale consistent with the local surface roughness. It then measures the mean surface change along the normal direction with explicit calculation of a local confidence interval. The method demonstrates a higher accuracy, as well as an easier workflow due to the absence of surface meshing or digital elevation model generation, than existing surface change detection methods (Lague et al., 2013).

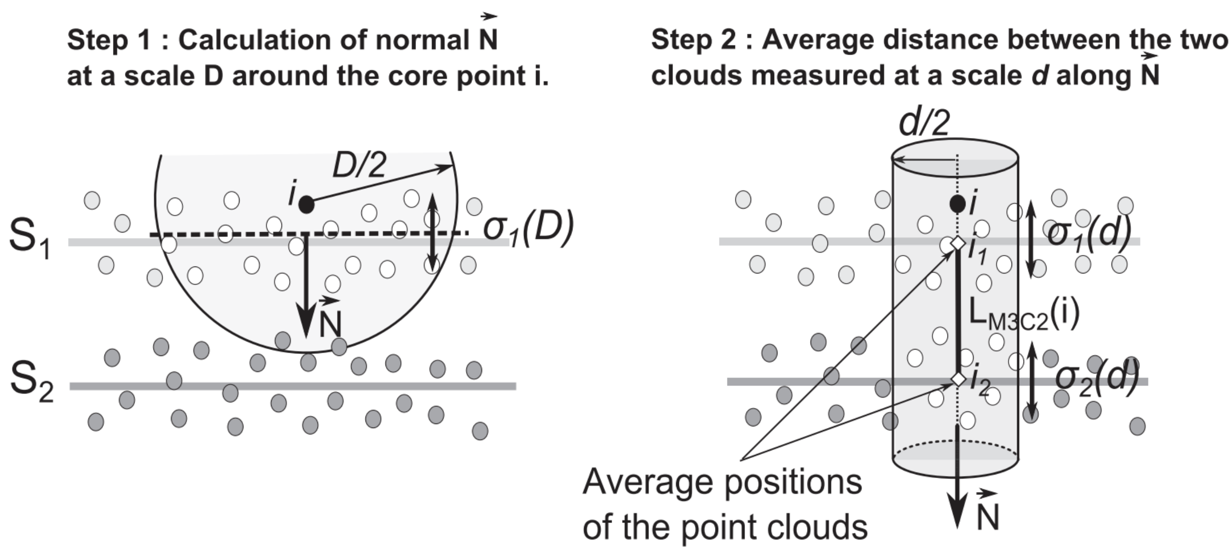

Figure 4.6: Principle of the M3C2 method (Lague et al., 2013).

For a core point i, as shown in Figure 4.6, a normal vector is defined for both of the clouds by fitting a plane to the neighbours of that cloud within a radius $D/2$. This radius is set as input within the tool and should be set according to the local roughness of the cloud, which is an estimate based on the standard deviations of the clouds (σ_1 and σ_2). Then the standard deviation of the distance of the neighbours to the best fit plane is used as a measure of the cloud roughness σ_i. Then a cylinder of radius $d/2$ is centered through i

and oriented along the normal vector. The intercept of each of the clouds within the cylinder defines two subsets, which are projected on the axis of the cylinder to find two distributions of distances.

The mean of the distribution, S_1 and S_2, and the standard deviations, σ_1 and σ_2, provide a local estimate of the point cloud roughness along the normal direction (Lague et al., 2013). The local distance $d_{1,2}$ between the clouds is then given by the distance $d_{1,2}$ between i_1 and i_2. The local distance measurement error is estimated using prescribed confidence level (like 95%) from sources of uncertainties.

4.4 Gas measurements

The monthly field measurements are divided into a file per year, from these the data is extracted that is relevant to the available GNSS and LiDAR measurements and placed into a single excel file. As the data is placed into a standardised template it can be easily loaded and processed by external processing software such as Python or MATLAB.

The field measurement data only contains the well number at which the measurement took place, but no further spatial information is provided. At an earlier stage the coordinates (RD-coördinaten) of the wells were recorded using a GNSS device, these are also loaded into the Python environment and linked to the well numbers. The gas wells are assumed to stay fixed in the horizontal (XY) dimension, forming a constant grid of data points against which to compare the settlement of the landfill.

From here several measured parameters can be directly compared to the point cloud data, such as the temperature at each well, the pressure and the gas composition. For other parameters further steps are required. One such parameter is the carbon mass extracted by the wells.

4.4.1 Extracted carbon

To obtain the amount of extracted carbon from the wells some additional calculation is required. To find the flow rate at each individual well the flow from the gas extraction blower, normalized at standard temperature and pressure (Equation 4.1), were averaged over the period in which the manual measurements at each well were carried out. Note that an assumption is made that all flow received by the blower comes from the wells, and there is no loss in the system.

$$Q_{\text{normalised}} = Q_{\text{inline}} * \left(\frac{p_{\text{atm}} + p_{\text{inline}}}{p_{\text{atm}}}\right) * \left(\frac{T_0}{T_{\text{inline}} + T_0}\right) \tag{4.1}$$

Here p_{atm} and p_{inline} are the atmospheric and inline measured pressures in hPa respectively, T_0 and T_{inline} are 0°and the inline measured temperatures in Kelvin, and Q represents the volumetric flow in m^3/s. This is then divided by the individual wells in proportion to the measured velocity, which differs at each well. Subsequently the molar flow rate of CH_4 and CO_2 present in the gas can be calculated using Equation 4.3:

$$CH_4\left(\frac{\text{mol}}{hr}\right) = (p_{\text{atm}} + p_{\text{well}}) * \left(Q_{\text{normalised}} * \left(\frac{C_{\text{CH}_4}}{100}\right)\right) * 100/\left(R * (T_{\text{well}} + T_0)\right) \tag{4.2}$$

and

$$CH_4\left(\frac{\text{mol}}{hr}\right) = (p_{\text{atm}} + p_{\text{well}}) * \left(Q_{\text{normalised}} * \left(\frac{C_{\text{CO}_2}}{100}\right)\right) * 100/\left(R * (T_{\text{well}} + T_0)\right) \tag{4.3}$$

where R represent the ideal gas constant $R = 8.3145 J \cdot mol^{-1} \cdot K^{-1}$. From here the amount of carbon extracted through the wells can be calculated using Equation 4.4:

$$\text{Carbon}\left(\frac{\text{kg}}{\text{hr}}\right) = \frac{\left(\text{CO}_2\left(\frac{\text{mol}}{\text{hr}}\right) + \text{CO}_2\left(\frac{\text{mol}}{\text{hr}}\right)\right)}{M_C} \tag{4.4}$$

where the previously calculated molar flow rates $\text{CO}_2(\frac{\text{mol}}{\text{hr}})$ and $\text{CH}_4(\frac{\text{mol}}{\text{hr}})$ are divided by the molar mass of carbon, M_C.

4.4.2 Comparison with settlement

To compare the parameters calculated in the previous section to the settlement of the landfill additional processing is required. First the gas well data is read from a Comma-Separated Value file (CSV) and each of the columns is populated to a newly created GeoPandas dataframe. A dataframe is a 2 dimensional data structure, similar to a table with rows and columns. GeoPandas allows for the preservation of the reference CRS by allocating the geometry to a special geometric *shapely* object. It also allows for the CRS to be changed, automatically adapting the coordinates to the new reference system. Next the remote sensing data is loaded into the same environment. The procedure for the TLS, ALS and GNSS data is the same as they all consist of coordinates with additional scalar fields such as height or M3C2 results. Figure 4.7 shows an ALS point cloud and the gas well coordinates loaded into Python, plotted using matplotlib.

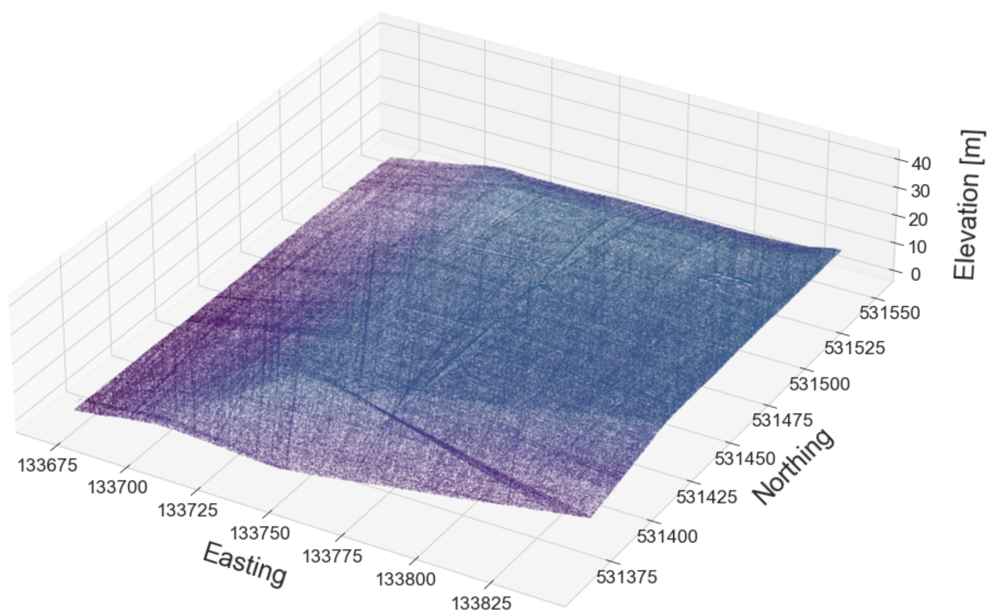

Figure 4.7: ALS point cloud loaded into Python. Coloring based on the intensity value but not of importance for the processing in Python.

Note that in Sections 3.2 and 3.3 the TLS and ALS data respectively were downsampled using the 'spatial' downsampling feature built into CloudCompare. This was sufficient for the processing performed within CloudCompare, but now that processing continues in Python the data had to be further downsampled to 100 mm. For further information as to what this entails please refer back to Chapter 3. Without further downsampling the processing steps required Terabytes of computer memory, as indicated by the Python console, something which was not available for this study.

The LiDAR data is cropped to the extent of the gas well infrastructure (Figures 4.8 and C.12), as to avoid extrapolating data outside of the bounds of the wells and to further ease the processing power required. Additional crops are made with buffer zones around the outer wells for when different outer boundaries are desired.

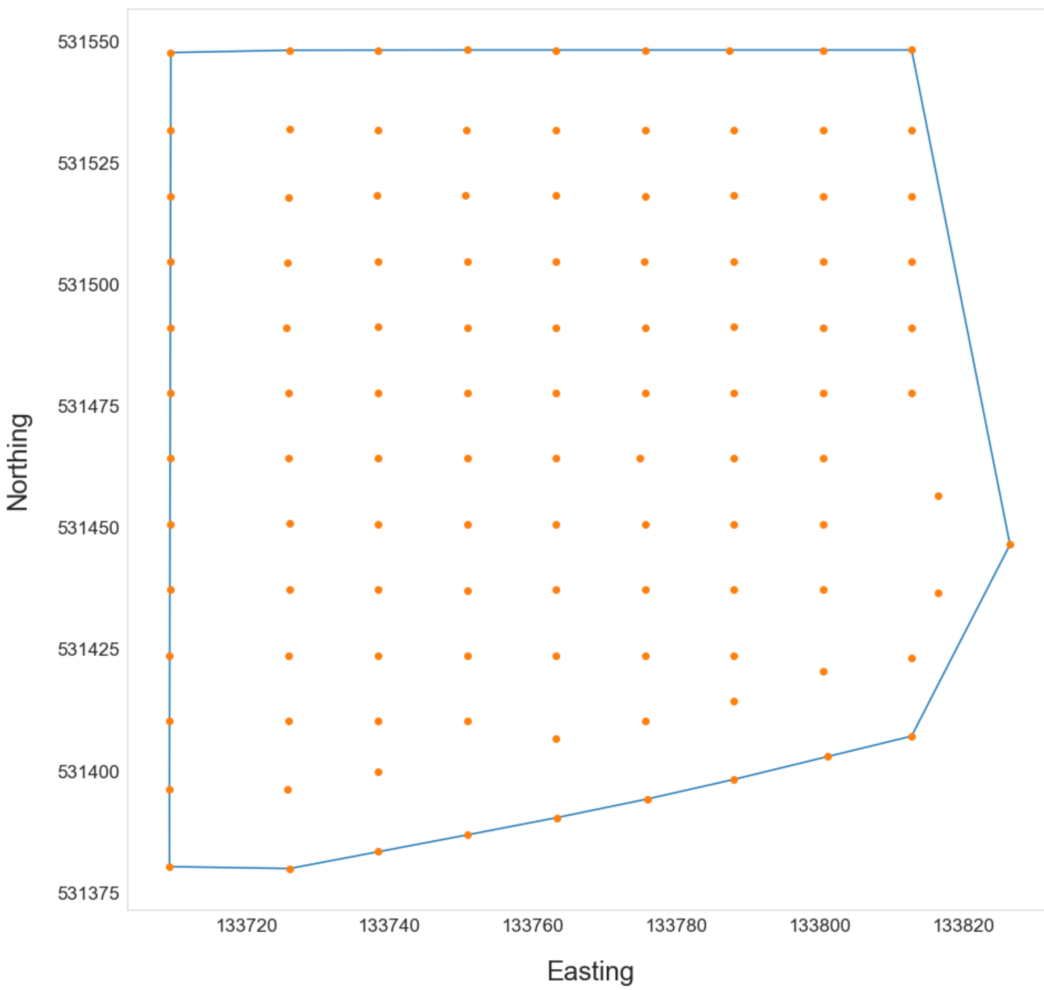

Figure 4.8: Area to which the LiDAR data is cropped, the dots represent the 110 gas wells.

The measurements by GNSS devices are at different coordinates than the gas wells, making direct comparison impossible, therefore to allow for comparison the gas and settlement data is interpolated onto the same grid of regular points, as shown in Figure 4.9. It was hypothesised that the density of ALS and TLS points would be sufficient for locating the gas wells within the original point clouds, negating the need for interpolation.

However, it was found that due to the effect of nearby difficult to manage vegetation, sensor noise, and the uncertain exact location of the gas well heads this was not feasible.

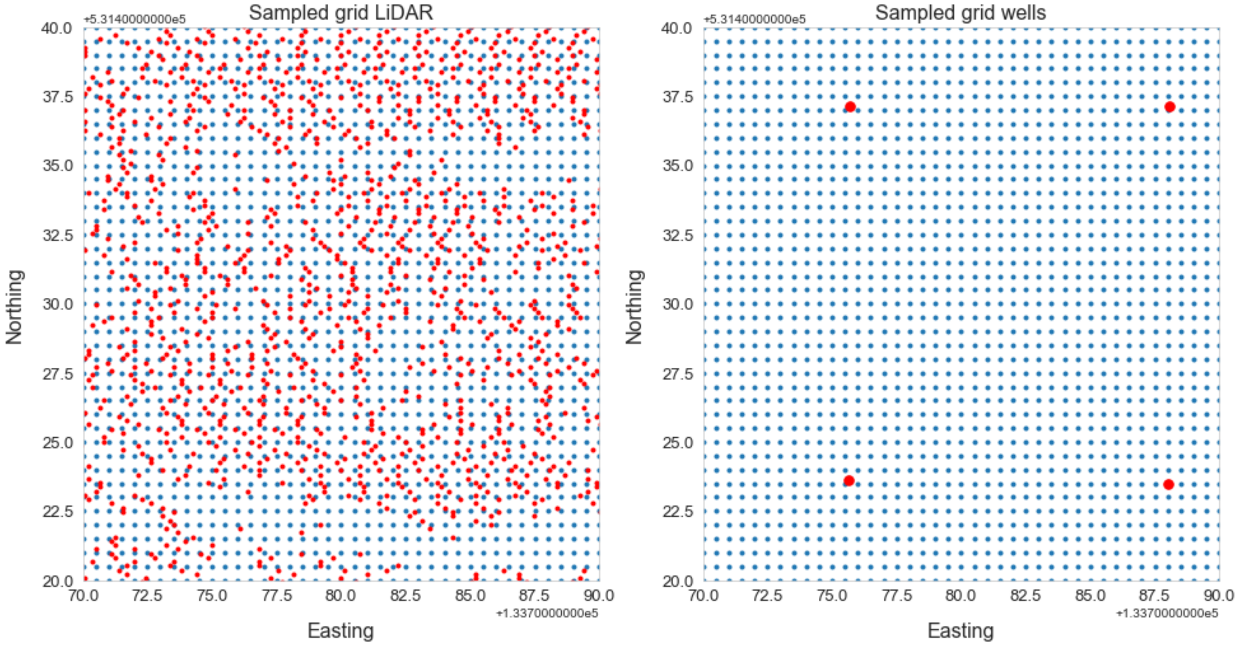

Figure 4.9: Interpolation grid with ALS LiDAR points on the left, and the gas well coordinates on the right (interpolation grid in blue, LiDAR points (left) and gas well (right) coordinates in red). The ALS points shown are 1/10th the actual amount of points for visual clarity.

Ordinary Kriging was chosen as method of interpolation. Kriging is a stochastic technique that uses a linear combination of weights at known points to estimate the value at an unknown point, the most commonly applied form of kriging uses a "semi-variogram" (Figure 4.10) which is a measure of spatial correlation between pairs of points describing the variance over a set distance (Hartkamp et al., 1999). Ordinary Kriging was chosen as interpolation method due to its inclusion of prediction uncertainty. The prediction variance depends on the spatial distribution of the points, and represents the uncertainty associated with the prediction.

The data being interpolated is split into training and test, the random split is controlled through a set seed so that the results are reproducable. Next the variogram is plotted, based on which the variogram parameters are manually fine tuned to find a best estimate for the sill, range and nugget. Sill is the value at which the model first flattens, range the ditance at which this occurs, and the nugget the value at which the variogram intercepts the y-axis.

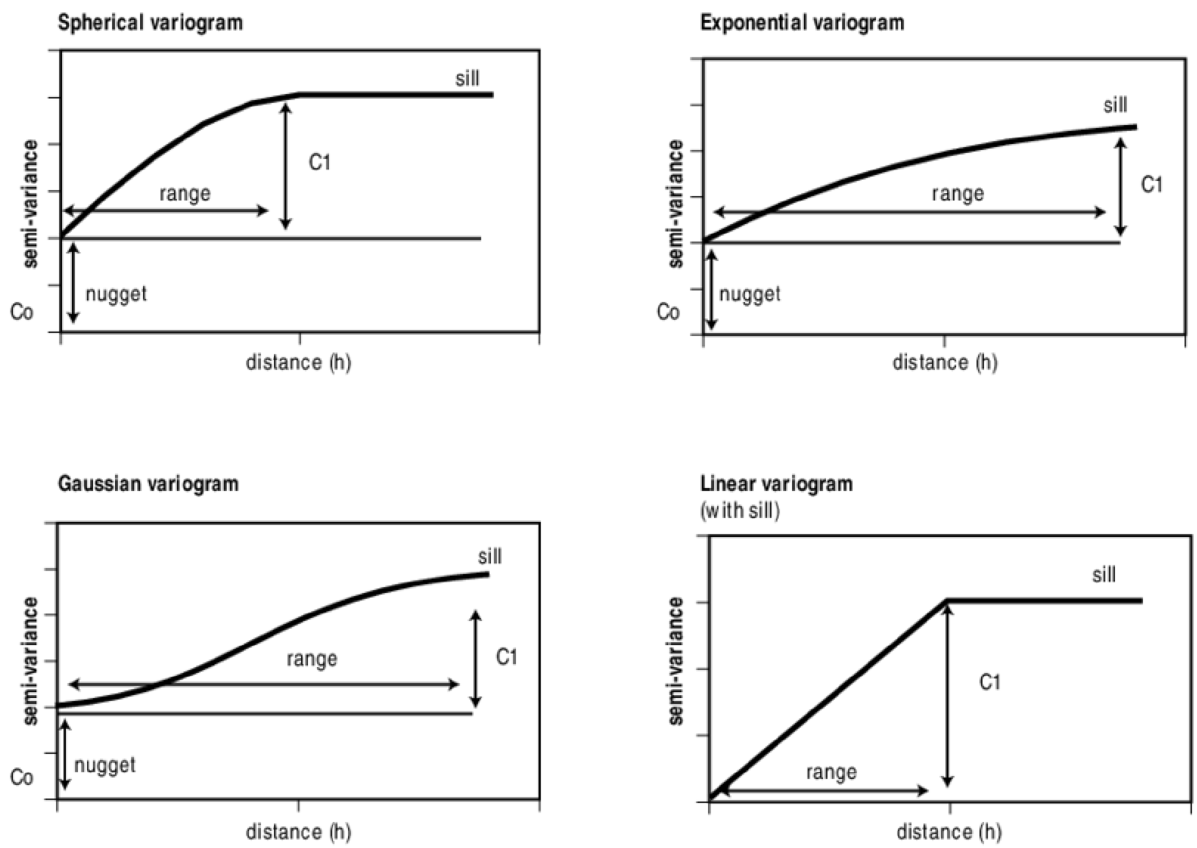

Figure 4.10: Examples of four commonly used variogram models (Hartkamp et al., 1999).

After the model is fitted, its performance is tested against the previously split testing data by plotting the prediction and observation against each other. Once the performance is deemed satisfactory by comparing the prediction values against the separated training data the model is applied to each grid point, creating a new prediction value which is added as a scalar to the DataFrame. Now that both the settlement and gas data is kriged to the same grid the correlation can be found. The Pearson correlation coefficient is calculated using Equation 4.5.

$$r = \frac{\sum (x - m_x)(y - m_y)}{\sqrt{\sum (x - m_x)^2 \sum (y - m_y)^2}} \tag{4.5}$$

where m_x is the mean of the vector x and m_y is the mean of the vector y. x and y are the input arrays, in the case of this study the settlement and gas well data. The Pearson relation measures the strength of the linear relationship between two variables (Williams et al., 2020). The coefficient ranges from -1 to 1, where -1 means a total negative linear correlation, 0 being no correlation, and +1 meaning a total positive correlation.

5 Results

This chapter will cover the results of this study. First, Section 5.1 the findings from the GNSS devices are presented. Second, Section 5.2 covers the registration of the point clouds. Third, in Section 5.3 a comparison of the remote sensing methods is given, followed by the settlement findings in Section 5.4. Finally, Section 5.5 covers the correlation between the settlement and waste degradation data.

5.1 GNSS measurements on settlement plates

From Afvalzorg nine sets of Stonex S10 GNSS measurements of the settlement plates were available, from 26-07-2017 till 08-09-2021. These are plotted in Figure 5.1, where the lines represent the cumulative settlement of a single settlement beacon and the thicker black line represents the mean settlement of the entire area covered by plates. Settlement plates installed on the slope of the landfill (Figure 5.1, shown in green) show significantly more settlement than those installed on the top of the landfill (Figure 5.1, shown in blue). A map of the ground plates can be found in Figure 3.3b.

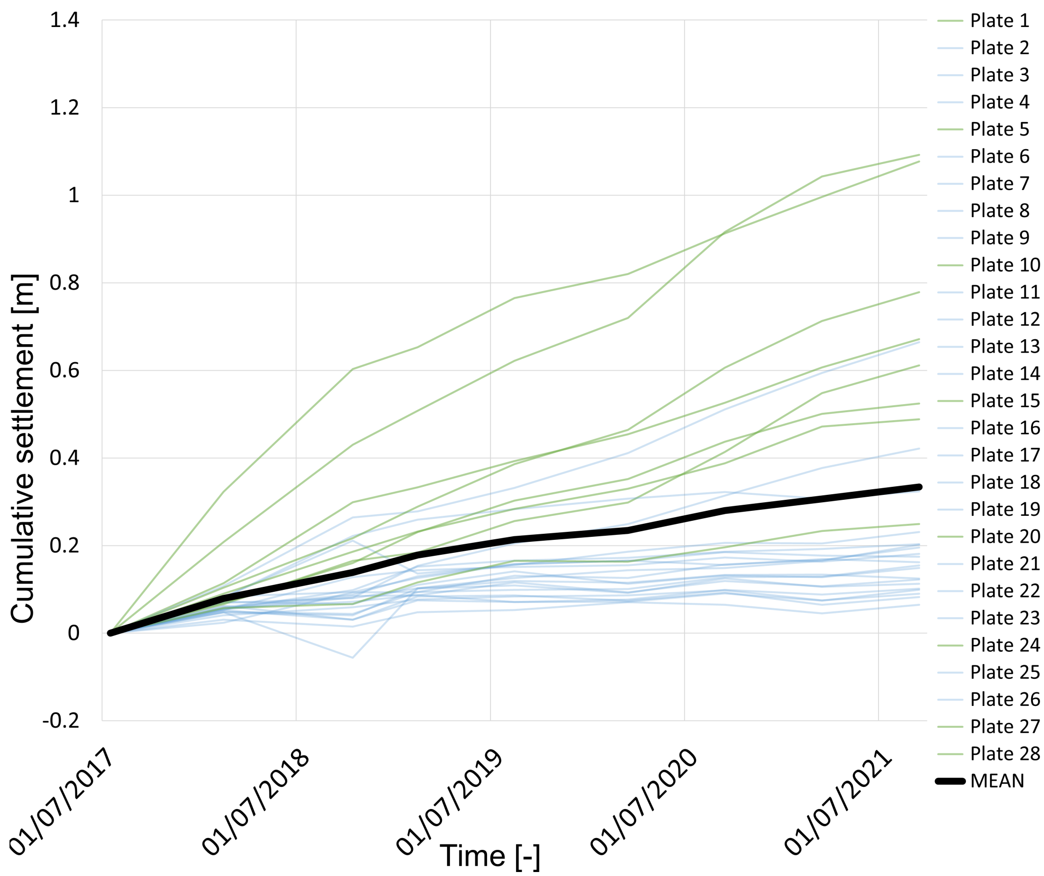

Figure 5.1: Cumulative settlement of the settlement plates from 26-07-2017 to 08-09-2021 (positive value indicating a decrease in height of the landfill).

Over the four years of measurements, beacon 15 placed on the slope experienced more than a meter of settlement (1.09 meter). Whereas beacon four placed on top of the landfill only settled 0.08 meter over this same time period. This is well beyond the Stonex's method uncertainty of 0.8 centimeter. A new set of measurements was made using the Trimble R8 on the 16th of March, shown as the most recent measurements in Figure 5.2. The campaign on the 16th shows a significant change from previous measurements. All but two of the settlement plates were measured having a reversal in settlement direction. The mean and median settlement of this set of measurements is -0.03 and -0.02 meter respectively, a negative value indicating the landfill is increasing in height (uplift). Whilst some earlier surveys showed sporadic cases of a beacon having negative settlement, none had an overall negative mean or median. The data is plotted as continuous lines to improve visibility of the observed anomaly.

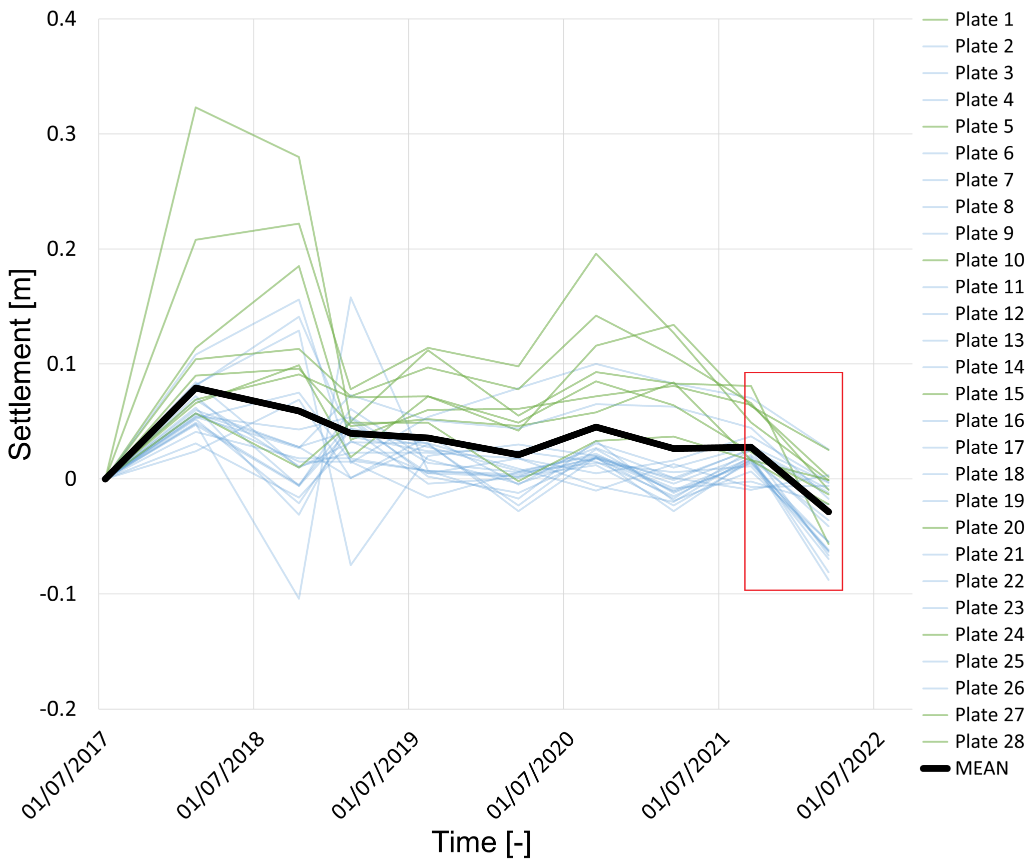

Figure 5.2: Measured settlement of the settlement plates using Stonex S10 GNSS data, latest measurement using Trimble R8. The red rectangle indicates the transition from the most recent Stonex S10 measurement to the Trimble R8 measurement.

To further investigate this discrepancy observed between the measurements by the Trimble and Stonex rovers two additional measurements were made. The Stonex was used on the 17th of March, and the Trimble again on the 29th of March. These, as well as the earlier Trimble measurements are shown in Figure 5.3.

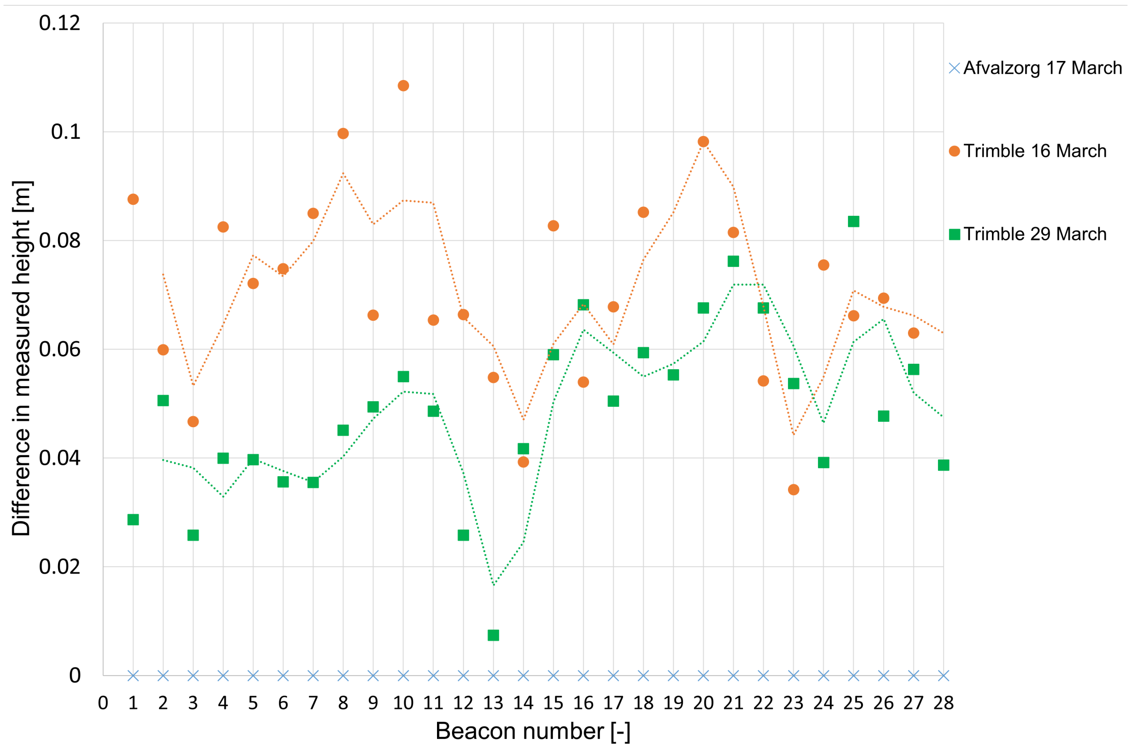

Figure 5.3: Differences between the Stonex (Afvalzorg, 17 March)) and Trimble (TU Delft, 16 and 29 March) GNSS measurements of the settlement plates, normalised for the Afvalzorg measurement.

The results in Figure 5.3 show that there is significant variance between the two Trimble measurements, as well as to the Stonex measurement. The characteristics of both devices were covered in Subsection 3.1. The stated precision is well below the differences found between the measurements, which was at certain plates more than 10 centimeters (plates 8 and 10). The differences are also much to large to be attributed to height changes in the landfill, as from Subsection 3.5 we expect there to be negligible settlement in the time span of two weeks.

The standard deviation and mean differences between the three sets of measurements are shown in Table 10. Median absolute deviations is included as it is less sensitive to outliers in the data. Due to the lower standard deviation between the Stonex measurements and the Trimble measurements on the 29th of March the error here appears systemic. On the other hand, the error between Stonex and the Trimble device on the 16th is highly variable.

Table 10: Differences observed between the Trimble R7 and Stonex S10 GNSS measurements of settlement plates.

(in mm)	Trimble 16 March - Stonex 17 March	Trimble 29 March - Stonex 17 March	Trimble 29 March- Trimble 16 March
mean	78.4	50.4	-28.8
st.dev	37.3	15.7	40.6
MAD (median absolute deviations)	72.1	51.5	-23.6
sMAD (st.dev)	20.0	14.3	25.9

To further isolate this issue a measurement campaign was organised on June 6th where both devices could be used simultaneously, providing measurements within 30 seconds of one another. This isolates the difference in satellite coverage between measurements, narrowing down potential causes of the discrepancy. In addition, a Trimble R7 GNSS Base was brought to the landfill, which was mounted to a tripod and placed on nearby paved ground to act as ground station. The data from the ground station can be used to post-process the Trimble R8 data and improve its precision, and/or validate the measurements.

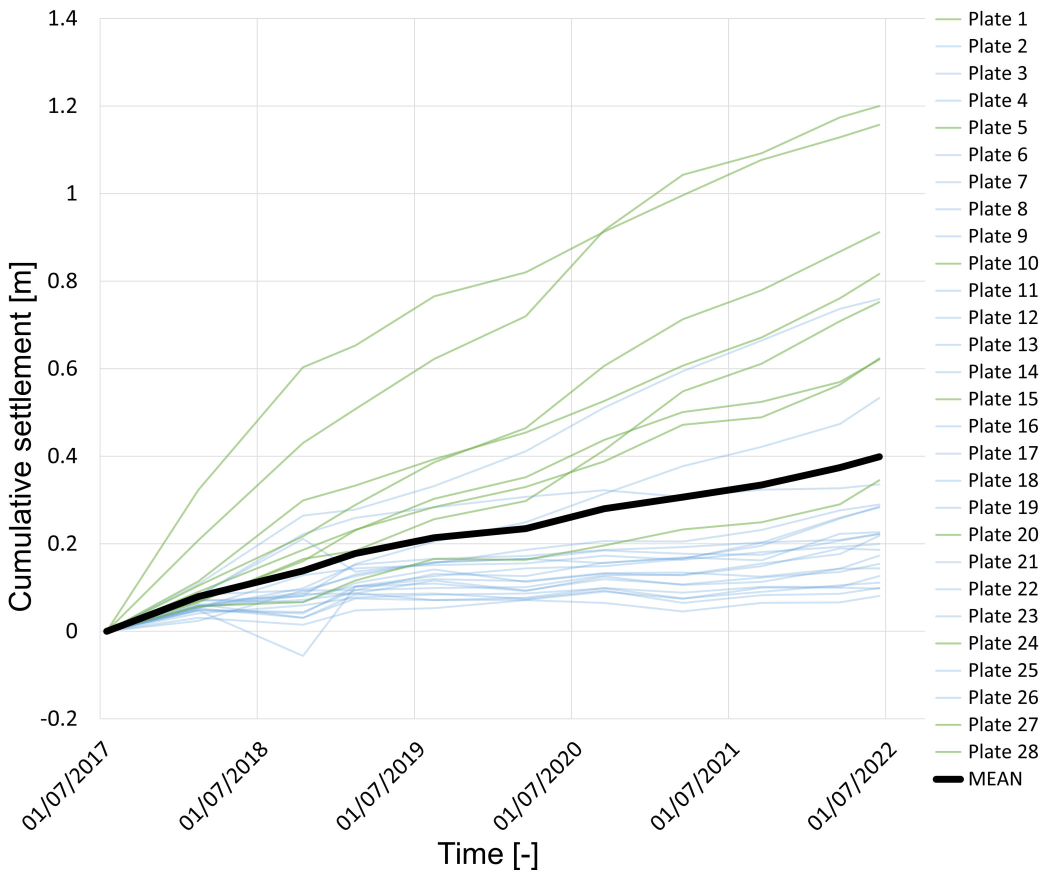

Figure 5.4: Cumulative settlement of the settlement plates surface using Stonex S10 GNSS data with added 17 March 2022 and 9 June 2022 surveys.

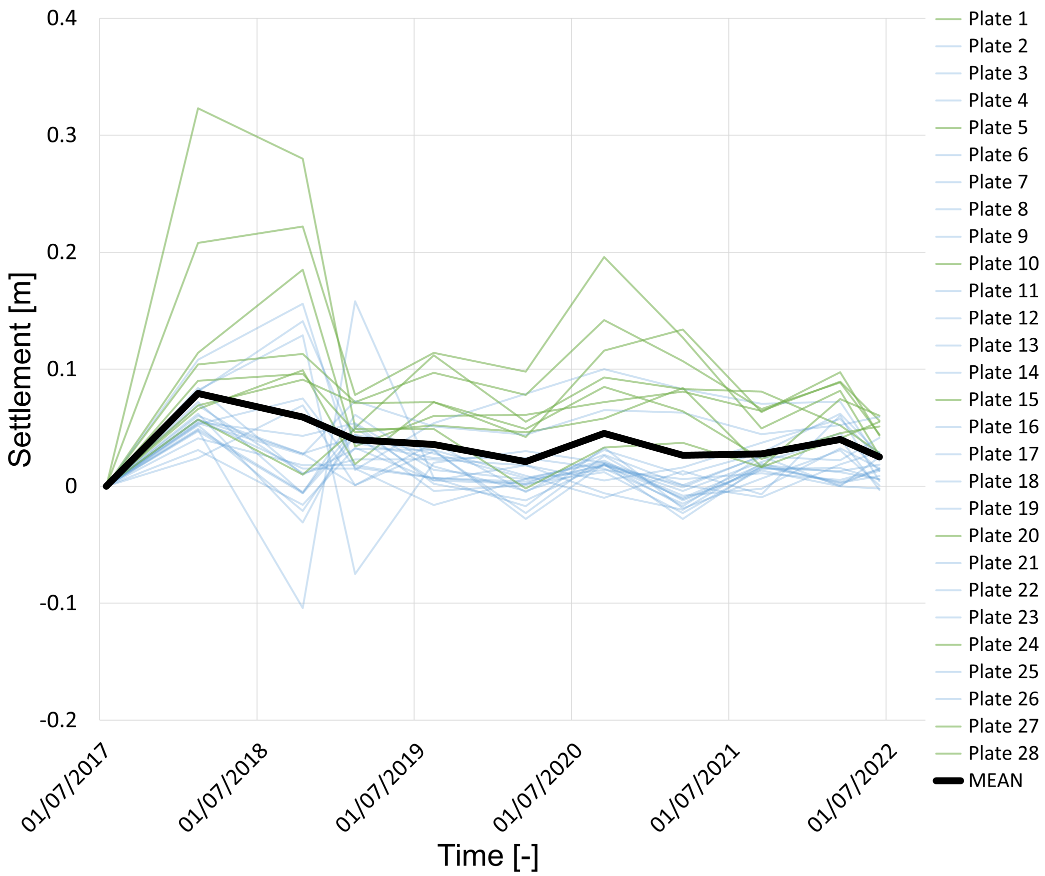

Figure 5.5: Settlement of the landfill using Stonex S10 GNSS data with added 17 March 2022 and 9 June 2022 surveys.

The Stonex S10 data is plotted again in Figure 5.4 and Figure 5.5, as done previously in Figure 5.1 and 5.2, including the additional measurements. The Stonex data shows no significant oddities and is inline with the previous trend in settlement. This adds additional confidence to these measurements prior to the comparison against the Trimble data.

When closely inspecting the Trimble R7 and R8 data from the additional survey on the 9th of June 2022 two potential causes of the measurement discrepancy were found. The first cause was an error in the NETPOS processing software. The software did not account for the offset in height caused by the antenna height center not being physically aligned with the measuring height of the receiver. This caused a constant error of 6.49 cm which has since been fixed (including in Table 11). The second cause is not an easily resolved fault or error, but instead poor overall performance of the Trimble rover when used without reference base station.

Table 11: Differences observed between the Trimble R8 and Stonex S10 GNSS measurements including Trimble R8 measurements post processed using Trimble R7 reference data. All data from 9 June 2022.

(in mm)	**Trimble R7 - Trimble R7 + R8**	**Stonex S10 - Trimble R7 + R8**	**Stonex S10 - Trimble R7**
mean	19.5	-4.7	24.2
st.dev	17.5	12.6	18.1
MAD (median absolute deviations)	9.5	23.5	11.2
sMAD (st.dev)	14.1	34.8	16.6

In Table 11 the results from post processing the Trimble rover data with the reference station are shown. Trimble R7 + R8 in the column header means that the Trimble R8 rover measurements were post-processed with the reference data of the R7 base station. From the results it is clear that the measurement discrepancy/difference between the Trimble and Stonex measurements decreases markedly when post processing is performed with Trimble R7 data. In Figure 5.6 the differences between the post processed Trimble R8 and Stonex S10 data are shown.

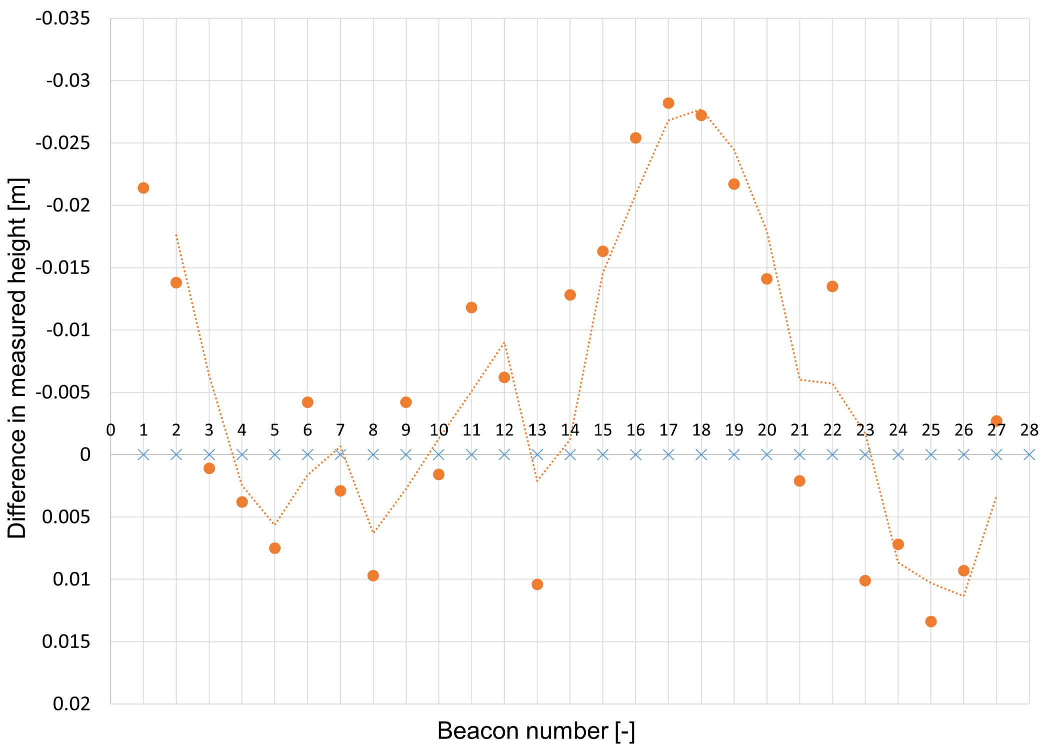

Figure 5.6: Differences between Trimble R7 + R8 and Stonex S10 on the 9th of June 2022. Normalised for Stonex S10 to show differences. Orange circles represent the Trimble measurements.

5.2 Registration

For the TLS and ALS scans in May 2021 and March 2022 which were performed on the same day, additional tie-points were selected on the aeration infrastructure pipelines and scaffolding. This extra step was taken as it was observed that the eastern part of the landfill, far away from the rigid structures on which tie points were selected, small offsets in the registration process would propagate and cause larger differences between the scans. This effect can be seen in Figure 5.7. Whilst movement is expected between the cross sections due to settlement occurring, this settlement will not cause the extreme tilt seen between the two cross sections which is especially noticeable on the right side. The TLS scans of July and August 2022 do not have an ALS scan available for the same day and as such these additional tie-points could not be used.

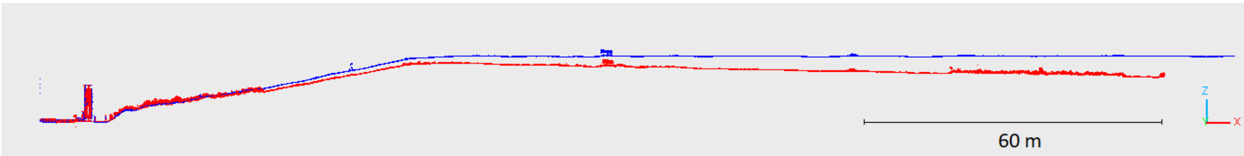

Figure 5.7: Cross section of landfill profile showing the gradual misalignment (misalignment increased in this figure for visual effect). Both profiles from ALS data (May 2021 in red, March 2022 in blue) prior to additional tie-points being placed on the aeration infrastructure.

The March 2022 ALS scan was chosen as the reference point cloud, based on which the other point clouds were registered. This scan was selected due to the relatively low amount of vegetation being present due to recent mowing. The TLS scan taken the same day was also considered. However, since the extent of the ALS scan is greater, especially in the southern and eastern direction, it was seen as the best reference scan available. Having these parts of the landfill better represented in the reference scan may be beneficial due to a propagating misalignment issue shown in Figure 5.7. In addition, on this day there were Trimble R8 GNSS measurements of rigid structures and the ground settlement plates, something not available to the 2021 ALS scan. The scans were first coarsely co-registered with manually selected tie-points, shown in Figure 5.8. Photographs of the structures used for registration are available in Appendix A.

(a) GNSS points near bio filters. **(b)** GNSS points near smokestacks.

Figure 5.8: Examples of manually selected tie points for point pair registration, ALS data from March 2022 in background. Scale in meters, scale bar is 4 m for Figure 5.8a and 4.5 m for Figure 5.8b.

This extra step where tie points are selected on the aeration infrastructure is not possible for the TLS scans of July and August 2021 as no matching ALS scan is available. Whilst the rigid structures, as the name implies, remain rigid and in place, the aeration infrastructure settles with the landfill. Therefore the aeration infrastructure can not be used as tie points for scans at different dates. For these scans GNSS measurements of the settlement plates are used as additional tie points but the use of these is limited. The plates are often slightly inset into the topsoil and covered by vegetation, rendering locating these plates in the scans a difficult or impossible task.

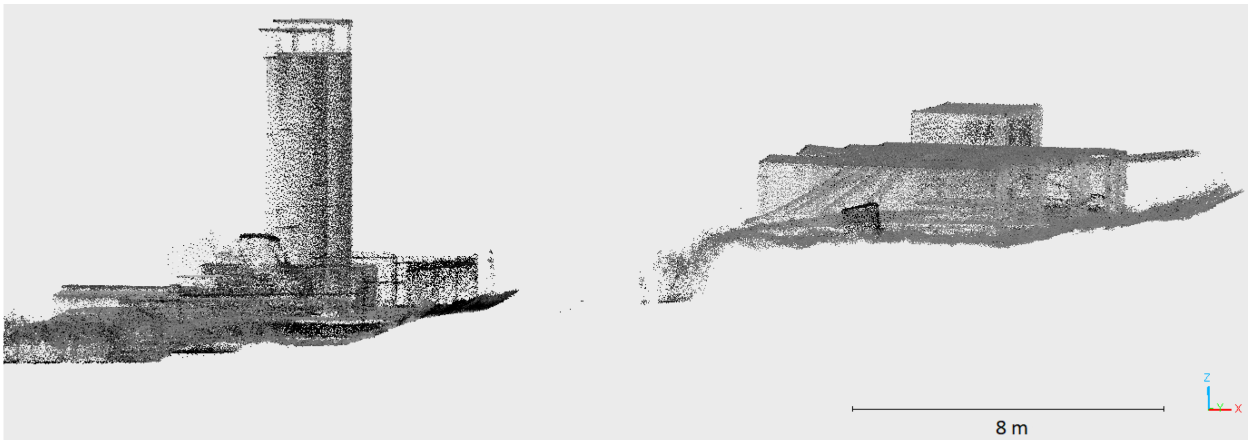

Figure 5.9: The approximate area cropped in all point clouds for use in the ICP algorithm due to rigid structures, smoke stacks and containers shown.

After the coarse registration using tie points an iterative process was performed incorporating the ICP algorithm, as explained in Subsection 4.1.2. This algorithm was only applied to a cropped area of the scans, devoid of as much vegetation as possible, as shown in Figure 5.9. When using vegetated surfaces the ICP algorithm has difficulties defining planar surfaces from the given vegetation geometries, and as such can not substantially reduce the registration errors which were circa 20 to 30 cm. This is much to large for the purposes of this study, with settlement being substantially lower than this range in areas of the landfill. Before the final registration error is determined an additional validation step is done.

The registration was further validated by visually comparing the cross section of the rigid structures to improve the alignment. One such example can be seen in Figure 5.10. Due to the shadowing effect the smoke stacks are only scanned on the side visible to the TLS scan locations, resulting in only a partial scan of the smoke stack as seen in Figure 5.10b.

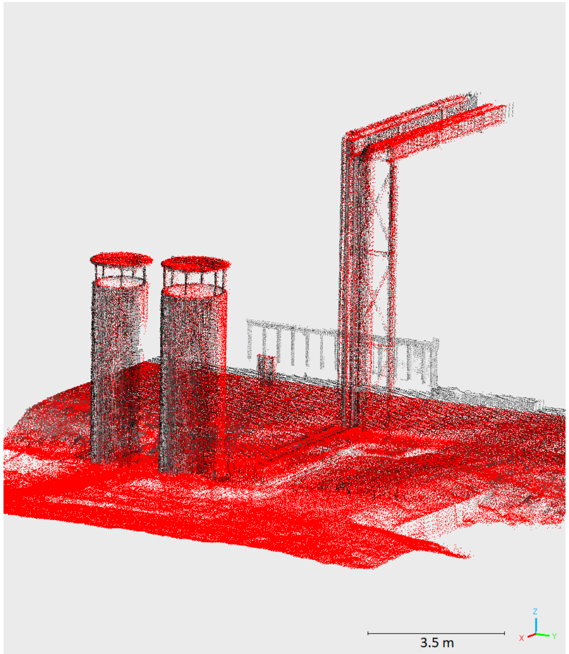

(a) Overall area

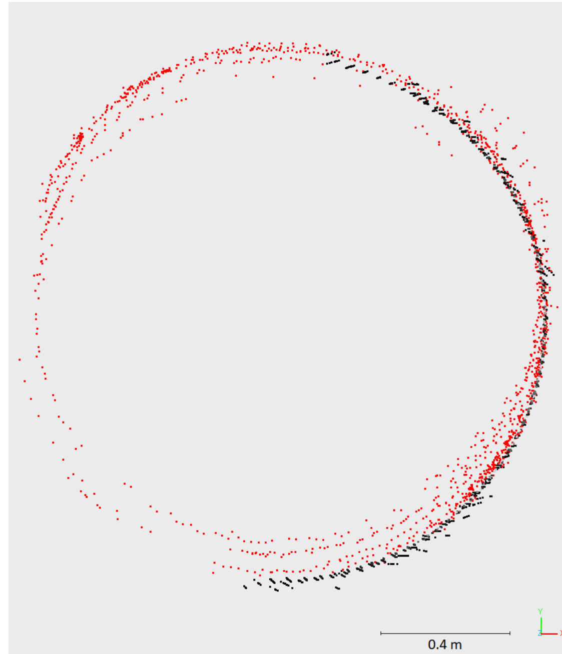

(b) Cross section of smokestack

Figure 5.10: Validation of registration using rigid structures (Red ALS March 2022, Gray TLS March 2022).

This iterative process was performed until no further gains were made, with a final registration error (Root Mean Square Error (RMSE)) of <3 cm for all scans. The registration of the two ALS scans resulted in a RMSE of ∼1.6 cm. The earliest TLS scan, in May 2021, suffers from a low number of scanning positions causing many of the objects used for registration to be only partially scanned. Due to this the lowest achievable RMSE was ∼3 cm. The three other TLS scans contain a higher amount of scanning locations, which were also more evenly spread. The TLS March 2022 scan was registered with a final RMSE of ∼1.9 cm. The July and August 2021 TLS scans had a final RMSE of ∼2.3 cm and ∼2.5 cm respectively.

The RMSE value is based on the smaller cropped areas with rigid structures and as such only provides an indication of the quality of the registration. Notably from the RMSE of the July and August 2021 TLS scans one would think the registration quality is high, but as mentioned further on in this report in Section 5.4 they are nearly unusable due to the bad registration quality on the top of the landfill.

Some exemplary crops of the quality of the registration achieved can be seen in Figure 5.11. Note that the areas shown in this figure were not directly used in the point picking process as that would introduce bias into the quality check. Locations with tie points will be 'forced' together in the registration process, making them unsuitable for validation of the overall quality.

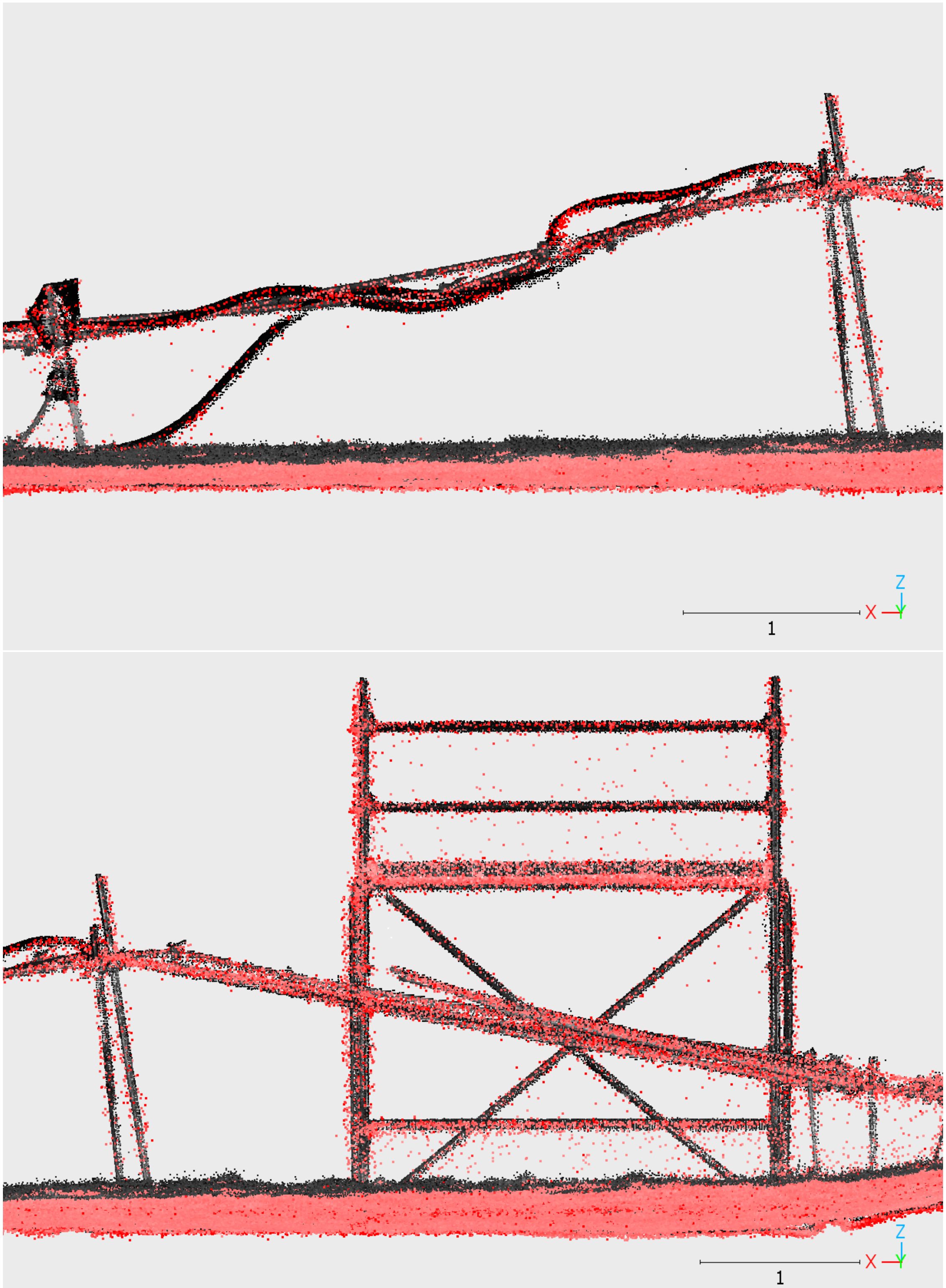

Figure 5.11: Crops highlighting the quality of registration. On view are the aeration structure and scaffolding present on the landfill. Gradient in point color due to use of intensity value color scale, scale in meters (Red ALS March 2022, Gray TLS March 2022). The ALS points are scaled up 50% to improve visibility. Quality achieved in these images is consistent with other areas of the point cloud. Scale in meters.

5.3 Comparison of acquisition methods

Once the scans are registered, the ALS and TLS scans are investigated for differences between the two methods. First, the ability of the methods to scan objects (structures, containers, aeration infrastructure, etc) is visually assessed. Unless otherwise specified the scans used in this comparison are the ALS and TLS scans of March 2022. Both methods experience the shadowing effect described in Paragraph 2.4.3.2. However, the TLS is affected to a much greater extent due to the relatively flat environment it is used in. The below figures of point cloud data are coloured according to their intensity value to help distinguish between objects. Unless otherwise specified the scale of the images is in meters.

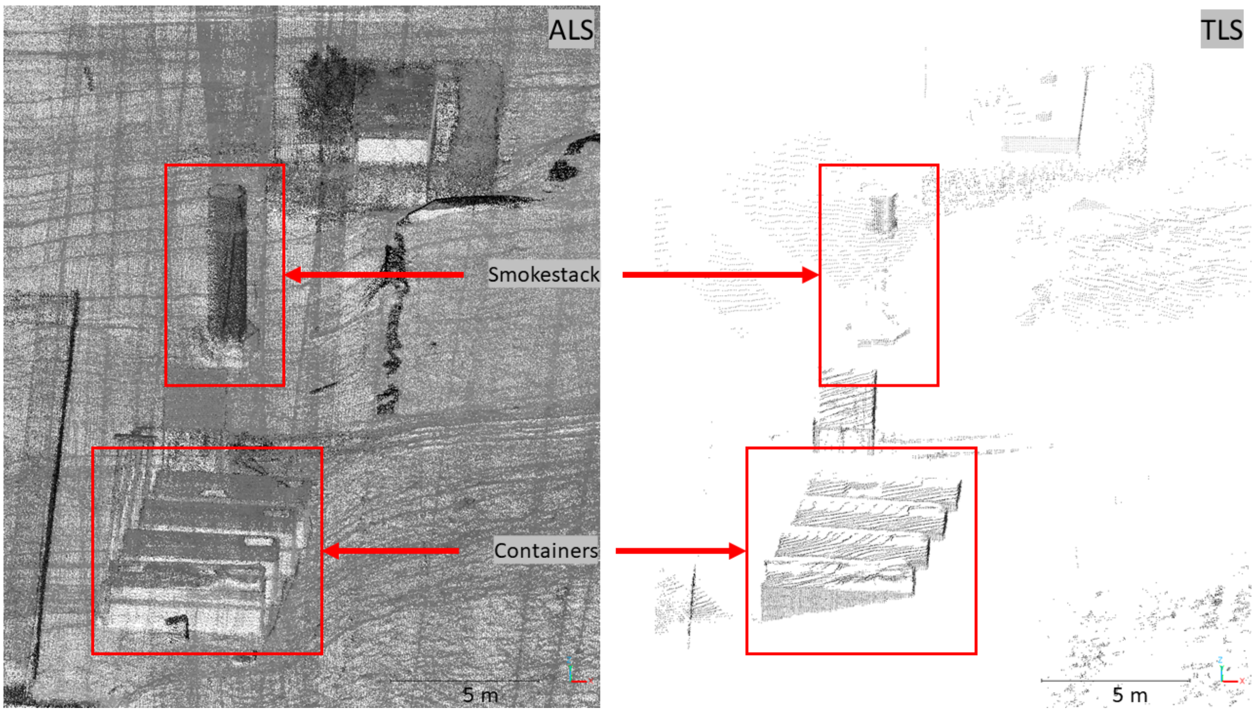

Figure 5.12: Cropped regions of March 2022 ALS and TLS scans to highlight differences, photographs of the rigid structures are located in Appendix **??**.

One can observe from Figure 5.12 that the TLS scan is only able to 'see' the top parts of the containers, as well as the smoke stack. This is due to the TLS scanning locations, which were all either on top of the landfill or on the western and southern slopes. The area shown is circa 50 meters away from the nearest TLS scanning location, and the drop-off in point density is significant. This drop-off is irrespective of using raw or downsampled data, although using downsampled data the effect is increased as already data-sparse areas are reduced in density further. The ALS scan maintains a consistent coverage of points throughout this area. The data is shown in its full extent in Figure 5.13, where these previously mentioned differences can again be clearly seen.

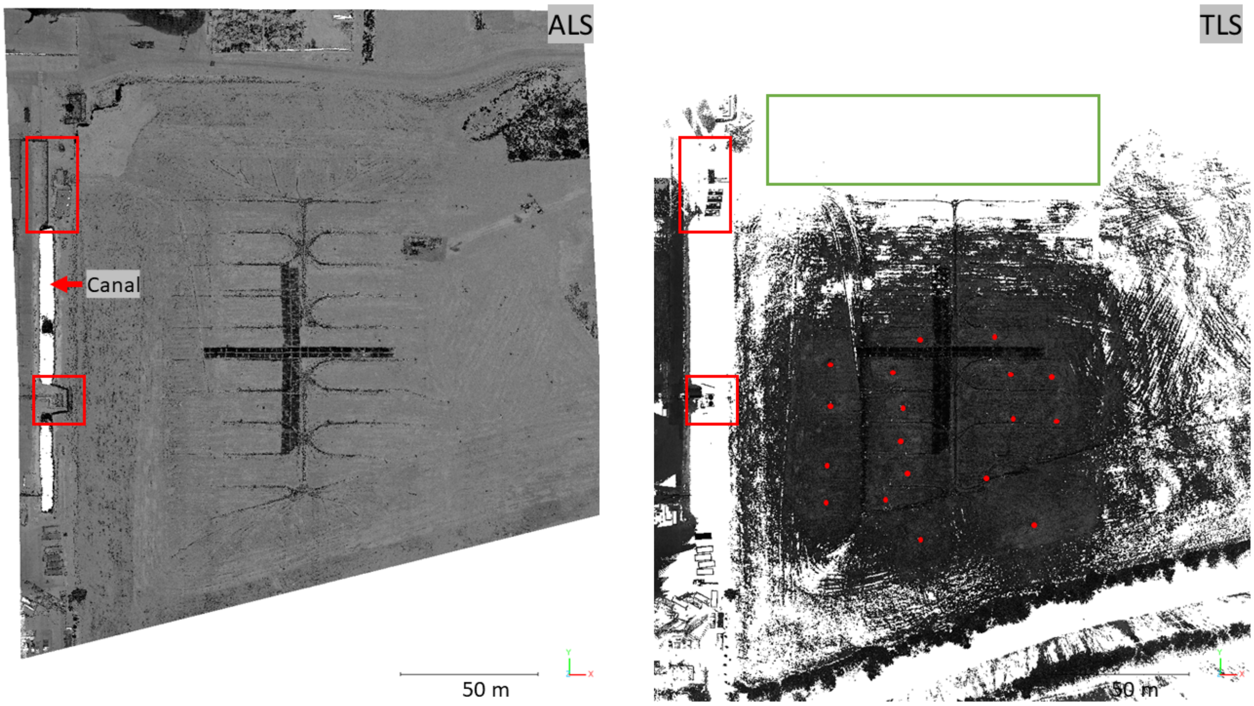

Figure 5.13: Overview of March 2022 ALS and TLS scans to highlight differences, the red points mark TLS scanning locations. The red boxes indicate the area shown in Figure 5.9 and 5.12. The green box marks the missing northern slope in the TLS data. The colouring of the point clouds is according to their intensity value, which differ between the two methods.

The area cropped for Figure 5.12 is in the far top left of these uncropped figures. In the eastern part of both the ALS and TLS scans a body of water is present, causing the area to be devoid of points as no return signals are received. The lasers wavelength causes most or all of the signal to be absorbed by the water. The ALS scan provides a visually continuous point cloud of the landfill, whereas the TLS scanning locations rapidly lose point coverage at radially increasing distance away from the scanner. The northern slope of the landfill is especially affected as it lies under the horizon for scanning locations on top of the landfill. The southern region in the ALS scan was cropped by the UAV operator and should not be compared to the treeline visible in the bottom of the TLS scan. Note that the large cross/plus shape seen in both scans is a geotextile that was installed to protect ERT electrodes that were installed on the landfill.

Using CloudCompare the point densities are mapped and shown in Figures 5.14. The densities represent the number of points within a circular 20 cm radius, 20 cm is chosen to speed up processing as larger radii often froze the software. For the purposes of this comparison the 20 cm radius also proved sufficient. In the TLS figure (on the right) the drop-off in points, as distance increases from the scanner is very clearly visible. Near to the scanner high densities are achieved in the region of tens of thousands of points. At a distance of 50 meters this has dropped to the low, or even sub, hundreds. The ALS data shown on the left shows a more even density, as compared to the TLS data, with no significant hot spots. For the ALS scan the density increases towards the center of the landfill, near the aeration infrastructure. This is due to the UAV's flight path being concentrated around this central area. The criss-cross pattern of stripes in the ALS figure (Figure 5.14) are caused by overlapping scan lines.

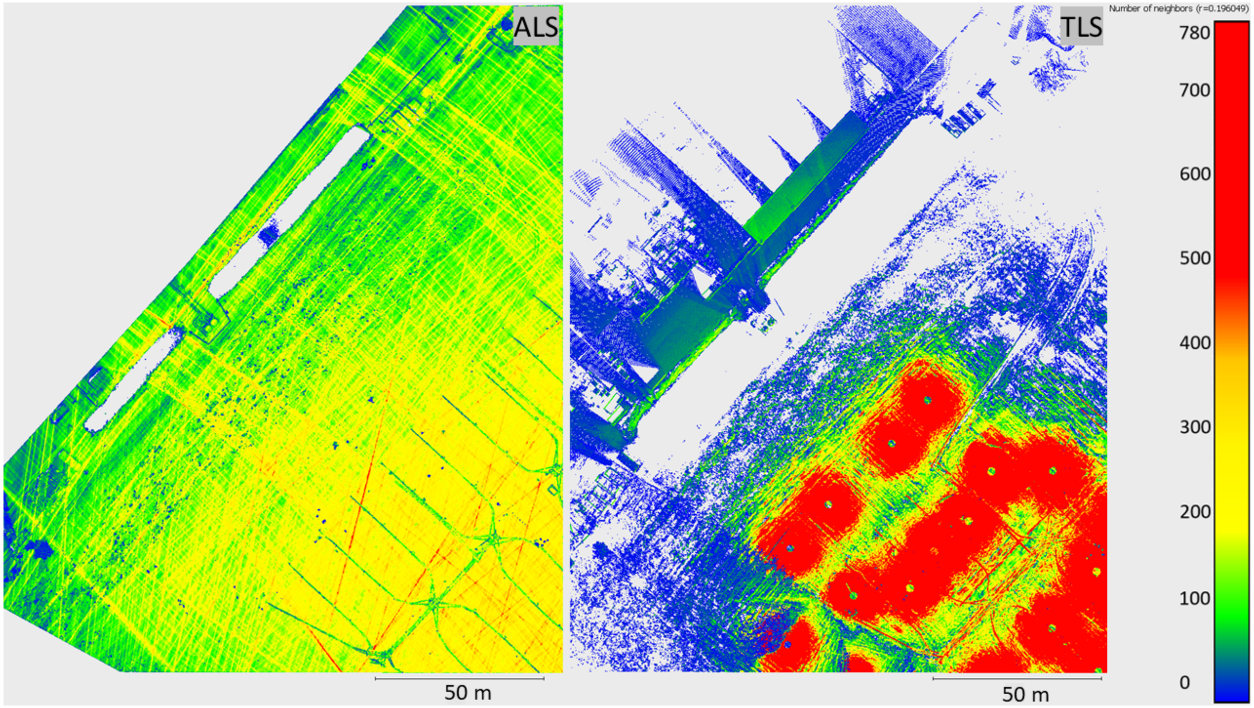

Figure 5.14: Point density of 2022 ALS and TLS point clouds (unsampled), numbers shown correspond to points within a 20 cm cylinder. The color bars are kept consistent for both the ALS and TLS data.

Histograms are created using the density values, shown in Figure 5.15. The histogram of the ALS resembles a Gaussian curve. This can be attributed to the UAV flying at even speed and height, and the constant scan rate of the scanner. As the UAV flies its grid-like flight path each area receives a relatively equal share of coverage, with the inner and outer areas receiving a higher and lower share respectively. The histogram for the TLS data is in a significantly different shape, heavily right (or positively) skewed with a long tail. The relatively heavily weighted tail is caused by areas of high density close to the acquisition location, where they overlap forming areas of mixed high and medium density.

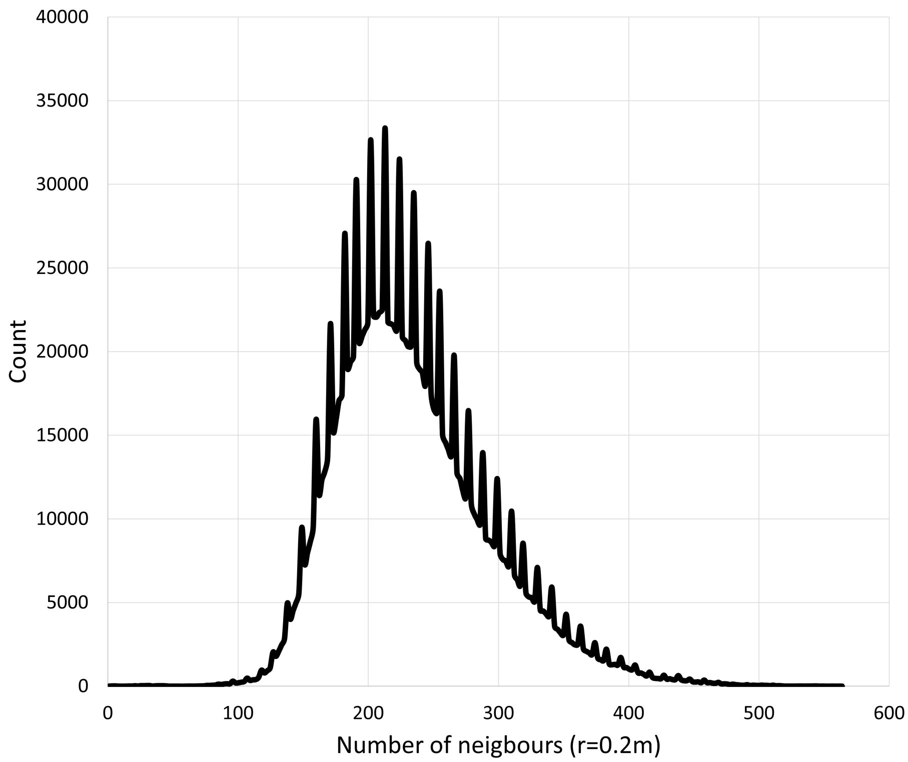

(a) ALS March 2022

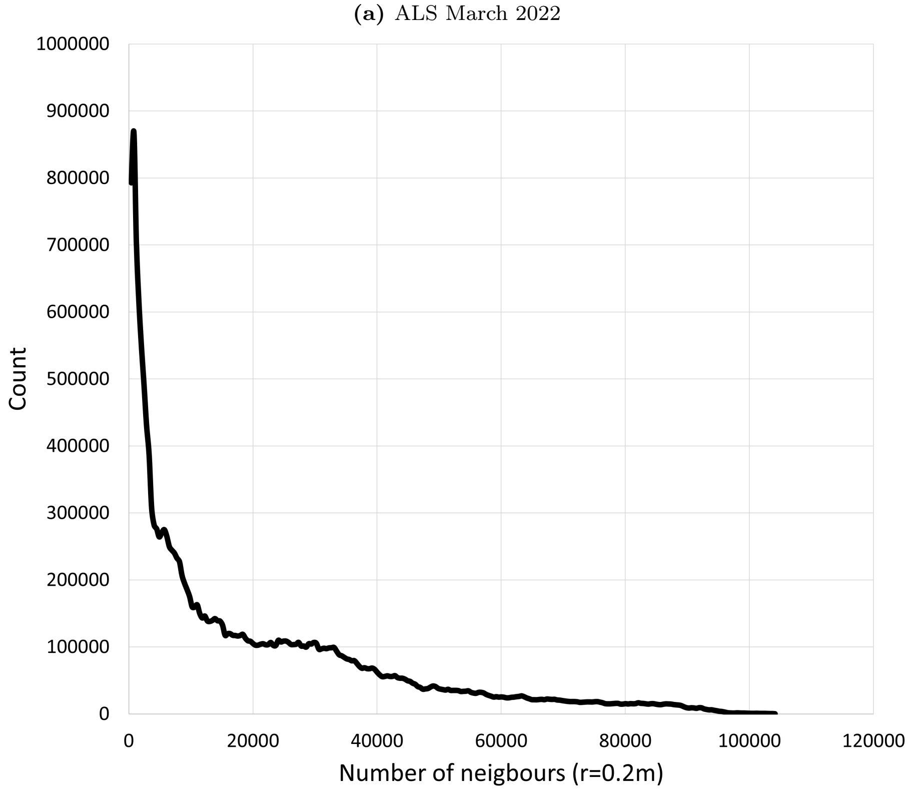

(b) TLS March 2022

Figure 5.15: Histograms of the density maps shown in Figure 5.14. The spikes in the ALS histogram (Figure 5.15a) are due to the earlier mentioned scan lines.

In Figure 5.16 two peculiarities are observed. First is an area of low point density underneath the aeration infrastructure pipelines in the ALS scan (blue diagonal line). The areas underneath the pipeline are occluded to the UAV flying directly above, rendering the only thing visible to the UAV the pipeline. Further decreasing the density is the circular shape and highly reflective surface of these pipes, which causes specular reflection decreasing the number of signals received by the scanner. Due to the low incidence angle of the TLS, instead of the aeration pipelines being areas of low density, they are areas of high density. The pipes are scanned just as for the ALS, except now the areas underneath the pipe are still partially or fully scanned. These additional points cause the areas of relatively higher density.

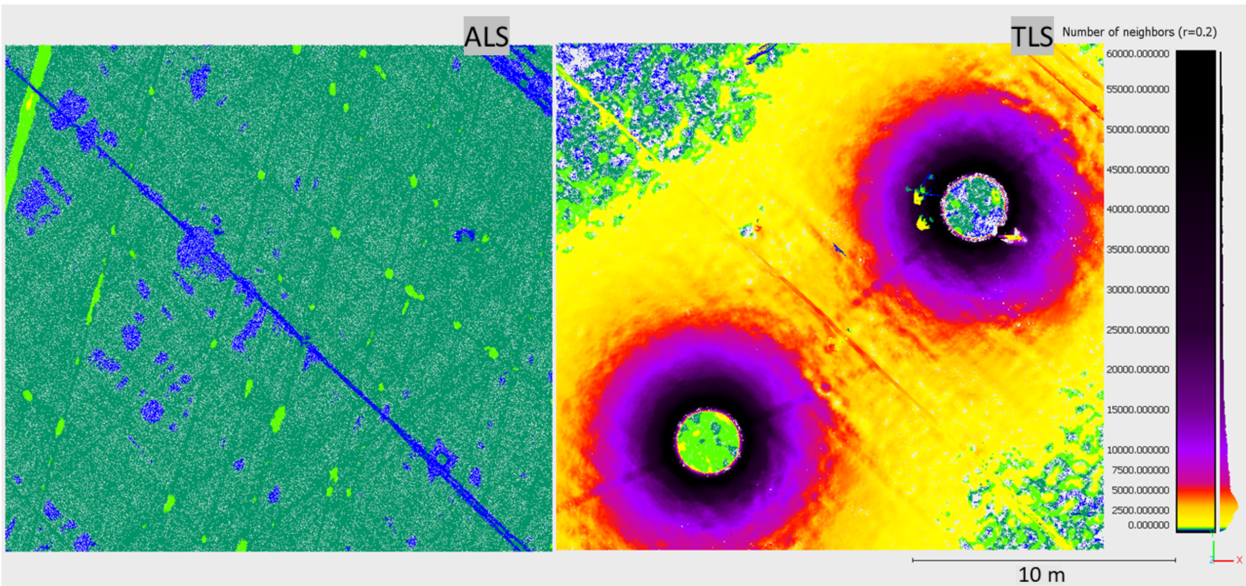

Figure 5.16: Cropped region of Figure 5.14 with adjusted color bar to capture full extent of density.

To further illustrate the drop off in point density away from the TLS scanning location some additional figures were made. Figure 5.17 shows the point cloud of a single TLS scanning location, 1 of 19, which combine to form the entire March 2022 point cloud. A small section, marked in red in Figure 5.17, extending radially outwards of the TLS location is extracted for further analysis.

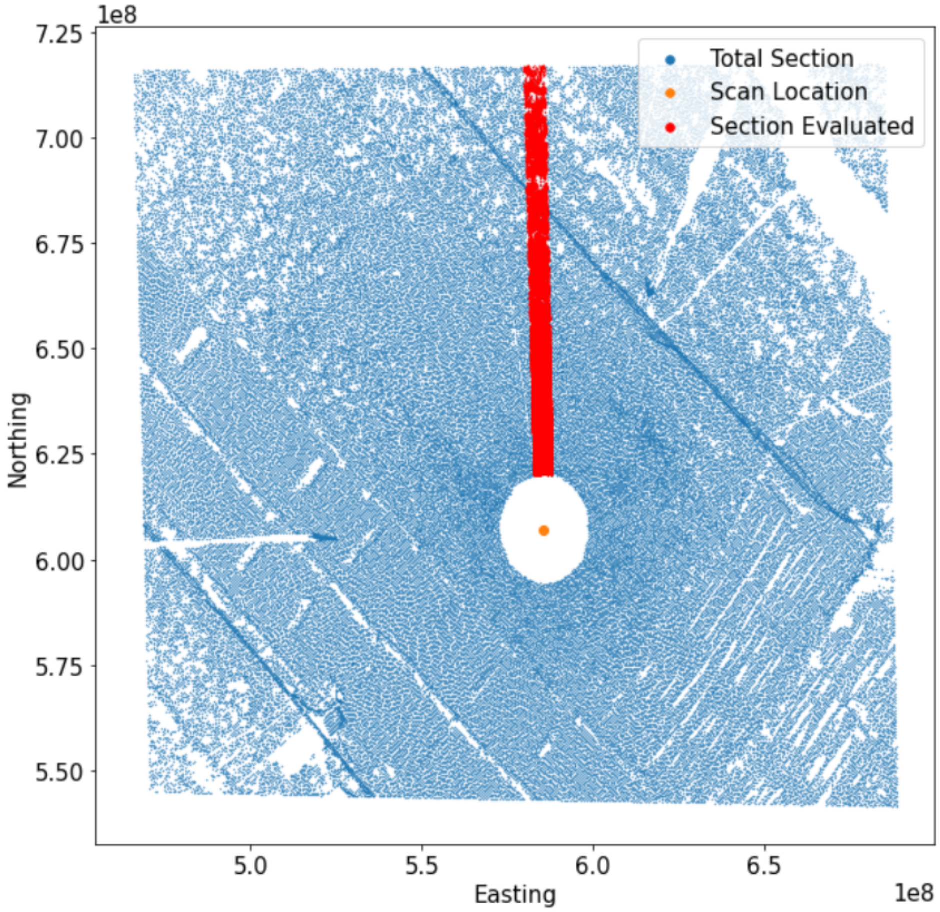

Figure 5.17: Point cloud of a single TLS scanning position from the March 2022 survey.

The red section from Figure 5.17 is shown again in Figure 5.18 but now zoomed to its full extent. In the figure one can see how close to the TLS location, in dark blue, the points provide near full coverage with little gaps. Further away, in the green or yellow area, the point density has dropped significantly with larger gaps in point coverage. The section has been spatially downsampled (50 mm, as explained in Section 4.4.2) to better illustrate the decrease in point density. Very close to the TLS there are no points as the angle at which the laser scanner rotates is limited.

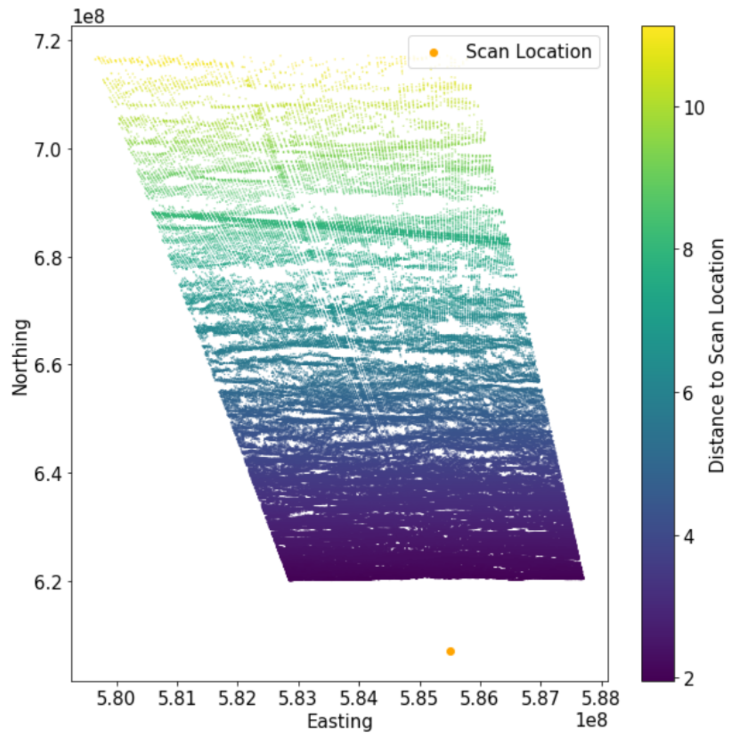

Figure 5.18: Point distnace from scan loacation of point cloud from a single TLS scanning position from March 2022. The orange dot represents the location at which the TLS stood.

Next, the data from the cropped section shown in Figure 5.18 is placed into a histogram (Figure 5.19). It is again clearly visible how at at increasing distance to the laser scanner the point density drastically drops off.

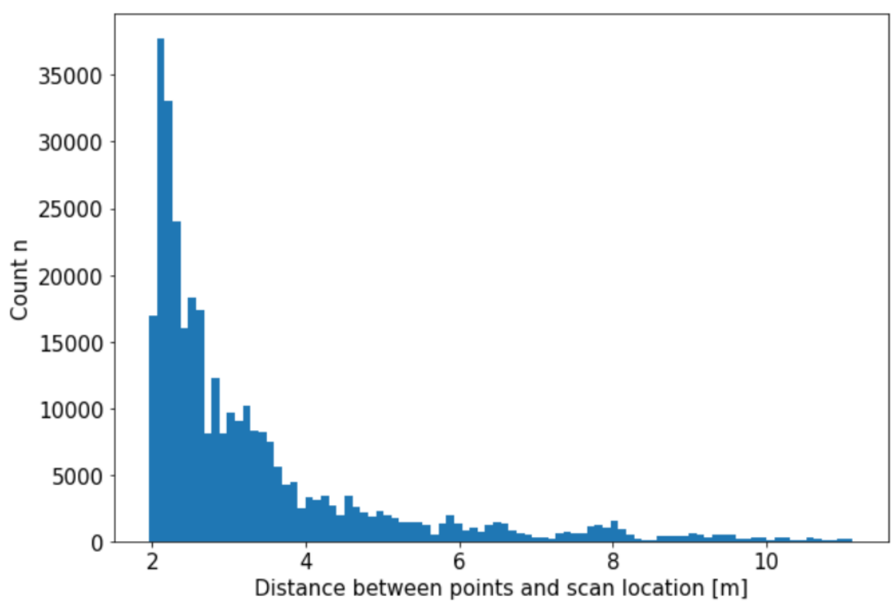

Figure 5.19: Histogram of point distnace to scan location of a point cloud from a single TLS scanning position from March 2022.

Figure 5.20 shows the roughness histogram of several cropped regions, to benchmark the performance of the methods at capturing these different areas. Roughness is a measure of how much the points deviate from a plane fitted to its nearest neighbours within a user defined region. For Figures 5.20a and 5.20b a flat roof section was chosen (shown on the right in Figure A.6) and subsequently cropped. Figures 5.20c and 5.20d are from a vertical section of facade (shown on the right in Figure A.7). Finally, Figures 5.20e and 5.20f originate from a grass patch on the top of the landfill. All cropped sections are roughly 2 by 2 meters in size. Whereas the histograms of the ALS scans show a relatively similar profile, no matter which crop is chosen, the TLS scans show vastly different profiles. As the TLS scanning locations are mostly at the same elevation, all scans hit the planar surfaces at roughly the same incidence angle. This is irrespective of distance from the scanning location to the scanned object. Due to this the TLS was able to precisely measure the planar surfaces, especially the vertical planar section from Figure 5.20c, as shown by the low roughness values. This also holds true for Figure 5.20a, but to a lesser extent due to the angle of the slanted roof section.

Figures 5.20b and 5.20d of the ALS data show significantly more roughness than the TLS. As the UAV scans the section at a larger range of incidence angles, due to it flying around both near and far away, noise and therefore roughness is created. This noise is caused by the small inherent distance measurement error of the laser scanner. The grass patch histogram of both methods show similarity, unlike those of the planar crops. The grass may have a high enough inherent roughness due to the varying lengths of vegetation that it overshadows method-related roughness. Density also has an effect on roughness, planar surfaces return a higher amount of signals to the scanner than vegetation which scatters and traps signals. The higher density of points on a structure are more easily fitted to a plane, than a sparse 'cloud' of signal returns from vegetation.

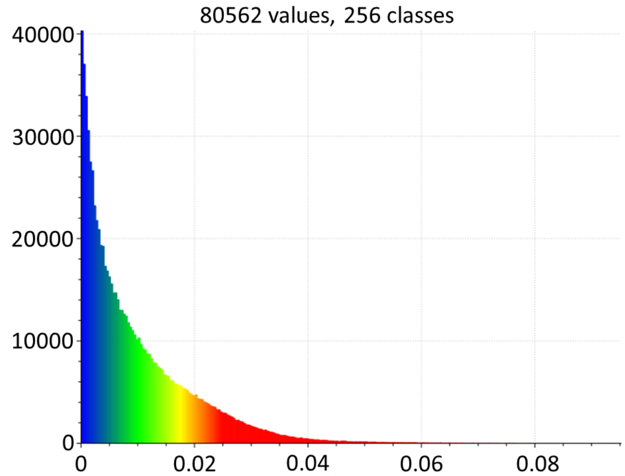

(a) Planar TLS 1

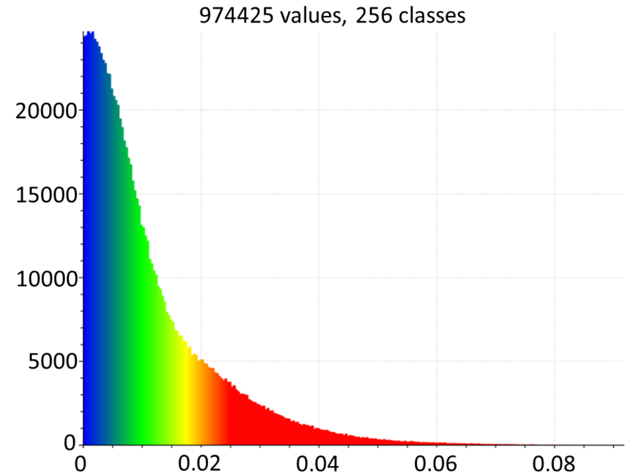

(b) Planar ALS 1

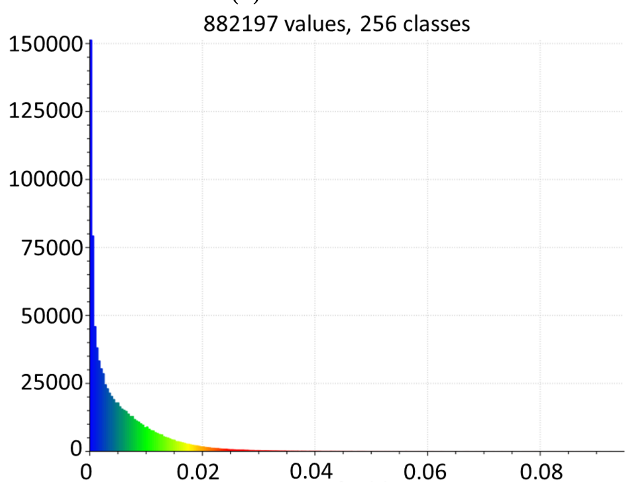

(c) Planar TLS 2

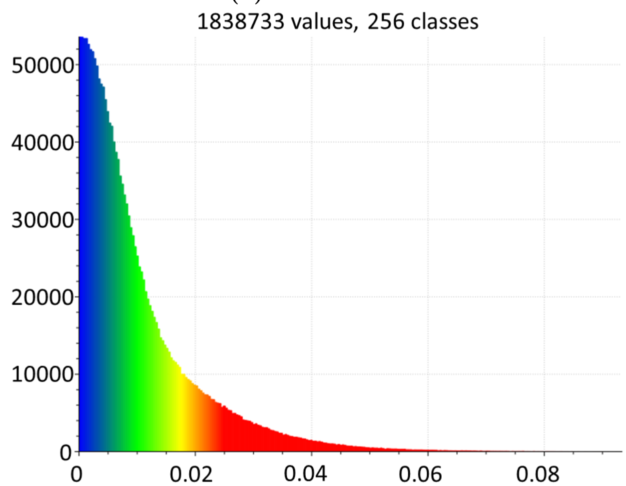

(d) Planar ALS 2

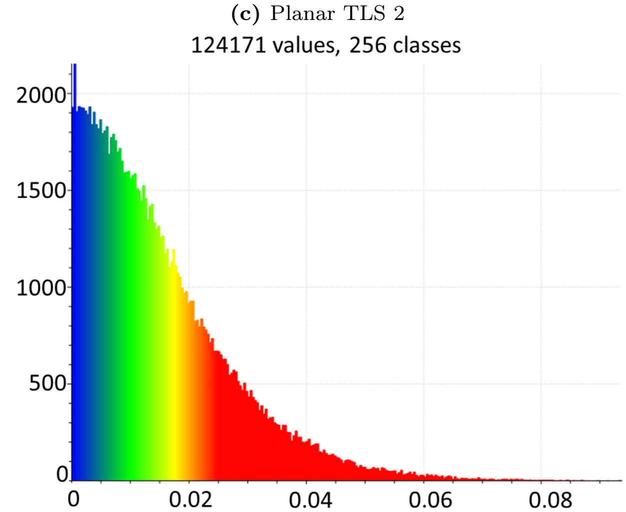

(e) Grass patch TLS

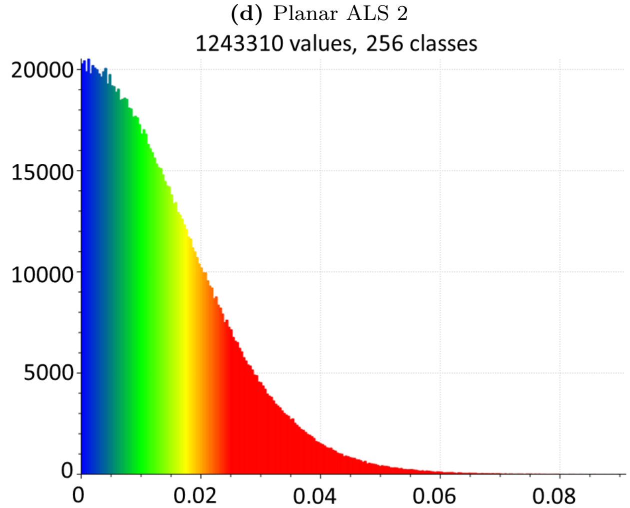

(f) Grass patch ALS

Figure 5.20: Histograms of the roughness of March 2022 ALS and TLS scans at different cropped zones. Roughness (within a 0.1 m radius cylinder) on the horizontal axis and histogram count on the vertical axes.

This increased roughness is also visible when comparing different sections, such as the circular pole shown in Figure 5.21. Note here that due to the roughness, or noise, the pole also appears to have an increased diameter when compared to the TLS cloud. This effect is also visible in square poles. The increased roughness could be partially attributed to the great at which the UAV scans the landfill, but as there are no ALS scans available at different heights this could not be verified. The roughness increases slightly at greater distances to a TLS scanning location, but within the extent of the available point clouds it does not reach the roughness of the ALS.

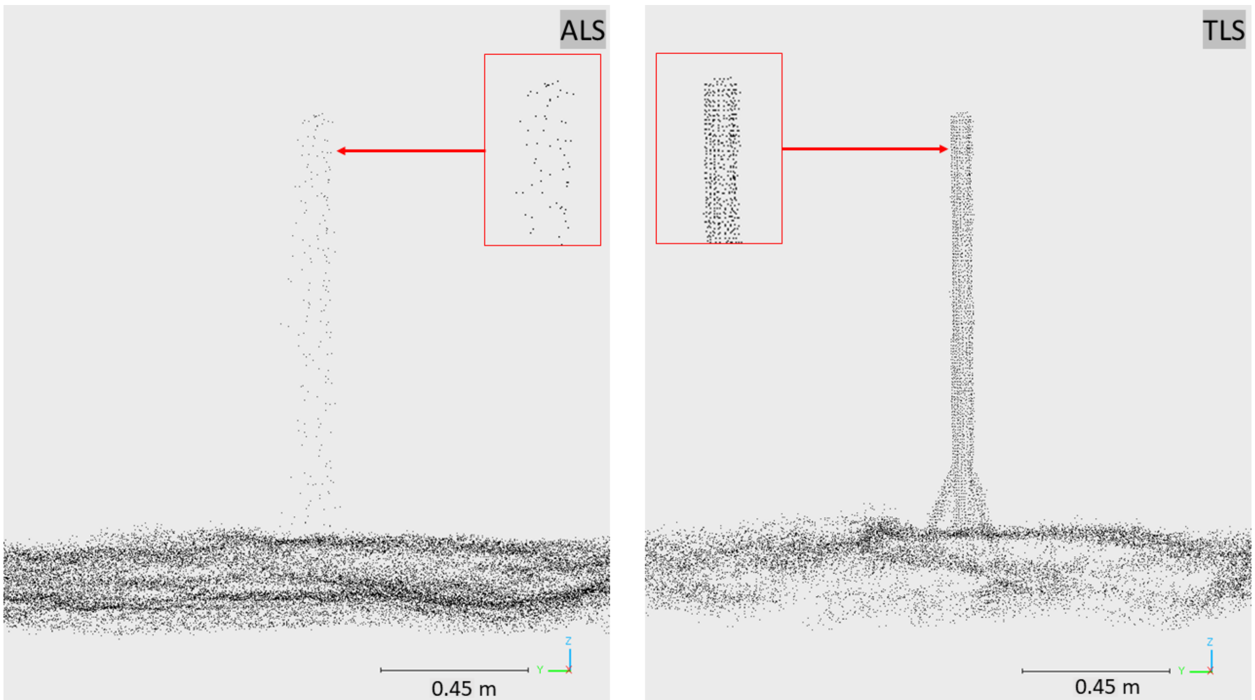

Figure 5.21: Comparison of a metal pole in the 2022 ALS and TLS point clouds, red boxes indicate a zoomed in crop.

5.3.1 Elevation obtained from method

Arguably the most important aspect of the data acquisition methods under review is their ability to accurately measure the height of the landfill from the generated DTM. Therefore, a comparison was made between the elevations measured by each method. Note, this is purely elevation at a single date compared, the settlement stemming forth from the difference in height between surveys is covered in Section 5.4. In Figure 5.35 the elevation measured by the GNSS device is first shown, after which the difference between the GNSS elevation and the elevations measured by the ALS and TLS are shown. The difference in elevation from the ALS and TLS point clouds and GNSS measurements are found by using the M3C2 algorithm on the point clouds at the locations of the settlement plates, providing an averaged elevation near the plate. The LiDAR results within this section use point clouds processed using the Cloth Simulation Filter and rasterized, the results from these processing steps are shown in Section 5.4. As such the point clouds are not digital surface, but digital terrain models.

(a) Elevation of the settlement plates as measured by the Stonex S10

(b) Difference between GNSS and TLS elevation measurement

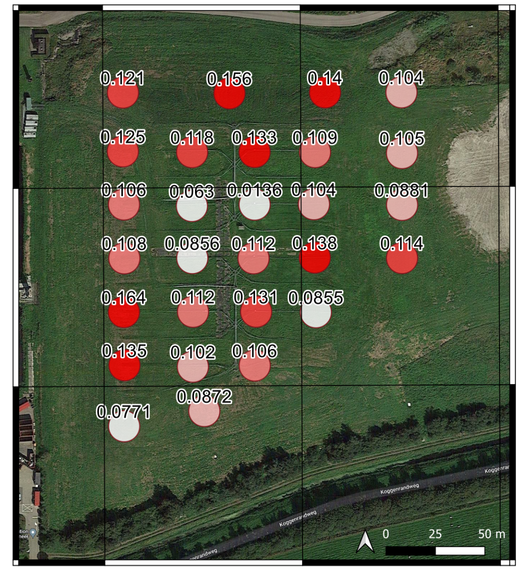

(c) Difference between GNSS and ALS elevation measurement

Figure 5.22: First, in 5.22a the elevation of each settlement plate measured by the Stonex S10 GNSS device for the March 2022 survey. Second and third, in 5.22b and 5.22c the difference between the Stonex and the ALS and TLS point clouds. The height from the LiDAR data originates from 0.5 m M3C2 cylinders. A positive difference value indicates a higher elevation than that measured by the Stonex. Figure 5.22b is missing plate measurements due to the limited extent of the point cloud. Scale of the figure and labels in meters. Note that the circle size does not represent a parameter but is instead arbitrary, and that the color scale is not consistent between the three figures.

Next, it is investigated to which extent the GNSS measurements of the settlement plate represent the overall landfill area. The 28 plates are sparsely spread over the landfill with large gaps in between, as such it is important to know how variable the landfill is in between these plates. To investigate this the difference in elevation between the GNSS measurement and the LiDAR data over increasing areas is compared. This can be seen in Figure 5.23, where the horizontal axis represents an increasing M3C2 cylinder. On the vertical axis the difference, or distance, between the GNSS measurement and the M3C2 result is shown. The difference at each of the M3C2 radii is available in appendix Tables 15 and 16.

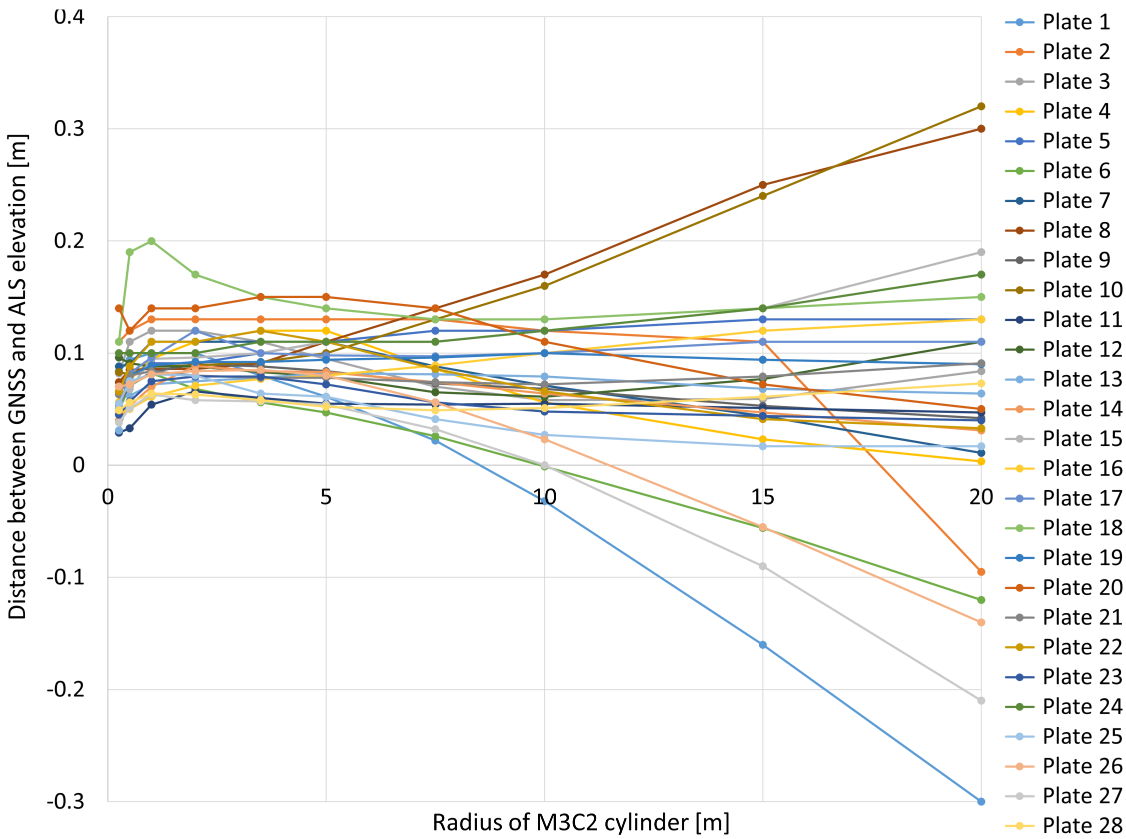

Figure 5.23: The difference between the elevation measured by the Stonex S10 GNSS and the ALS M3C2 derived elevation (March 2022).

To quantify the spatial extent of the variability Figure 5.24 was made using the data from Figure 5.23. Shown in this figure (5.24) is the M3C2 cylinder radius at which the difference in elevation as compared to a 0.5 m radius is larger than 5 cm. In essence, this means that if with 0.5 m radius M3C2 the elevation is found to be 6.000 m, and at 5 m radius the elevation is 6.051 m, the threshold of 5 cm has been reached thus the circle size is set at 5 m. This 5 cm threshold value was determined from the settlement measured by the GNSS rover, as 5 cm is outside of the LiDAR acquisition error and within the observed settlement at some plates. The upper limit was set at a 20 m M3C2 radius due to memory limitations and encroachment onto other nearby settlement plates. Note the threshold and radii values depend on the environment in which this analysis is to be done. As the top of the landfill surface is flat these values were chosen. This step is shown for ALS in Figure 5.24a and repeated for the TLS data in Figure 5.24b. The differences in settlement obtained from the data is further covered in Subsection 5.4.1

From Figure 5.24 it can be observed that at the crest, or top, of the landfill both methods indicate there is low variability in the profile of the landfill. This can be attributed to it being flat, which is well represented in the LiDAR data. At the outer edges were the landfill is sloped the variability increases as the radius at which the difference remains smaller than 5 cm decreases. Due to the limited extent of the TLS data some of the outer plates are missing as there are no points in the point cloud near these plates.

(a) ALS March 2022

(b) TLS March 2022

Figure 5.24: Distance in meters at which the change in the differences between the GNSS elevation and the averaged M3C2 ALS/TLS elevation from a 0.5 m M3C2 cylinder was within 5 cm. Radius of the circle is set according to this distance, correctly scaled to the satellite imagery in the background.

5.4 Settlement from LiDAR

First the cloth simulation filter is applied, which removed the aeration infrastructure, humans, TLS tripods and very tall vegetation. The values were tuned and iterated upon until no further gains could be made, the final settings are shown in the caption of Figure 5.25. The dense red areas in the left and top of Figure 5.25a are the slopes of the landfill which had taller vegetation than the top (or crest) of the landfill. The very dense rectangles (asphalt) at the top of this figure are outside of the landfill area and therefore ignored, as is the dense area in the northeast.

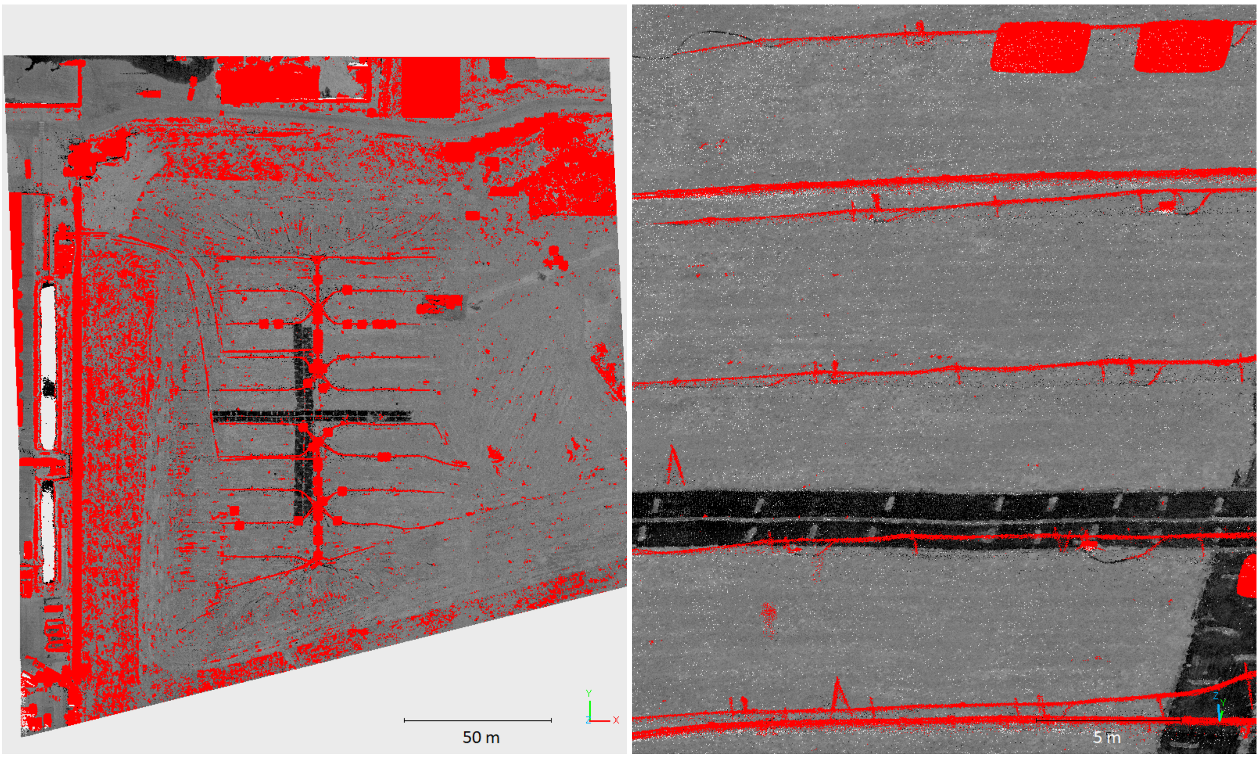

(a) Overview **(b)** Zoomed in

Figure 5.25: Example of results achieved using the Cloth Simulation Filter algorithm on the 2022 March ALS point cloud, in red the off-ground points and in gray the ground points (Cloth resolution = 0.5, Iterations = 2000, Threshold = 0.1, slope processing on, Relief). Scale in meters.

Once all point clouds were processed, Figure 5.26 provided some initial visual confirmation that changes have occurred on the top of the landfill in between the scanning days. The differences in height seen in this figure are, at their maximum, in the range of 10 centimeter. This is larger than the registration and distance measurement errors of both methods (Sections 5.2 and 3.3), indicating that this is real settlement of the landfill and not errors in (pre-)processing. The ground settlement plates show a similar settling trend as seen in Figure 5.26, but with lower absolute values of settlement.

In Figure 5.26 the TLS point clouds from July and August are slightly to the right of the others, separate from the May 2021 and March 2022 clouds. This is due to the less accurate registration of these scans, as there was no ALS data available from the same date to improve the registration on the top of the landfill.

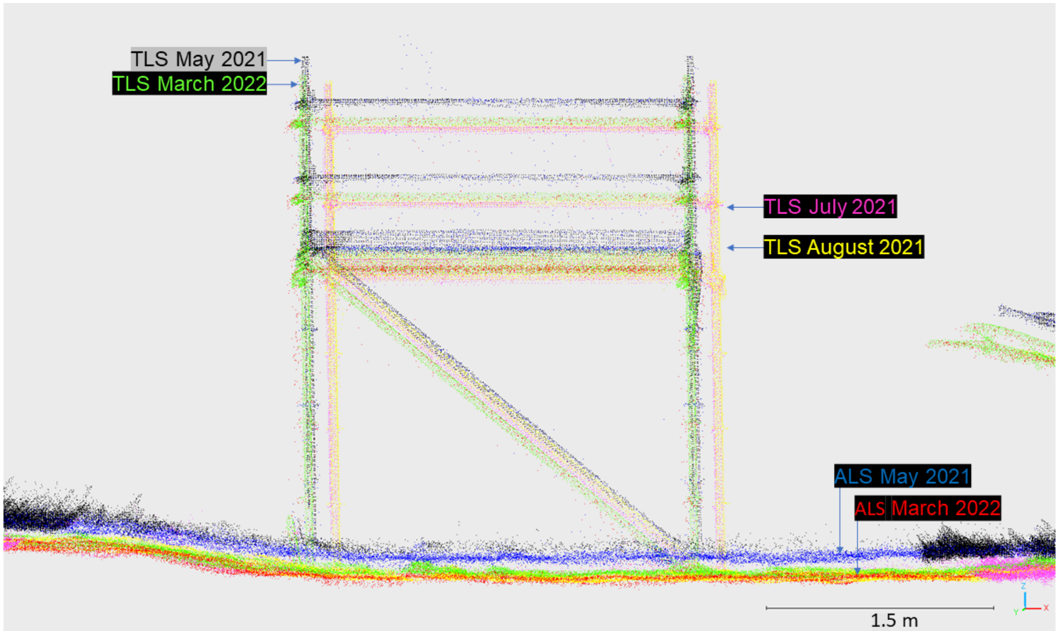

Figure 5.26: Cross section of scaffolding on top of the landfill showing all available LiDAR data. Point cloud shown prior to CSF being applied.

To verify whether the differences between scans seen in Figure 5.26 can be potentially attributed to settlement, and not registration or method errors, the results are verified against rigid structures as shown in Figure 5.27. The rigid structures shown are located in the west most section and were not used for registration purposes, as otherwise any differences between the scans would have been removed due to point pair picking. These rigid structures showed differences in the low centimeter range, much lower than the observed settlement.

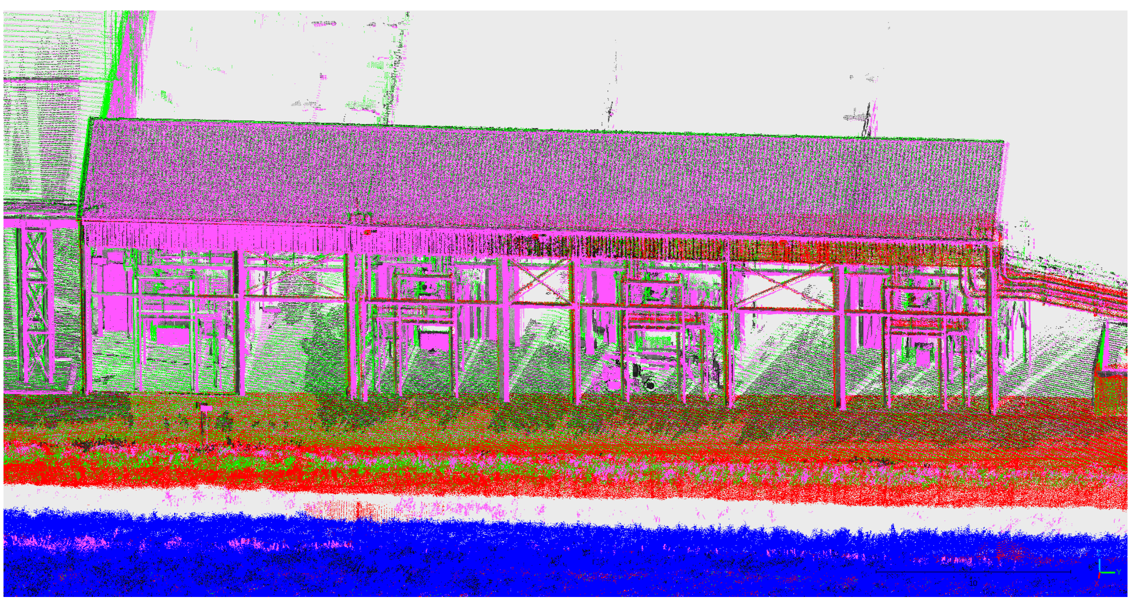

Figure 5.27: View of rigid structures to illustrate the differences from Figure 5.26, note the colouring of the point clouds is taken from Figure 5.26. Photographs of this area can be found in Appendix A. Point cloud shown prior to CSF being applied.

Then the point clouds are rasterized as previously explained in Subsection 4.2.2. After testing various grid sizes eventually a choice was made for 15 cm by 15 cm cells. Smaller cells negated the 'penetration' effect, whilst further increasing the cell size introduced artifacting and an undesired amount of data loss due to averaging.

The differences between the rasterized and non-rasterized point clouds is shown in Figure 5.28. The top of the landfill, devoid of tall vegetation shows only small changes after being rasterized. The exception are some patches of slightly taller vegetation, and a piece of aeration infrastructure near the middle which was not filtered out by the CSF algorithm. The outer areas of the figure, which contain denser and taller vegetation, show significantly larger (>5 cm) changes.

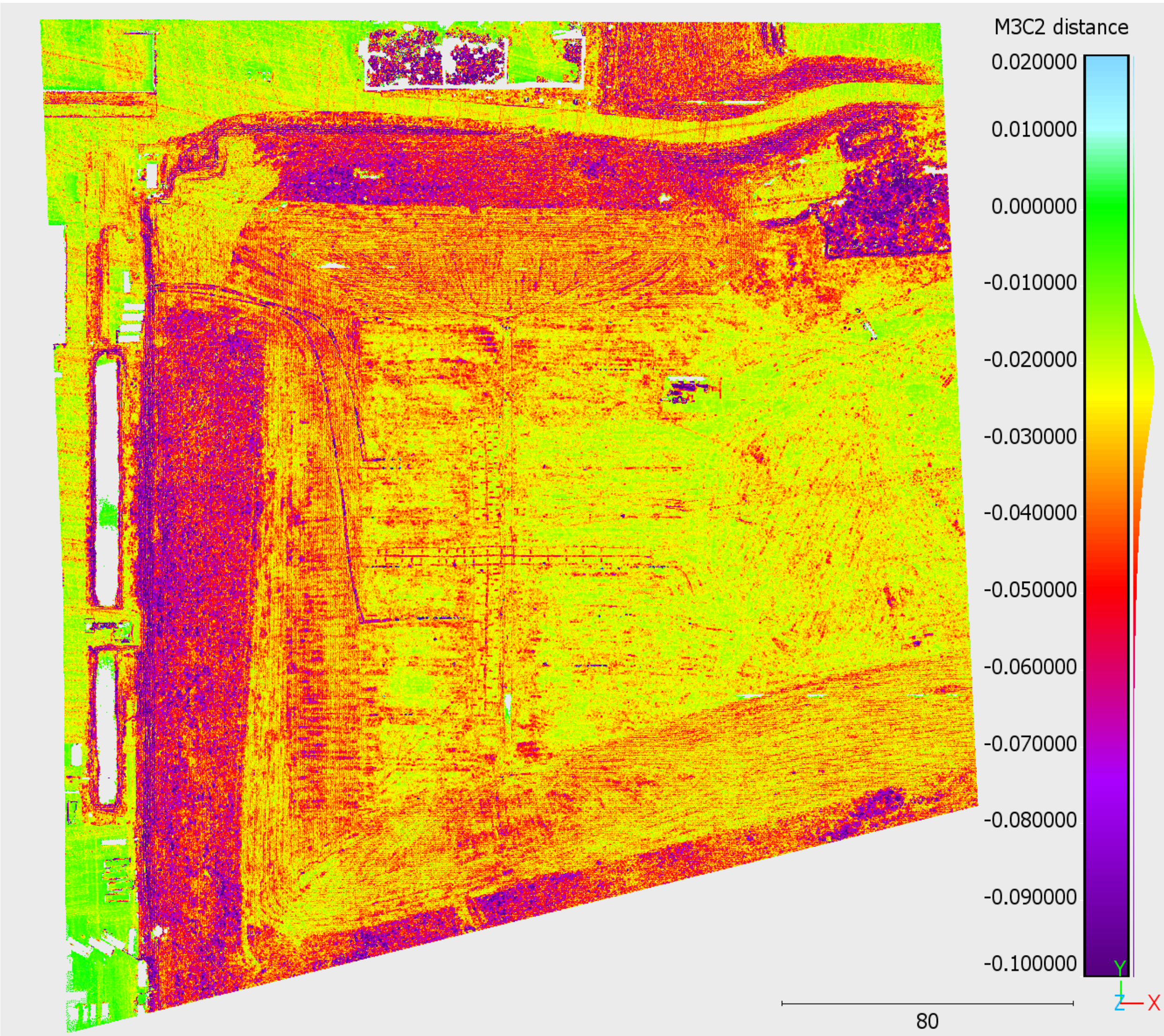

Figure 5.28: Differences caused by rasterizing (15 cm) the March 2022 ALS point cloud. A negative value in the color bar (in meters) corresponds to a decrease in elevation after rasterization. Scale of both point cloud and color bar in meters.

Next, the M3C2 algorithm (Subsection 4.6) is used to quantify the changes between the point clouds from different dates, which is a measure of the settlement that has occurred in between these dates. The two ALS scans dating from May 2022 and March 2022 are first processed using M3C2 with a cylindrical diameter of 0.25 centimeters, shown in Figure 5.29. This is repeated for the TLS scans of the same data in Figure 5.30, unfortunately the May 2021 TLS point cloud is of a much smaller extent, only covering part the middle section of the landfill. Areas where one point cloud contains data, but the other does not are shown in dark gray.

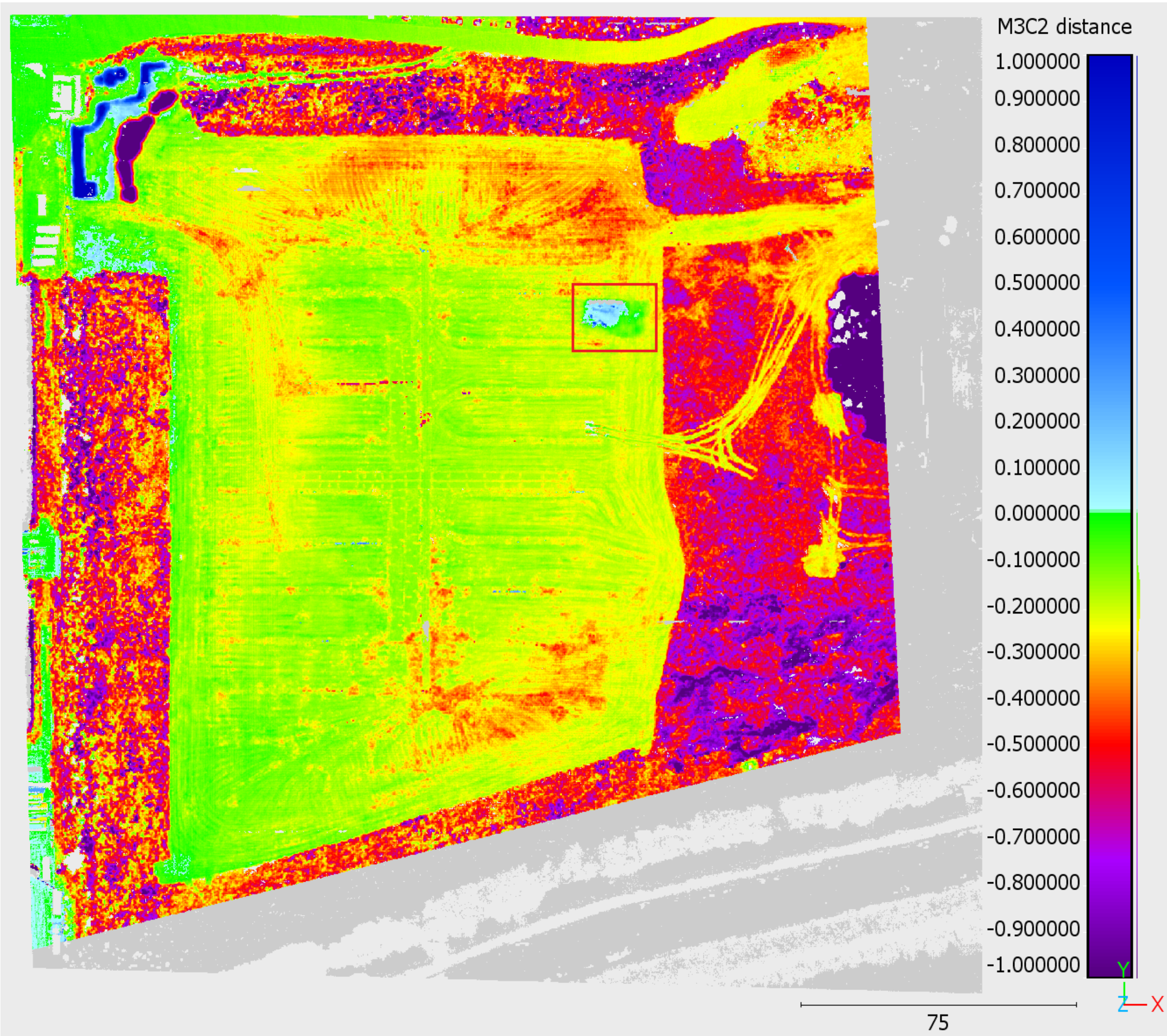

Figure 5.29: M3C2 signed distances between the ALS point clouds of May 2021 and March 2022, a negative value indicating settlement. Grey areas indicate no matching points between the two scans. The red rectangle marked near the middle of the figure indicates a storage site for materials and does not reflect the settlement of the landfill surface. Scale of both color bar and point cloud in meters.

Both the ALS and TLS settlement products show similar trends in computed distances, wit the top of the landfill showing settlement ranging anywhere from 0 to 25 centimeters with smaller red areas of upwards of 50 cm. The outer areas in the west and east show significantly higher settlement values. This is caused by the presence of high vegetation in these areas in the 2021 scans, which were mowed prior to the 2022 scans. In Figure 5.29 a dark blue area can be seen in the upper left of the figure, this is a soil mound added in between the scans. In both figures faint lines can also be seen around the north and eastern sides of the landfill, these are tire tracks. Notably the tire tracks show smaller changes than the nearby vegetated areas.

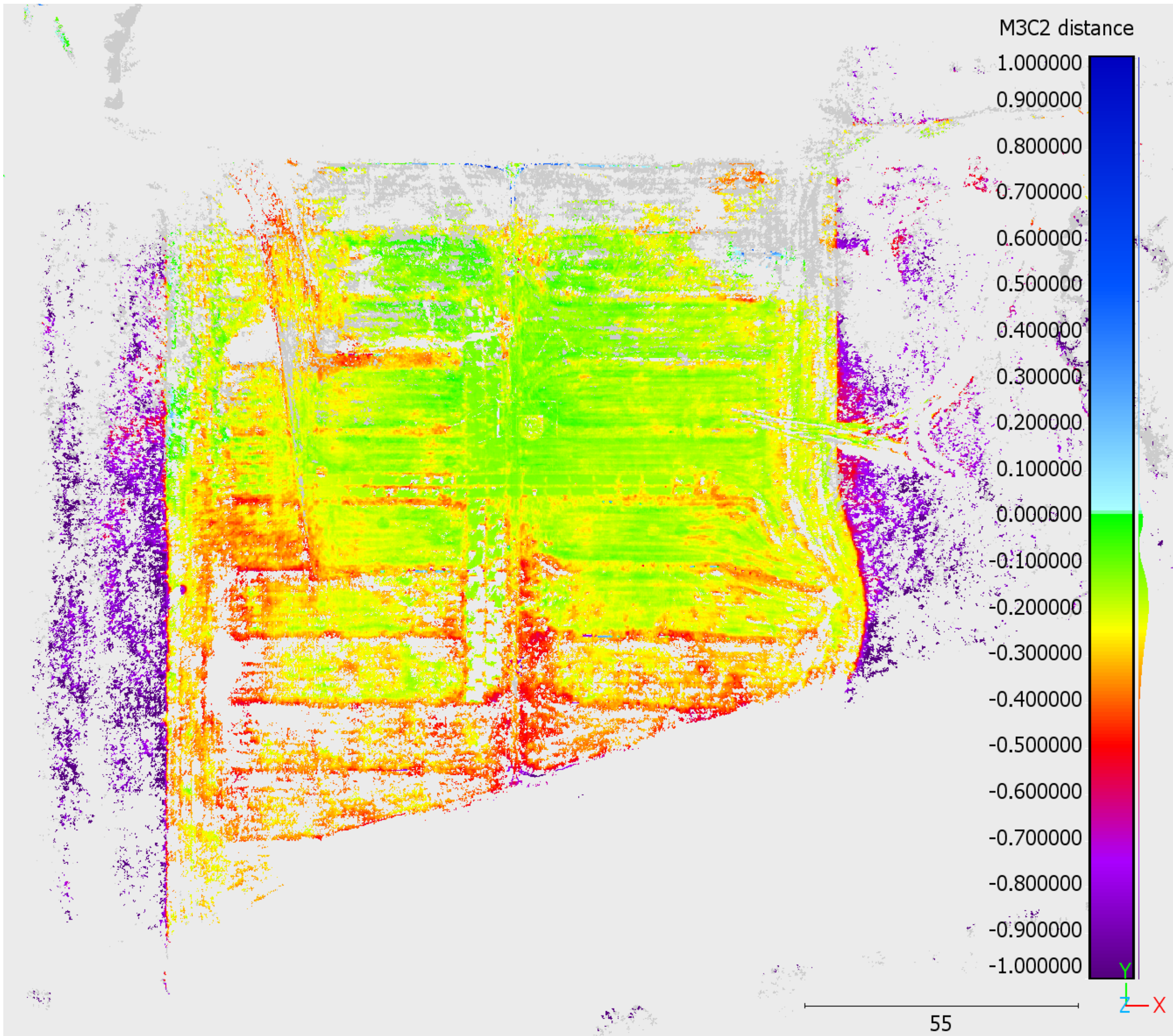

Figure 5.30: M3C2 signed distances between the TLS point clouds of May 2021 and March 2022, a negative value indicating settlement. Grey areas indicate no matching points between the two scans. Scale of both color bar and point cloud in meters.

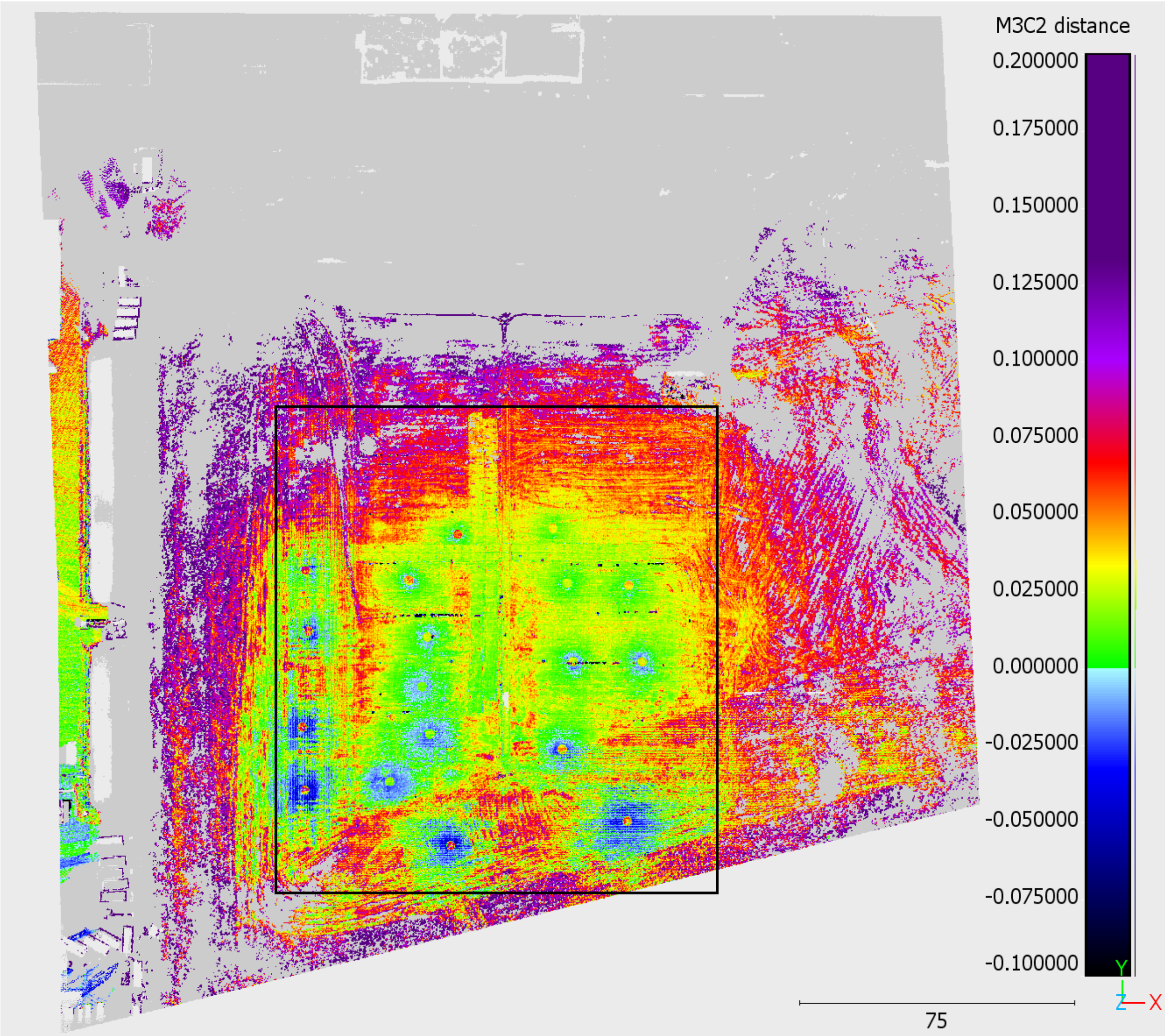

Figure 5.31: M3C2 signed distances between the TLS and ALS point clouds of March 2022, a positive value indicates the ALS height value was lower than the TLS. The black rectangle indicates the area cropped for Figure 5.32. Note that the color bar used for this figure differs from the previous figures. Scale of both color bar and point cloud in meters.

In Figure 5.31 the TLS and ALS scans of the same date (March 2022) are compared using M3C2. This is to investigate the difference in measured heights when the scans were performed on the same date. Any differences in height can then only be attributed to the method itself, assuming that the wind remained relatively constant and did not impact the vegetation significantly. The distances are significantly lower than those observed in the settlement figures (Figures 5.29 and 5.30), giving extra credibility to the settlement data. Larger differences are observed on the slopes and in the upper north, at greater distance to the TLS scanning locations.

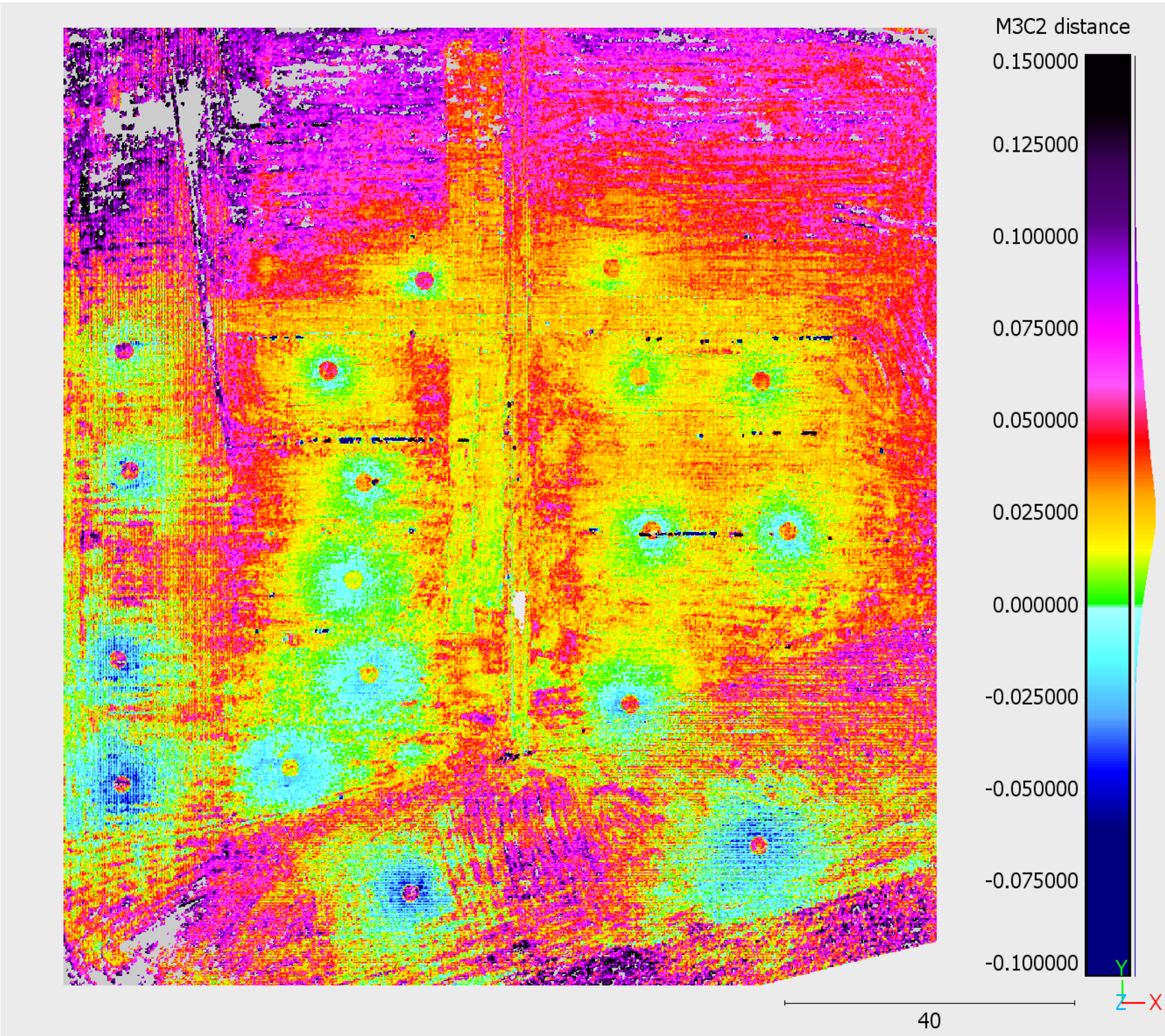

Figure 5.32: Cropped M3C2 signed distances between the TLS and ALS point clouds of March 2022, a positive value indicates the ALS height value was lower than the TLS. The horizontal line segments are remnants from the aeration infrastructure, incorrectly marked as ground points. Scale of both color bar and point cloud in meters.

An area of Figure 5.31, marked by the black rectangle, is cropped and shown in Figure 5.32. The color bar is also adjusted for the range of values in this newly cropped figure. This increase in differences mentioned earlier is even more apparent when looking at a zoomed in section on the top of the landfill. At increasing distance to a scanning location (the circular shapes visible in Figure 5.32) the differences between the ALS and TLS measured elevation increases. Very near to the TLS scanning locations a reversal occurs where the TLS point cloud lies 'below' the ALS cloud, giving a lower elevation. The criss cross pattern of faint lines visible in Figure 5.32 are visual artefacts in the 3D renderer from the rasterization process and do not impact the data itself.

The previous figures were focused on the ground points extracted by the CSF algorithm. It was hypothesised that the off ground points, which mainly consists of the aeration structure that is present on the top of the landfill, could be used to measure the settlement. The aeration structure should not be influenced by vegetation as it is suspended above the ground surface. The M3C2 derived settlement from the off ground points is shown in Figure 5.33.

Unfortunately, as can be seen in Figure 5.33, this hypothesis did not hold up. Beneath the aeration structure some points are included from the tallest vegetation present. This is a desired effect for the purposes of removing vegetation from the ground points, but here it causes the M3C2 process to incorrectly compute settlement as the mean elevation at these pipes is shifted downwards due to the vegetation. This in turn causes settlement to turn negative upwards to 1.13 m near the elevated sections of the aeration infrastructure in the center of Figure 5.33.

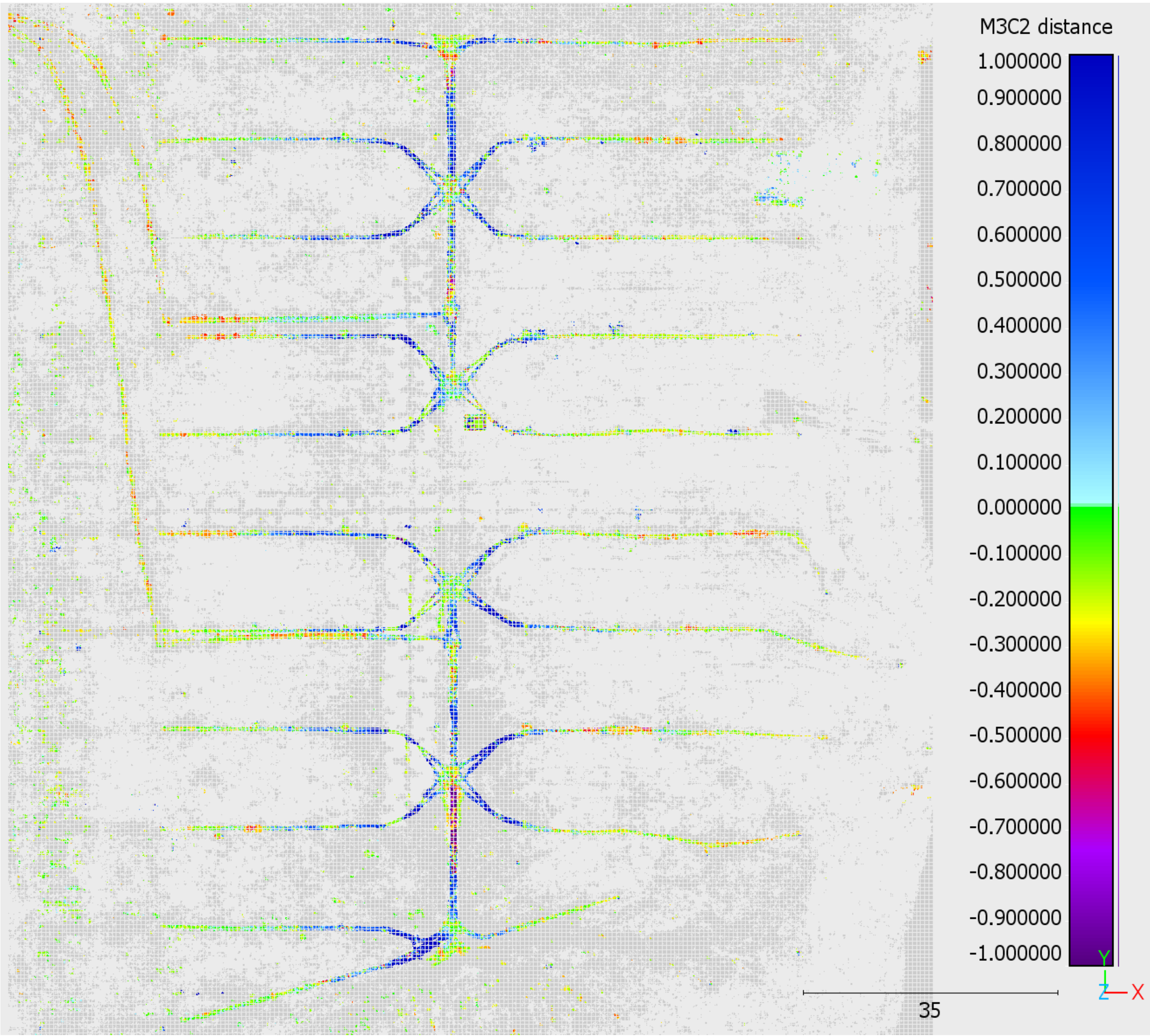

Figure 5.33: M3C2 signed distances between the ALS point clouds of May 2021 and March 2022 using the off ground points from the CSF algorithm, a negative value indicating settlement. Grey areas indicate no matching points between the two scans. Scale of both color bar and point cloud in meters.

The TLS scans of July 2021 and August 2021 were not covered in this section due to the poor quality of the elevation/settlement retrieved when using these two point clouds in combination with each other, or with the TLS scans of May 2021 or March 2022. The TLS M3C2 settlement products from July 2021 to March 2022 can be found in Figure C.4, from August 2021 to March 2022 in Figure C.5. Figure C.4 contains significantly higher than expected settlement, as well as areas of negative settlement due to a large amount of vegetation being present in the July point cloud. Figure C.5 has an incorrectly registered scanning location in the southwest of the point cloud, as well as a significant tilt which introduces a gradient in the settlement from the southwest to the northeast. The tilt was caused by the earlier mentioned difficulties registering the point clouds due to there being no tie-points available on top of the landfill.

5.4.1 Comparing GNSS against LiDAR settlement

From Subsection 5.3.1 the elevation measurements of the acquisition methods were compared. Now that the settlement has also been computed the work flow from this comparison can be repeated, but now for settlement instead of the elevation. By doing so the settlement measured by each method can be more directly compared, providing a measure of the quality of the findings. The results from this comparison are shown in Figure 5.35.

The GNSS rover consistently measures the lowest amount of settlement. Whilst the GNSS data ranges from March 2021 to March 2022, the ALS and TLS data both range from 2021 May to 2022 March. Some of the differences in settlement could thus be attributed to the slightly longer time range over which the GNSS settlement was measured. However, in this two month period the expected settlement from other GNSS surveys is in the low centimeters, not anywhere close to the differences observed between Figure 5.35a and Figure 5.35b/5.35c.

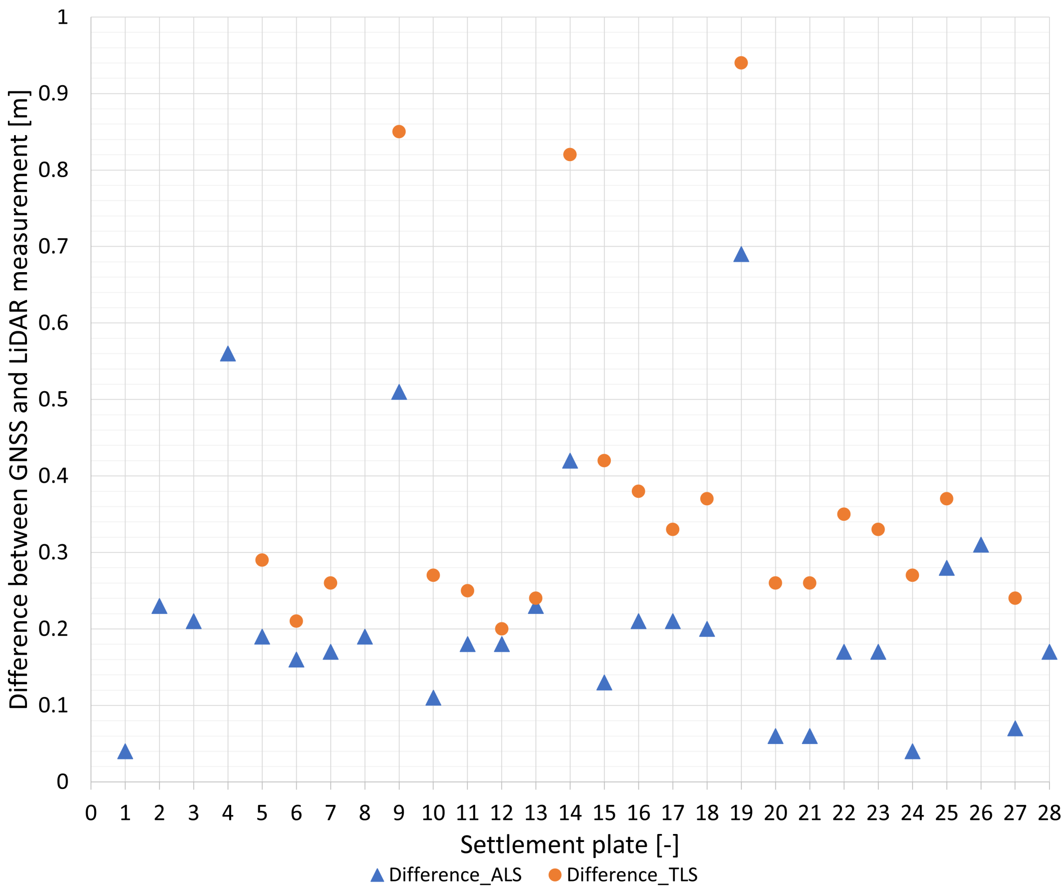

Figure 5.34: Difference in settlement values at the settlement plates between GNSS and ALS/TLS. A positive value indicates that the settlement from ALS or TLS was higher than that measured by the GNSS rover. Here higher settlement means more height decrease of the landfill.

To better visualise the comparison between the values shown in Figure 5.35, a scatter chart was made with the difference in settlement between GNSS and the laser scanning methods for each settlement plate. In this figure (Figure 5.34) it can be observed that the TLS differences reach a higher maximum, with a median value of 0.29 and a mean of 0.38 meters. The differences between the GNSS and ALS settlement has a median value of 0.18, and a mean of 0.22 meters. Settlement plates 9, 14 and 19 are significant outliers, more so for the TLS.

(a) Settlement of the plates - GNSS

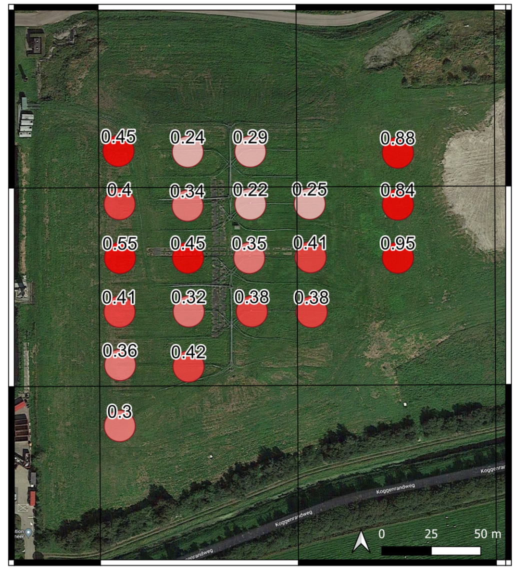

(b) Settlement of the plates - TLS

(c) Settlement of the plates - ALS

Figure 5.35: First, in Figure 5.35a the settlement between March 2021 and March 2022 as measured by the Stonex S10 GNSS rover is shown. In Figure 5.35b and Figure 5.35c the settlement from the TLS and ALS, respectively, is shown over the time period May 2021 to March 2022. The settlement from the LiDAR methods is the averaged settlement value, in meters, in a 0.5 m radius circle around the settlement plate location. In Figure 5.23 it was shown that 0.5 m provides a representative measure of the elevation and thus settlement. The scale of the figure and labels is in meters, a positive difference value indicates a higher settlement value than that measured by the Stonex GNSS rover. The color scale is not consistent between the three figures.

5.5 Settlement and carbon extraction correlation

First, the amount of carbon mass extracted by the wells is calculated as explained in Subsection 4.4.1. Both the data from the 110 gas wells, as well as the bulk flow rate from the gas blower station are utilised for the calculation. The gas wells were measured at roughly monthly intervals, totaling 62 measurements from August 2017 to March 2022. The cumulative carbon mass extracted from all wells is shown in Figure 5.36. Throughout the nearly 5 years (55 months) of measurements there is steady extraction of carbon, with no significant dips or other peculiarities.

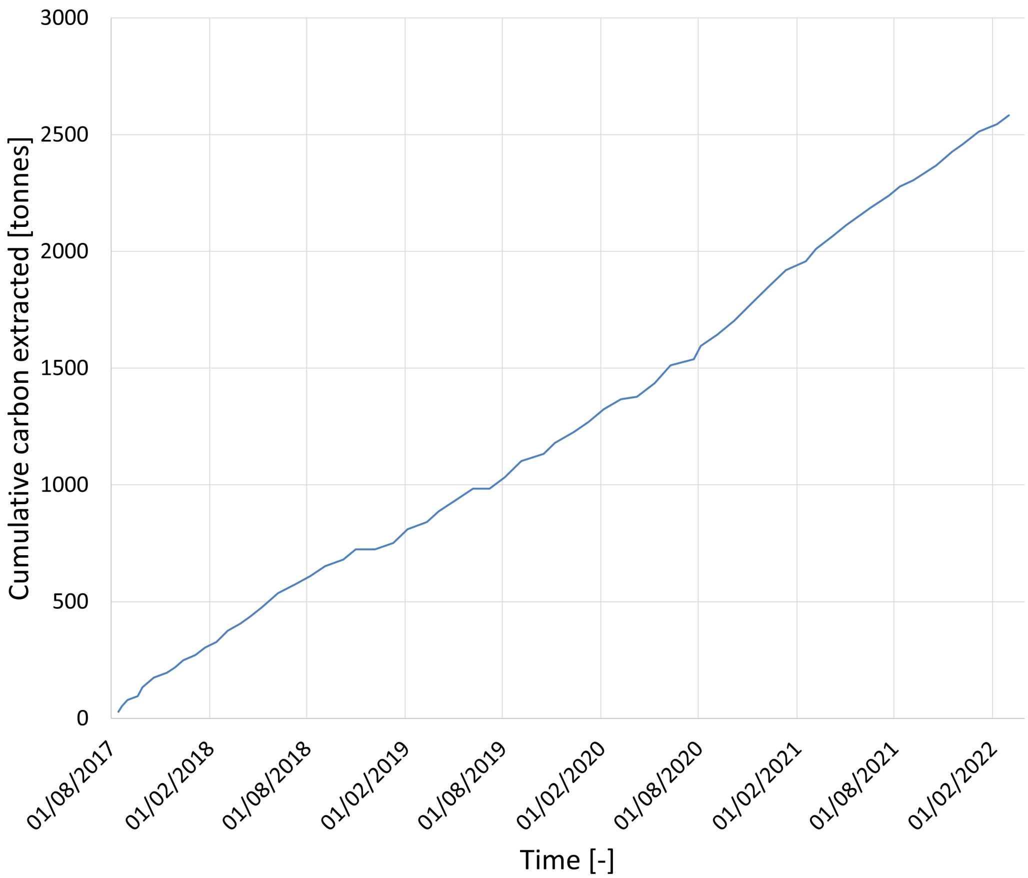

Figure 5.36: Cumulative extracted carbon mass from 110 wells between August 2017 and March 2022 in tonnes.

To investigate the spatial variability in carbon extraction it is shown for each well in Figure 5.37 over the period March 2021 to March 2022. This is the same time period as the GNSS data and nearly the same as the ALS and TLS data (May 2021 to March 2022) that were compared in Section 5.4 and 5.4.1. There are notable differences between the wells, with some very active and others nearly inert. The minimum value per well over this year of measurements is 0.0081 tonnes, maximum 11.24 tonnes and the mean 2.75 tonnes. The eastern half of the wells show generally higher amounts of extracted carbon, whilst the western/southwestern section shows considerably lower amounts extracted. Nonetheless, no clear pattern or trend can be observed, with some very inactive wells lying right next to very active wells such as the two bottom-most wells.

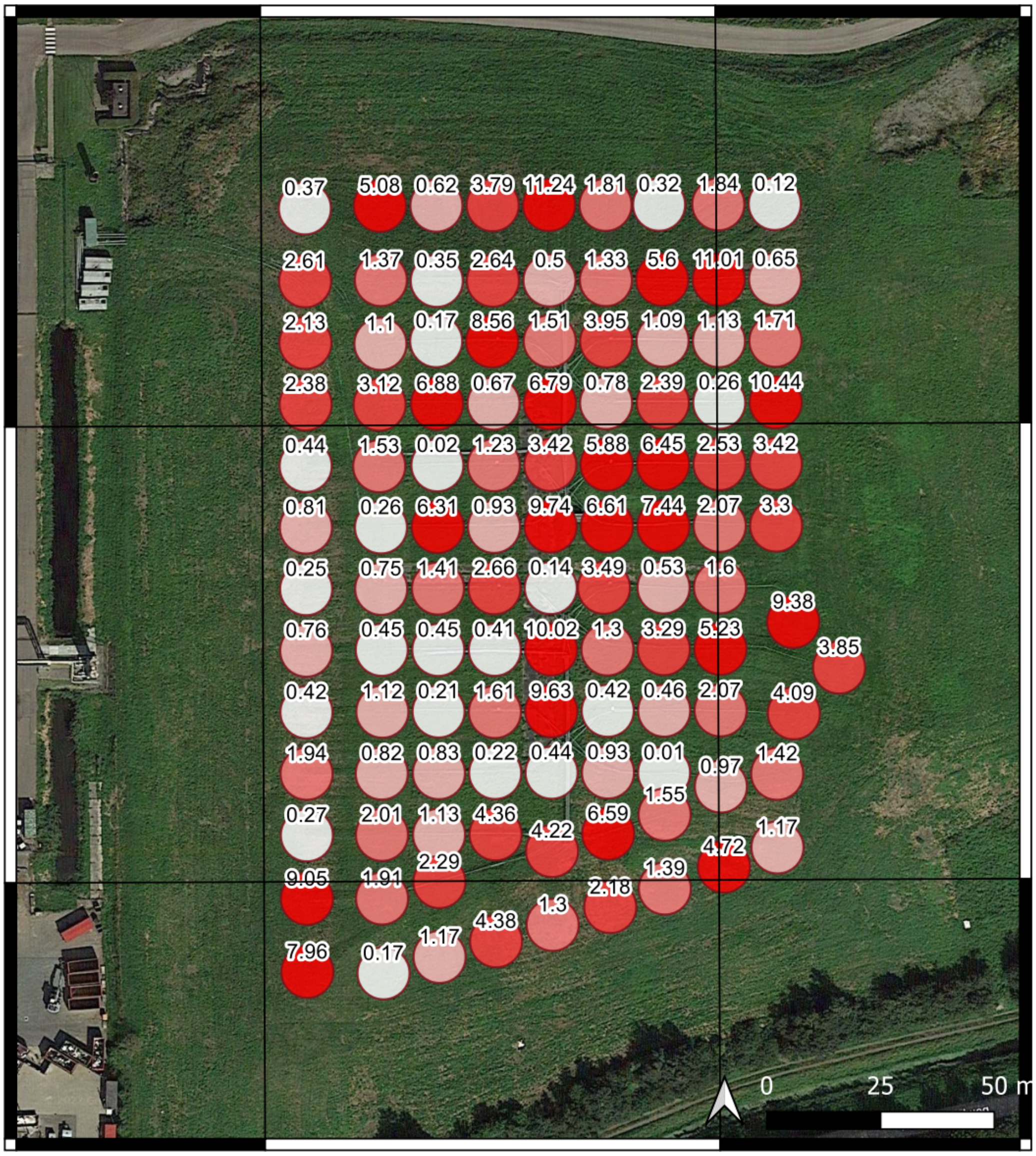

Figure 5.37: Extracted carbon mass from 110 wells between March 2021 and March 2022 in tonnes.

Figure 5.37 is shown three times in Figure 5.38, but now without labels and instead scaled according to carbon extraction value. Placed next to these three figures (5.38b, 5.38d, and 5.38f) are settlement figures of the three acquisition methods (5.38a, 5.38c, and 5.38e) over the period May/March 2021 to March 2022.

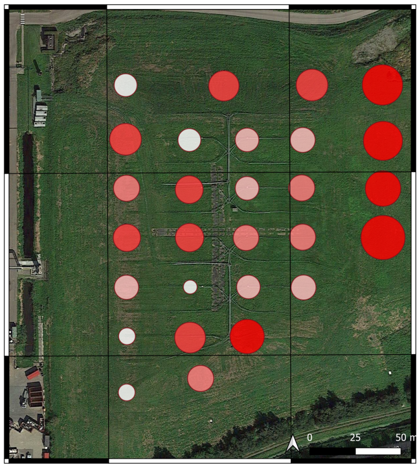

(a) ALS

(b) Extracted carbon

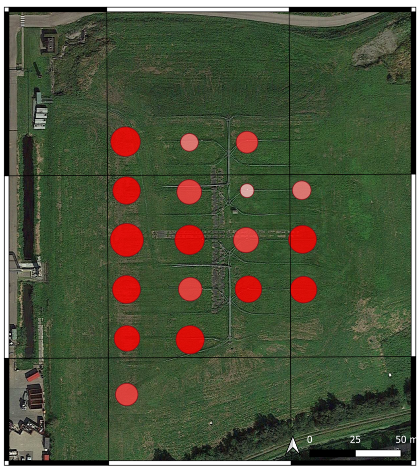

(c) TLS

(d) Extracted carbon

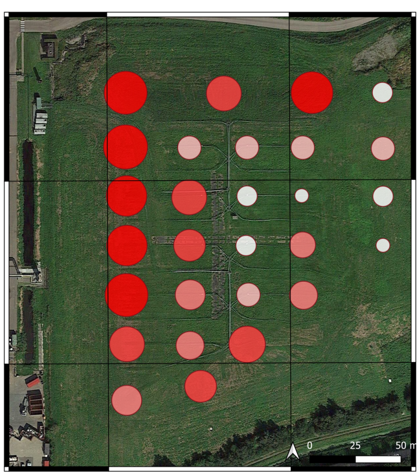

(e) GNSS

(f) Extracted carbon

Figure 5.38: Left figures (5.38a, 5.38c, and 5.38e) show settlement from May 2021 (March 2022 for GNSS) to March 2022 at the settlement plates. Scaling of circles is based on the maximum and minimum values of settlement from the respective acquisition method, independent of the other figures. The right figures (5.38b, 5.38d, and 5.38f), which are duplicates, contain the same data as Figure 5.37, except now circle size is scaled according to carbon extraction value.

From Figure 5.38 the settlement at the plates, and carbon extraction at the wells can be compared. Here again the TLS data is limited due to the smaller extent of the TLS point cloud. The GNSS measurements (Figure 5.38e) show significantly more settlement on the western slope of the landfill, the exact values can be found in Figure 5.35a. Interestingly, the western slope has comparatively low amounts of extracted carbon. When comparing the LiDAR measurements against the carbon extraction significant similarities are observed. One point of interest is the area of high carbon extraction slightly to the east of the center of the landfill which has a cluster of active wells. In all three of the settlement figures this same area shows low amounts of settlement.

A time series chart (Figure 5.39) is made of the cumulative (GNSS) settlement of plate 1 (on the northern slope), as well as the carbon extracted by the nearby well. Additionally, Figure 5.39 is made for plates 12, 15 and 22 in Figures C.7, C.8, and C.9. The distance between the plates and wells is less than half a meter for each of these figures.

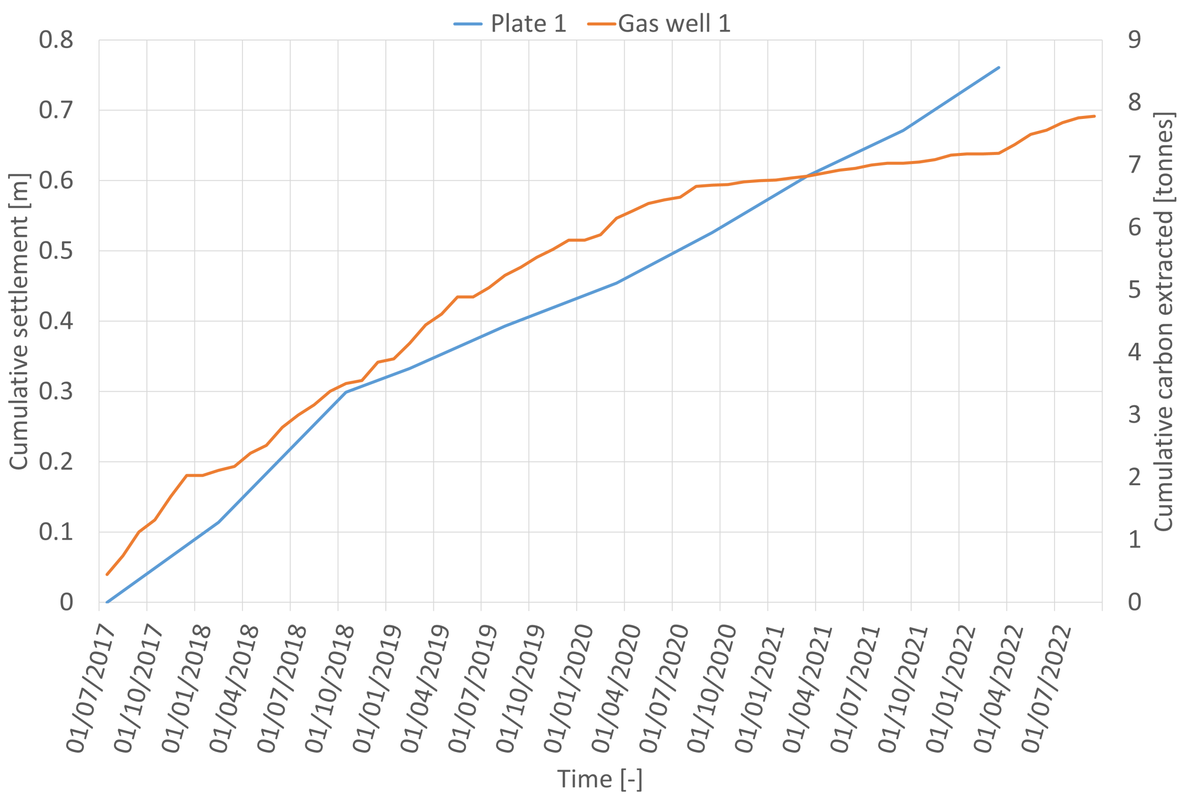

Figure 5.39: Cumulative extracted carbon mass and GNSS settlement at plate 1 and well 1 between August 2017 and March 2022. Settlement in meters, carbon mass in tonnes.

In Figure 5.40 the process is repeated but now for the 9 closest wells to the settlement plate. The same is done for plate 12 in Figure C.10. Whilst Figure 5.39 had nearly linear settlement and carbon extraction, Figure 5.40 instead shows significant changes in both settlement and extraction. Notably, in early 2022 there is an uptick in both carbon extraction and the settlement.

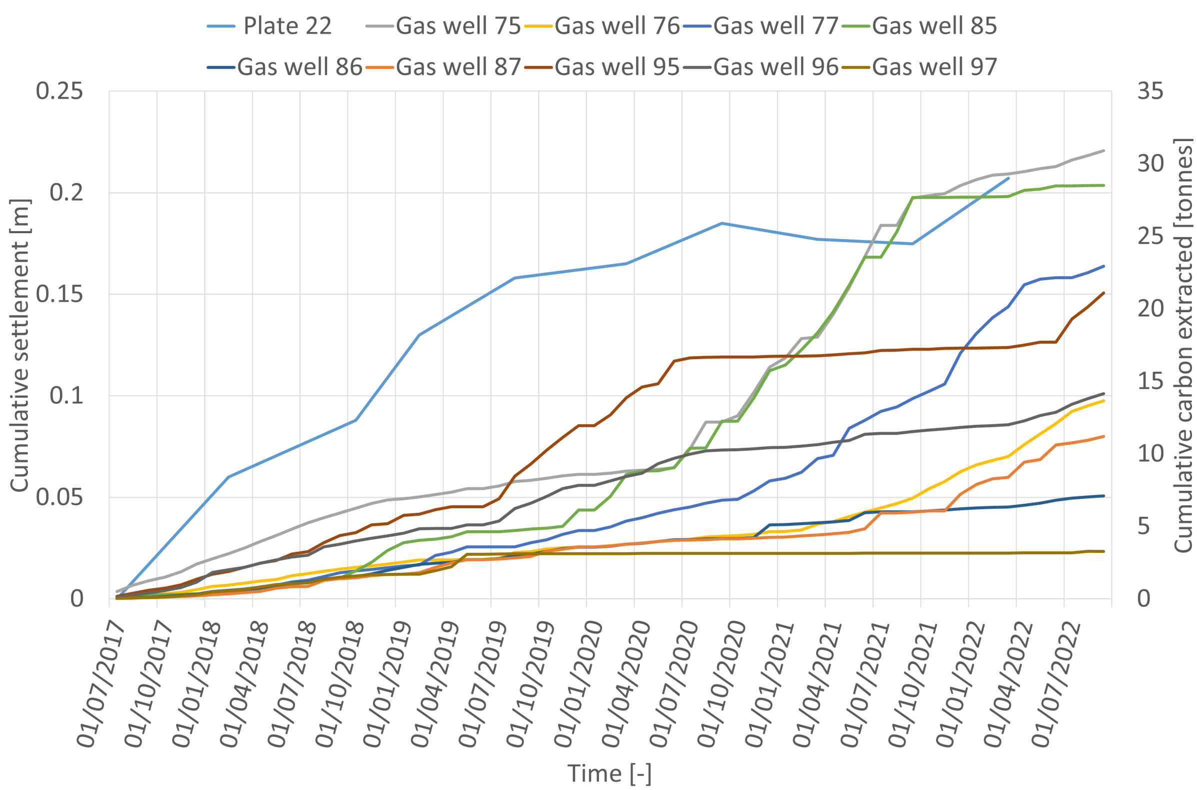

Figure 5.40: Cumulative extracted carbon mass and GNSS settlement at plate 22 and the 9 closest wells between August 2017 and March 2022. Settlement in meters, carbon mass in tonnes.

The carbon extraction data has now been compared to the LiDAR and GNSS settlement at the settlement plates, but one of the reasons LiDAR was desired is its continuous nature. Therefore, the processing pipeline explained in Subsection 4.4.1 is applied to the ALS and TLS data, to allow for an analysis of the entirety of the point clouds in between the gas wells. As input for the settlement data the M3C2 distance products are used, for example the data shown in Figure 5.29. In Figure 5.41 the results are shown of the Ordinary Kriging interpolation on the M3C2 derived settlement data. The variogram (an example is placed in the appendix, Figure C.14) is manually fitted by the sill, range and nugget values. Note that Figure 5.41 has been cropped to the outer extents of the gas wells, hence the odd cropping in the east and south of this figure.

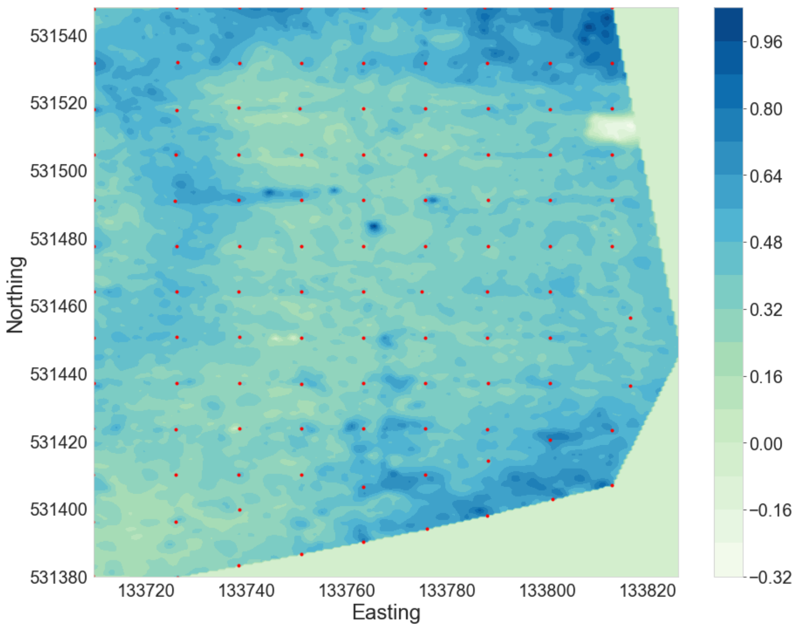

Figure 5.41: Ordinary Kriging interpolation of the M3C2 settlement data from May 2021 to March 2022. The red dots represent the locations of the 110 gas wells. The color bar indicates settlement (in meters). A positive number indicates settlement, negative uplift/heave. The greenish background colour does not represent any data, but is instead a quirk of the figure rendered used.

The interpolation process shown in Figure 5.41 is repeated for the carbon extraction data in Figure 5.42. The very active aeration wells that were visible in Figure 5.37 are again clearly visible.

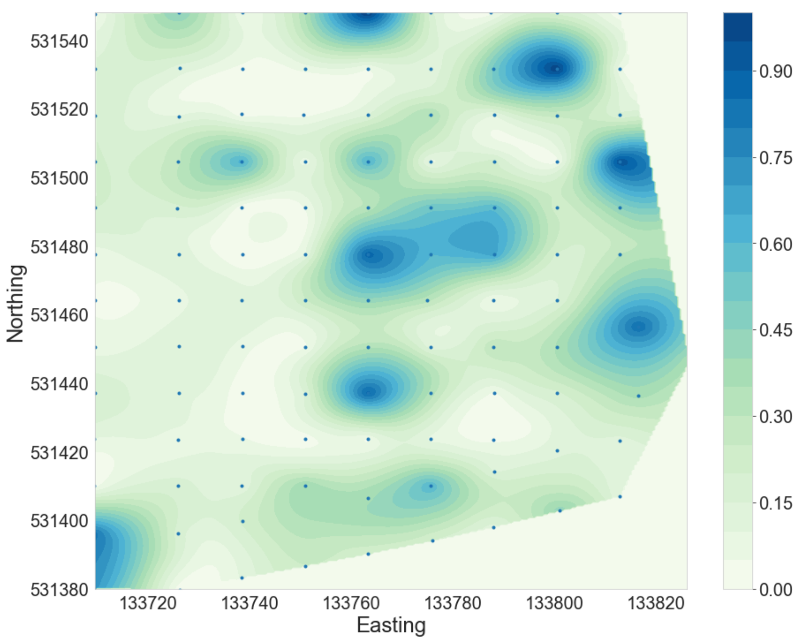

Figure 5.42: Ordinary Kriging interpolation of the carbon extraction data from March 2021 to March 2022. The blue dots represent the locations of the 110 gas wells. Color bar indicates carbon mass extracted in this time period (in tonnes). The greenish background colour does not represent any data, but is instead a quirk of the figure rendered used.

Then in Figure 5.43 both kriging interpolations are shown in 3D space, to show visually the data on which correlations will be computed.

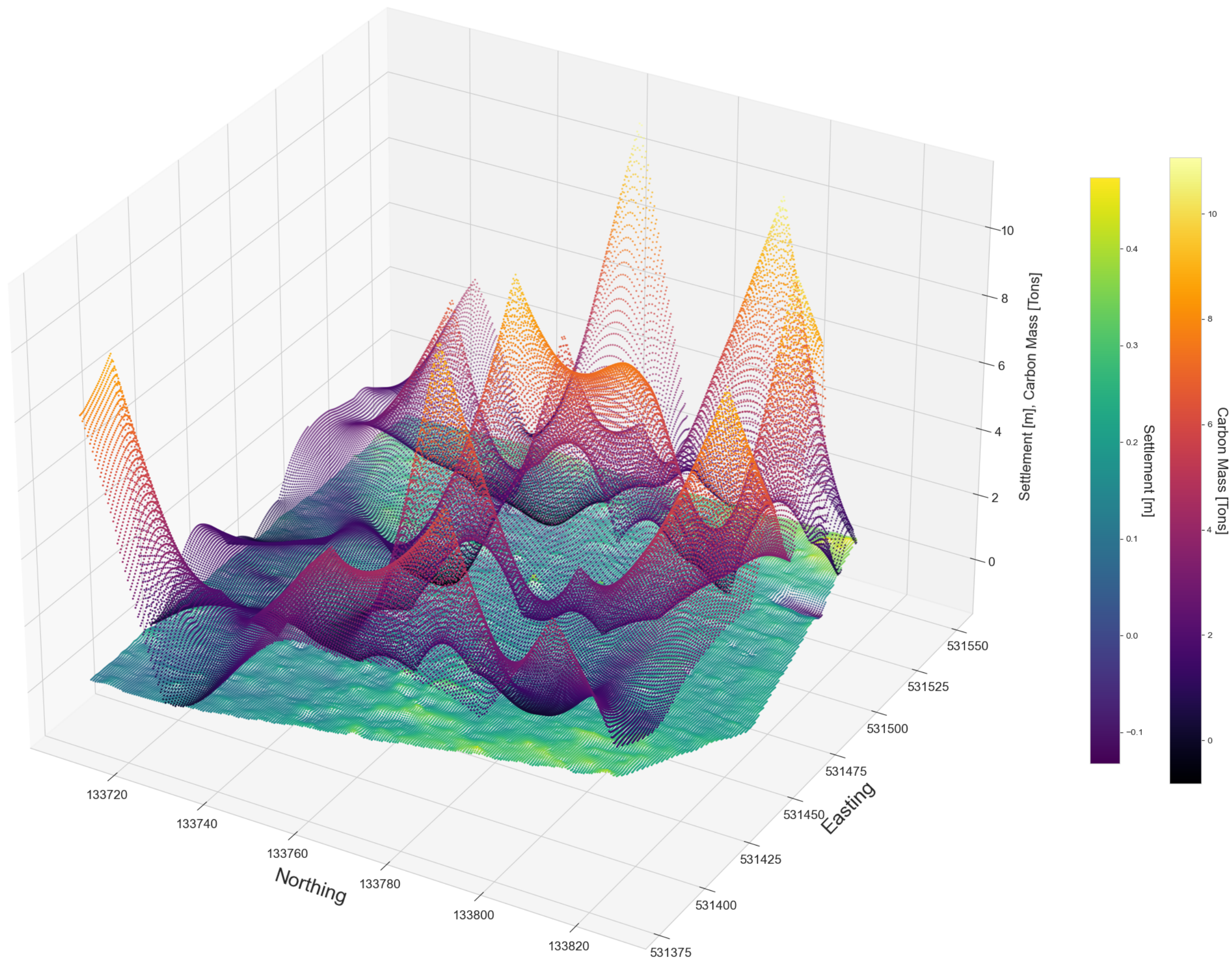

Figure 5.43: Interpolated extracted carbon mass (top surface), and the ALS M3C2 derived settlement (bottom surface) in 3D space. The carbon mass is scaled by a factor of 10 for visual effect. Used for visualisation, not for analysis.

Using the data that was visualised in Figure 5.43, the correlation between the settlement and carbon extraction is computed. This step is repeated for GNSS and TLS data. Table 12 shows the Pearson Correlation Coefficients found using different acquisition methods as input for the settlement. The gas data is made consistent with the time range of the settlement method under review.

Table 12: Pearson Correlation Coefficients for three acquisition methods at different time ranges.

Method	Timescale	Pearson Correlation Coefficient, r
ALS	2021 May – 2022 March	0.031
TLS	2021 May – 2022 March	0.079
TLS	2021 July – 2022 March	0.189
TLS	2021 July – 2021 August	0.215
GNSS	2021 May – 2022 March	0.324
GNSS	2021 Aug – 2022 March	0.503

Turney (2022) states that a correlation coefficient between 0 and 0.3 represents a weak correlation, between 0.3 and 0.5 moderate, and greater than 0.5 strong. From the values in Table 12 we can then state that neither the ALS or TLS data shows a strong correlation to the carbon extraction data. The correlations between the GNSS measurements show significantly stronger correlations, with the data from August 2021 to March 2022 showing the highest correlation from the data available. The correlations between the LiDAR acquisition methods show a distinct difference, the TLS nearly reaches a moderate correlation whilst the ALS correlation is nearly a factor 10 smaller when compared against the highest TLS value.

6 Discussion

This chapter will discuss upon the results of this study. First, Section 6.1 covers the GNSS discrepancy. Second, in Section 6.2 the registration is discussed. Third, in Section 6.3 the comparison of acquisition methods is covered. Fourth, in Section 6.4 the settlement is discussed. Finally, in Section 6.5 the correlation between the settlement and carbon extraction is discussed.

6.1 GNSS discrepancy

The GNSS receivers available to this study were used to provide highly accurate and precise measurements, based on which the LiDAR data can be anchored to the true ground surface. Any deviations, errors or misreported values in the GNSS data propagate forth into the registration of both the TLS and ALS data and as such a great deal of effort was taken to ensure the quality of the GNSS data is high. As shown in Subsection 5.1 a larger than expected deviation in values was observed when using the Trimble GNSS rover. Initially it was thought this was due to incorrect surveying, by for example not allowing the GNSS rover to initialise properly and locate satellites. In the second surveying campaign great care was taken to avoid such mistakes, yet the deviations were still far too large.

The next target of suspicion was the processing applied to the Trimble data. A network of base stations from NETPOS provide post-processing data to improve the accuracy of the RTK GNSS rover. The nearest stations are 24 and 34 kilometers away, decreasing the RTK precision to 40 mm. As this 40 mm deviation can be both positive and negative in the worst case an error of 80 mm can be introduced. The survey on the 9th of June with the Trimble R7, R8 and Stonex S10 provided the answers to the discrepancy, namely a software error and less than desired performance of the Trimble R7 on its own. Whilst the software issue was resolved, the need for the Trimble R7 base station remains if there is a need for the Trimble R7 to be used.

What made analysing this discrepancy harder than it needed to be was the lack of ground control points in both the data collected by Afvalzorg, as well as the Trimble TU Delft measurements. Henceforth, all surveys should include a ground control point as validation and reference.

6.2 Registration

The registration process for the 2021 May and 2022 March ALS and TLS data provided registrations that were of high enough quality for settlement to still be distinguishable. The registration error is in the low centimeter range, whereas the mean settlement over this period as measured by the GNSS rover was nearly a decimeter at certain plates. As such, the registration error should be small enough for it not to obscure the settlement that has occurred. Some plates, such as plate 13 only 2 centimeters of settlement within the period in between the scans. Here settlement nearly entirely falls into the registration error range.

However the 2021 July and August TLS scans, which had no ALS counterpart available contain significant uncertainty. The top of the landfill, devoid of rigid structures, is affected by the gradual misalignment as shown in Figure 5.7. The only way to correct this misalignment is through the use of ground settlement plate GNSS measurements performed in September. But, as these are covered by soil and foliage in the scans it is nigh impossible to utilise this data for a precise centimeter level adjustment. In the M3C2 results of these point clouds (Figure C.5 and C.4) negative settlement (uplift) of 1.13 m was computed, which is far outside the realm of possibility.

It is likely major gains can be made in settlement accuracy by further improving the registration process, both during the survey and afterwards whilst processing the data. By first uncovering the settlement plates, prior to a LiDAR survey, they might be distinguishable in the scan, allowing for corrections using the GNSS measurements at these points. The settlement plates could be used as additional tie points in the registration process. This would then remedy the issue mentioned in the previous paragraph, avoiding the current case of highly uncertain July and August TLS data.

The CSF algorithm has difficulties when filtering out structures close to the ground. Instead of filtering out the structures in some cases the nearby ground points are instead marked as off-ground points, where the cloth resolution determines the extent/area of this error. When the resolution is set too fine to partially negate this issue, the filter instead becomes over-sensitive, incorrectly marking areas significant areas of the landfill as off-ground points. Furthermore, CSF does not remove enough vegetation to markedly improve the performance of ICP. Therefore, CSF does not provide a solution to vegetated areas being unsuitable for the iterative registration algorithm. Instead rigid structures should be used.

6.3 Acquisition methods

When comparing the RIEGL UAV based ALS data and Leica TLS data notable differences were observed. The most immediately noticeable benefit of the UAV obtained ALS data is it scans the area in a continuous and complete manner, as shown in Figure 5.13. The northern part of the landfill is barely captured by the TLS scans, with the northern slope being completely absent from the point clouds. Whilst this can be remedied by adding additional scanning locations it is a time consuming affair, something not always possible or feasible. Scanning the entire landfill using the TLS would become a two day affair, whereas the UAV can scan the landfill in mere hours.

Another benefit is the nearly orthogonal incidence angle the UAV can reach when scanning the landfill, minimizing the shadowing effect the TLS data is plagued by. Due to the shadowing effect there are sections devoid of data in the TLS scans, and it limits the extent of the point cloud. This can be seen in Figure 5.12 where large parts of the smokestack and containers are not present in the TLS point cloud.

Due to the low incidence angle of the TLS, and low elevation as compared to the surface of the landfill, the point density of the TLS point clouds rapidly drop off. As the top of the landfill is very flat this effect is exacerbated, as shown in Figure 5.14. Whilst the increased density close to the scanning location and low incidence angle has its benefits, like having better point coverage below the aeration infrastructure as compared to the ALS data, this does not balance out against the drop off and limited extent of the TLS data.

A notable difference is shown in Figure 5.21, the comparison of a metal pole using unsampled data. Whereas the TLS is able to capture the pole to such a degree it is recognizable by the naked eye, the ALS scan is merely a column of noisy points. This difference is observed in all regions of the landfill, and irrespective of the type of surface scanned (as seen in the histograms in Figure 5.20). However, the effect this has on the computed settlement is thought to be limited. Vegetated areas are naturally noisy and rough in texture,

6.3.1 Elevation obtained from method

From the elevation comparison it was found that both the ALS and TLS point clouds at all times show a higher elevation at the settlement plate locations than that measured by the GNSS rover. This can be attributed to the soil and vegetation covering these plates. Even if the vegetation, or any other object present on the landfill, is perfectly filtered out, due to this soil and plant matter layer there will always be this offset in the elevation. The fact that at no plate the LiDAR data showed a lower elevation than the GNSS measurements is positive, as otherwise there would be a significant error occurring.

In any next ALS or TLS surveys it would be interesting to uncover the settlement plates prior to scanning to investigate if the differences observed in Figure 5.35 would drastically decrease due to the removal of dirt and vegetation. This would confirm the hypothesis that these differences are caused by the dirt/vegetation as shown in Figure A.9.

From Figure 5.23 it can be observed that the GNSS measurement at the settlement plate is representative for the surrounding landfill surface up to great distances. At some plate locations the differences in elevetation remains within 5 cm at distances 20 meters away. The 5 cm difference is exclusive of the consistent offset in elevation between GNSS and LiDAR measurements (due to the aforementioned layer of soil on top of the plates). The discontinuous and limited nature of the GNSS measurements was one of its main weaknesses. But from this figure it is clear that the GNSS measurement at a settlement plate does not only represent the elevation at this exact location, but also the surroundings to varying extent depending on the plate.

6.4 Settlement from LiDAR

The point clouds originating from May, July and August 2021 contain significant amounts of vegetation which obscures the bare ground. Even after the processing steps undertaken it is likely vegetation has a significant contribution to the settlement values found. The settlement found using LiDAR methods is significantly higher than those using the GNSS settlement plate measurements. This coincides with the earlier scan containing taller vegetation, the difference in vegetation between the scans is added to the settlement data. Hence it is critical to filter the vegetation as much as possible, to get closer to the real settlement of the landfill.

In Figure 5.29 the dark red and purple areas in the east and west of the landfill are areas with significant vegetation in the May 2021 point cloud. Interestingly the exact path the mowing tractor took can be seen both at the outer edges of this area, as well as the tire tracks that were left behind by the tractor. The settlement values within the tire tracks are inline with those found near the middle of the landfill, outside of the dark red and purple areas. The difference in settlement between the tire track and the vegetation a mere meter away is upwards of 70 cm. The drastic impact the trampled vegetation within the tire track has on the settlement further reinforces the significance of vegetation.

The effect of vegetation on the settlement was further quantified using Figure 5.32 (cropped in Figure 5.32). Here it can be seen that even the point clouds that were scanned within a week of mowing contributed centimeters of difference between the two LiDAR methods. Near the TLS scanning locations the terrestrial scanner was able to penetrate the vegetation further than the ALS, as there the measured TLS elevation is lower than the ALS elevation. Further away from the TLS scanning locations, where due to the nearly horizontal incidence angle the vegetation penetration is much less, the ALS has lower elevations instead. At nearly flat areas of the landfill this difference in vegetation penetration can account for upwards of 10 - 15 cm in measured elevation.

The ALS and TLS scan of 2022 contain significantly less vegetation and if these were to be compared against a new point cloud containing equally low amounts of vegetation the results will improve drastically. In spring 2023 a new ALS survey is planned which is a perfect opportunity to create an additional point cloud after a fresh mow.

Whether the aeration infrastructure, separated from the landfill surface through the CSF algorithm, could be used to compute the settlement was investigated. Due to the presence of tall vegetation in the off-ground points this turned out ineffective. But, if it were to be repeated using two point clouds both devoid of vegetation it could still prove to be an effective way to mitigate the effect of vegetation obfuscating the settlement of the landfill.

6.5 Settlement correlation to carbon extraction

The overall carbon extraction shows no significant changes over time, even though the flow rates changed significantly over the years from an initial peak of 1000 m^3 per hour to a low of 400 m^3 per hour. There are however large differences between the 110 gas wells, as shown in Figure 5.36.

In Figure 5.38 the settlement at the settlement plates was compared against the carbon extracted during the period at which settlement took place. Interestingly, an almost reverse correlation can be seen. Areas of high settlement in all three acquisition methods corresponded to wells with (relative) low amounts of carbon extracted. But upon closer inspection, as done in Figures 5.39 and 5.40 the settlement does seem to correlate to the carbon extraction. This apparent contradiction should be studied further.

The current implementation of the correlation script crops the LiDAR data to the outer extents of the gas wells, as shown in Figure 4.8. For the outer wells part of their area of influence is now cropped away due to this. There should be an outer border area around the outer wells, instead of being cropped to the exact extent of the gas wells.

7 Conclusions and recommendations

7.1 Conclusions

The availability of a treasure trove of remote sensing, as well as gas extraction, data available for the Wieringermeer landfill allowed for this unique study into the settlement and its correlation to carbon extraction. This chapter concludes the thesis by providing answers to the research, and sub-research questions. In addition some recommendations for future work are given in Section 7.3. First the sub-questions are answered in Subsection 7.1.1.

7.1.1 Sub-questions

1. *What is the impact of factors such as vegetation and method uncertainty on retrieving the settlement quantified using UAV-based LiDAR, Terrestrial Laser Scanning, and GNSS receiver surveys?*

   The GNSS receiver surveys are not impacted by vegetation, par the manual labour of removing it from the ground settlement beacons. It is however impacted by the performance of the device itself (Table 3) and the availability of validation and post-processing data. These two factors caused significant issues quantifying the settlement of the landfill, but have since been resolved. With the introduction of a GNSS base station and ground control points the GNSS rover will provide high quality measurements of the settlement with sub centimeter accuracy.

   The method uncertainty of both LiDAR data sources is of a magnitude that settlement is not obscured by it. Vegetation on the other hand has a significant impact on the ability of both ALS and TLS to quantify the settlement of the landfill. When comparing the 2021 May and 2022 March ALS and TLS scans the settlement is completely obscured by vegetation on most of the western slope (Figure 5.29), and part of compartment 5A. Even when the landfill surface has been freshly mowed some impact remains (10 - 15 cm), more so for the TLS due to its low incidence angle at increasing distance away from the TLS position.

2. *What are the differences between the LiDAR UAV and Terrestrial laser scan measurements, and how do these affect the uncertainty?*

   The LiDAR UAV point clouds covers a much larger area of the landfill than those from the TLS, providing a better representation of the pilot location. As the TLS needs to be manually moved around the landfill some areas were not scanned due to time limitations, decreasing the practicality of the TLS produced scans. The reason the UAV is able to so quickly and continuously scan the area is its ability to fly over the landfill. Naturally, this also largely minimises the shadowing effect which causes sparse or empty areas in the point clouds. Stitching multiple TLS scanning locations together does drastically improve the negative impacts of shadowing, but not to the extent the UAV is capable of.

   TLS point clouds contain significantly less noise, or roughness, as shown in Figure 5.21. However, as this study is focused on vegetated, inherently rough, areas the effect of this may be limited. What does show significant effect is the difference in incidence angle of the signals between the two methods.

The higher incidence angle made possible by the UAV allows the signals to penetrate the vegetation deeper than the shallow incidence angle of the TLS. This can be seen in Figure 5.31 where the ALS scan is consistently below the TLS in terms of measured elevation, as the effect of vegetation is less due to the deeper penetration. This theory is strengthened by the points radially near the TLS scanning locations, where the vegetation penetration is increased and the TLS elevations are closer, or even lower, in value than the ALS elevation.

Both methods are significantly impacted by the the accuracy of georeferencing using GNSS and the registration process, as also noted by Kovanič et al. (2020). Due to this two of the TLS scans were deemed unusable as the registration quality was so poor that the settlement retrieved from these scans were far outside the realm of possibility.

3. *How does the settlement in the Wieringermeer landfill vary spatially and temporally?*

There is clear spatial variability in the found settlements of the landfill. From the GNSS measurements it is observed that the slopes (northern, southern and western) settle significantly more than the top of the landfill. On the slopes from March 2021 to March 2022 plate 5 experienced the highest amount of settlement (16 cm), and plate 27 the lowest (6 cm). On the top of the landfill plate 11 experienced the highest at 9 cm, and plate 13 the lowest at 1 cm.

In Figure 5.4 it can be seen that this difference in settlement between the slopes and top of the landfill is unchanged since 2017. There appears to be a steady amount of settlement occurring, but from Figure 5.5 it is observed that in 2018 and at the end of 2020 the slopes of the landfill had peaks in settlement (peak mean settlement of in 8 cm in 2018, compared to a low of 2 cm in early 2020).

Due to the significant vegetation being present in the LiDAR data it is difficult to ascertain if what we compute using M3C2 is settlement, or a difference in vegetation between scans. What has been observed in both LiDAR data sets was a higher amount of settlement occurring in the southern part of the landfill as compared to the central middle area (∼5 cm of difference). In the ALS data the northern slope, and the northern half of the western slope likewise show higher amounts of settlement. However, here it is again unclear if this is due to vegetation or 'real' settlement. One indication it could be due to vegetation is the clear presence of tire tracks in the north of Figure 5.29, if these are caused by trampled vegetation it would mean the surrounding high settlement is caused by vegetation (difference of ∼ 6 centimeter between the tire tracks and surrounding ground). If the visible tire tracks are instead visible due to them cutting into the top soil layer it would disprove this theory. This is not verifiable from the TLS data as these areas are missing from the point clouds due to the limited extent of the TLS point clouds.

GNSS measurements are not available for the exact dates of the ALS and TLS scans, as such the values can not be precisely compared for the temporal variations. An attempt was made in Figure 5.35 and 5.34, taking the closest GNSS measurements available. The temporal (as it is the difference between two surveys) and spatial variability show similarity between ALS, TLS and GNSS measurements. For all plates there is an offset in settlement between GNSS and LiDAR, less so for ALS than TLS. If this offset disappears or shrinks significantly when two point clouds are used, scanned after a fresh mow, it would confirm it is caused by vegetation and could then potentially be corrected for.

4. *What spatial and temporal correlations exists between the variability of settlement and carbon extraction data?*

   There is little to no temporal variability in the cumulative carbon extraction over all wells. Individual wells do show significant changes over the nearly 5 years of measurements, occasionally even dropping to nearly zero carbon extracted during some measurements. From Figures 5.39 and 5.40 a clear correlation between carbon extraction and settlement can be seen. But when visually inspecting all wells and settlement plates together the results are not so clear-cut and require further investigation.

   The computed Pearson Correlation Coefficients between the GNSS measurements and carbon extraction data show a strong correlation, much stronger than those computed from the ALS and TLS data. As the GNSS is believed to provide the most accurate portrayal of the real settlement of the top of the landfill this is a promising result.

7.2 General conclusion

Answer to the main research question of this study:

- *"To what extent can 3D remote sensing be used to measure the settlement and degradation of organic material in a landfill over time?"*

To conclude, 3D remote sensing methods are able to measure the same spatial and temporal trends that were found using GNSS receiver surveyed ground settlement beacons. However, significant uncertainty is caused by the presence of vegetation. This severely inhibits the ability of the LiDAR methods to accurately measure the settlement.

The GNSS rover is able to precisely measure the settlement of the 28 plates installed on the landfill surface, and is therefore irreplaceable. There is nearly no training required for operating the rover, it can rapidly survey the landfill, and the results are easily processed and interpreted.

When the GNSS measurements are compared against the elevations from both ALS and TLS large, but potentially consistent, offsets are found. It is hypothesised that with point clouds devoid of vegetation these offsets could be corrected for, drastically improving the performance of the LiDAR methods at measuring settlement. This hypothesis could not be tested with the available data, but this will be possible with the planned 2023 ALS scan.

The added value the TLS provides is a scan with comparatively low noise, and very high point density near the scanner. Due to the inherently noisy vegetated area of the landfill the first aspect has very limited benefits. The high point density, and high incidence angle, allows for higher amounts of vegetation penetration than the ALS. However, this is only within very close (<10 meter) proximity to the scanner, severely diminishing the added value this provides. Furthermore, large sections of the landfill were not scanned at all. Whilst this is remedied by additional scanning locations this will require significantly more time surveying.

The ALS is the preferred method of LiDAR acquisition for measuring the settlement of the pilot landfill. It was able to rapidly scan the entirety of the landfill. Its ability to penetrate the vegetation on top of the landfill surface was worse than that of the TLS close to its scanning location. But this quickly reverses as mentioned earlier, moreover the ALS provides a much more consistent penetration and therefore more consistent settlement results.

The correlations computed between the methods and carbon extraction data where mixed. The GNSS measurements showed the highest amount of correlation, then the TLS, and the ALS shows nearly no correlation. Whilst the GNSS result was expected due to its ability to precisely measure the settlement, the TLS was found to be worse than the ALS at measuring settlement but here shows a higher correlation. This places into doubt the validity of the methodology used to compute these correlations.

7.3 Recommendations

The methodology described in Chapter 4 contains a number of processes and steps that could all be further improved upon. However, optimising a specific processing step is not the main focus of the study. Instead, the recommendations are focused on improving the ability of settlement to be measured by the available remote sensing methods. These recommendations are based on encountered weaknesses or deficiencies.

1. *GNSS surveying improvements*

   The current GNSS surveys do not incorporate any ground control points on rigid, non-moving, areas. These should be a standard addition to the current surveys of the ground settlement beacons to provide validation data for these measurements. Near the landfill are some paved roads and parking lots which provide a suitable location for the control points. This issue came to light due to the discrepancy in measurements between the Stonex S10 and Trimble R7.

   If the Trimble R8 GNSS rover is to be used by operators from the TU Delft, the Trimble R7 base station should at all times be brought along and installed. By post processing the Trimble R8 rover's RTK surveys the mean difference between the Stonex and Trimble measurements are reduced by ∼2 cm, with a final difference of only ∼0.5 cm.

2. *Mowing*

   The vegetation growing on the landfill has an adverse impact on the ability to measure the settlement of the landfill using LiDAR acquisition. It should be coordinated between the mowing company and surveyors that the mowing takes place as close as possible to the surveys. This was done for the most recent scan in March 2022, and as a result these scans were impacted to a much lesser extent by the obfuscating effects of vegetation.

   Another ALS survey is planned for 2023, if mowing is correctly coordinated for this survey there will be two 'low-vegetation' surveys available (also from March 2022). Using these two surveys the processing pipeline and comparison from this study should be repeated, this should then provide vastly improved M3C2/LiDAR derived settlement maps.

   Further work should be spent on improving the filtering of vegetation from the point clouds, whilst this will not produce improvements as significant as mowing, any improvements to the significant vegetation uncertainty should be welcomed.

   In a similar fashion to coordinating the mowing, the ground settlement plates should be cleared of vegetation, debris and soil prior to any LiDAR scanning taking place. If the settlement plates are then located within the LiDAR point cloud the difference in elevation measurement between the GNSS and LiDAR methods could be quantified very precisely. Due to the highly reflective metal surface of these plates it might be necessary to cover them with a less reflective material before scanning.

3. *Well data*

   The analysis of the well data was limited in scope in this thesis. Further studies should be done on this component of the thesis, especially once the third and final ALS survey is performed in 2023 at the Wieringermeer landfill, improving the ability to analyse the temporal aspect of the settlement. Furthermore, the amount of carbon extracted can also be calculated through the gas densities and the flow rate at the gas blower station. Based on some preliminary, non final, results the amount of carbon extracted calculated this way are somewhat close in value (2206 tonnes, versus 2583 tonnes using the method used in this study), but more work should be spent on this comparison.

References

Abed, F. M., Mills, J. P., and Miller, P. E. (2012). Echo amplitude normalization of full-waveform airborne laser scanning data based on robust incidence angle estimation. *IEEE Transactions on Geoscience and Remote Sensing*, 50(7):2910–2918.

Agdag, O. and Sponza, D. T. (2004). Effect of aeration on the performance of a simulated landfilling reactor stabilizing municipal solid wastes. *Journal of environmental science and health. Part A, Toxic/hazardous substances & environmental engineering*, 39:2955–72.

AHN (2022). Specifications actueel hoogtebestand nederland. https://www.ahn.nl/kwaliteitsbeschrijving.

Anders, N., Valente, J., Masselink, R., and Keesstra, S. (2019). Comparing filtering techniques for removing vegetation from uav-based photogrammetric point clouds. *Drones*, 3(3).

Bareither, C. A. and Kwak, S. (2015). Assessment of municipal solid waste settlement models based on field-scale data analysis. *Waste Management*, 42:101–117.

Barlaz, M. A., Ham, R. K., Schaefer, D. M., and Isaacson, R. E. (1990). Methane production from municipal refuse: A review of enhancement techniques and microbial dynamics. *Critical Reviews in Environmental Science and Technology*, 19:557–584.

Benson, C., Barlaz, M., Lane, D., and Rawe, J. (2007). Practice review of five bioreactor/recirculation landfills. *Waste Management*, 27(1):13–29.

Bolyard, S. C. and Reinhart, D. R. (2016). Application of landfill treatment approaches for stabilization of municipal solid waste. *Waste Management*, 55:22–30. SI:Sanitary Landfilling.

Brand, E., de Nijs, T., Claessens, J., Dijkstra, J., Comans, R., and Lieste, R. (2014). Development of emission testing values for pilot landfills for sustainable landfill practices - phase 2: Proposals for testing values.

Brede, B., Lau, A., Bartholomeus, H. M., and Kooistra, L. (2017). Comparing riegl ricopter uav lidar derived canopy height and dbh with terrestrial lidar. *Sensors*, 17(10).

Cheremisinoff, N. P. (1997). 4 - groundwater contamination. In Cheremisinoff, N. P., editor, *Groundwater Remediation and Treatment Technologies*, pages 127–168. William Andrew Publishing, Westwood, NJ.

CloudCompare (2015). Distances computation. https://www.cloudcompare.org/doc/wiki/index.php?title=Edit%5CSubsample.

CloudCompare (2016). User manual: version 2.6.1. http://www.cloudcompare.org/doc/qCC/CloudCompare%20v2.6.1%20-%20User%20manual.pdf.

Corrigan, F. (2020). Drone gyro stabilization, imu and flight controllers explained. https://www.dronezon.com/learn-about-drones-quadcopters/three-and-six-axis-gyro-stabilized-drones/.

Edi, T. B. and Ranguette, V. J. (1990). Wuellner, ww," settlement of municipal refuse. *Geotechnics of waste fills: Theory and practice*, 1070:225.

EPA (2021). Understanding global warming potentials. https://www.epa.gov/ghgemissions/understanding-global-warming-potentials.

Fang, W., Huang, X., Zhang, F., and Li, D. (2015). Intensity correction of terrestrial laser scanning data by estimating laser transmission function. *IEEE Transactions on Geoscience and Remote Sensing*, 53(2):942–951.

Gil, A., Núñez-Casillas, L., Isenburg, M., Alonso-Benito, A., Bello, J., and Arbelo, M. (2013). A comparison between lidar and photogrammetry digital terrain models in a forest area on tenerife island. *Canadian journal of remote sensing*, 39:396–409.

Glira, P., Pfeifer, N., Briese, C., and Ressl, C. (2015). A correspondence framework for als strip adjustments based on variants of the icp algorithm. *Photogrammetrie-Fernerkundung-Geoinformation*, 2015(4):275–289.

Hall, D., Gronow, J., and Smith, R. (2004). Achieving equilibrium status and sustainable landfill–the holy grail? *Proceedings of Waste Conference Integrated Waste Management and Pollution Control: Policy and Practice, Research and Solutions*, pages 568–578.

Hartkamp, A., de Beurs, K., Stein, A., and White, J. (1999). Interpolation techniques for climate variables. *Geographic Information Systems Series 99-01. International Maize and Wheat Improvement Center (CIMMYT), Mexico 1999. ISSN: 1405-7484*.

Heimovaara, T., Oonk, H., van der Sloot, H., and van Zomeren, A. (2010). Reduction of the long-term emission potential of existing landfills, final report phase 2. https://duurzaamstorten.nl/wp-content/uploads/2016/07/EindRapportDSII_v06_lay_out.pdf.

Horswell, J. (2013). Recording. In Siegel, J. A., Saukko, P. J., and Houck, M. M., editors, *Encyclopedia of Forensic Sciences (Second Edition)*, pages 368–371. Academic Press, Waltham, second edition edition.

Huber, D. (2011). The astm e57 file format for 3d imaging data exchange. In *Three-Dimensional Imaging, Interaction, and Measurement*, volume 7864, pages 88–96. SPIE.

IEA (2021). Methane tracker 2021. https://www.iea.org/reports/methane-tracker-2021.

Isenburg, M. (2022). lasoverlap. https://rapidlasso.com/lastools/lasoverlap/.

IUPAC (2019). *Compendium of Chemical Terminology, 2nd edition*. Blackwell Scientific Publications, Oxford, England.

Kankare, V. (2015). *The prediction of single- tree biomass, logging recoveries and quality attributes with laser scanning techniques*. PhD thesis.

Kattenberg, W. and Heimovaara, T. (2011). Policy process of allowingresearch pilots for sustainableemission reduction at landfills in the netherlands.

Kattenberg, W., van der Sloot, H., and Heimovaara, T. (2013). New dutch legislation to allow research of natural biodegradation at landfills.

Kovanič, L., Blistan, P., Urban, R., Štroner, M., Blišťanová, M., Bartoš, K., and Pukanská, K. (2020). Analysis of the suitability of high-resolution dem obtained using als and uas (sfm) for the identification of changes and monitoring the development of selected geohazards in the alpine environment—a case study in high tatras, slovakia. *Remote Sensing*, 12(23):3901.

Lague, D., Brodu, N., and Leroux, J. (2013). Accurate 3d comparison of complex topography with terrestrial laser scanner: Application to the rangitikei canyon (n-z). *ISPRS Journal of Photogrammetry and Remote Sensing*, 82:10–26.

Laner, D., Crest, M., Scharff, H., Morris, J., and Barlaz, M. (2011). A review of approaches for the long-term management of municipal solidwaste landfills. *Waste Management*, 32:498–512.

Lee, H. (1973). Accuracy limitations of range-range (spherical) multilateration systems.

Legg, S. (2021). Ipcc, 2021: Climate change 2021-the physical science basis. *Interaction*, 49(4):44–45.

Leica Geosystems (2022). Datasheet leica scanstation p40. https://leica-geosystems.com/products/laser-scanners/scanners/leica-scanstation-p40--p30.

Leonard, Sr, M. L., Floom, Jr, K. J., and Brown, S. (2000). Estimating method and use of landfill settlement. In *Environmental geotechnics*, pages 1–15.

Ling, H. I., Leshchinsky, D., Mohri, Y., and Kawabata, T. (1998). Estimation of municipal solid waste landfill settlement: Journal of geotechnical and geoenvironmental engineering: Vol 124, no 1.

Lwasa, S., Seto, K., Bai, X., Blanco, H., Gurney, K., Kilkiş, S., Lucon, O., Murakami, J., Pan, J., Sharifi, A., and Yamagata, Y. (2022). IPCC, 2022: Climate Change 2022: Mitigation of Climate Change. Contribution of Working Group III to the Sixth Assessment Report of the Intergovernmental Panel on Climate Change: Urban systems and other settlements Supplementary Material.

Meza, N. (2021). Project sustainable landfill management. summary document. *Internal report project CURE (Coupled Multiprocess Research to Reduce Landfill Emissions).*

Oonk, H. (2012). Introductie duurzaam stortbeheer op praktijkschaal - integraal plan van aanpak.

Pfeifer, N., Dorninger, P., Haring, A., and Fan, H. (2007). Investigating terrestrial laser scanning intensity data: quality and functional relations. *8th Conference on Optical 3-D Measurement Techniques*.

Powrie, W., Xu, X.-B., Richards, D., Zhan, L., and Chen, Y. (2019). Mechanisms of settlement in municipal solid waste landfills. *Journal of Zhejiang University - Science A: Applied Physics & Engineering*, 20.

Prokop, A. and Panholzer, H. (2009). Assessing the capability of terrestrial laser scanning for monitoring slow moving landslides. *Natural Hazards and Earth System Sciences*, 9(6):1921–1928.

Rajammal, S. (2009). Effect of dissolved organic carbon (doc) on heavy metal mobility in soils. *Nature Environment and Pollution Technology*, 8:817–821.

Reddy, K. and Bogner, J. (2003). Bioreactor landfill engineering for accelerated stabilization of municipal solid waste. *Proceedings of Invited Theme Paper on Solid Waste Disposal, International E-Conference on Modern Trends in Foundation Engineering: Geotechnical Challenges and Solutions*, page 22.

RIEGL (2016). Datasheet riegl vux-sys. https://www.rieglusa.com/pdf/vux-sys-datasheet.pdf.

Rijksoverheid (2021). Klimaatnota 2021. *Ministerie van Buitenlandse Zaken en Klimaat*.

Ritzkowski, M. and Stegmann, R. (2012). Landfill aeration worldwide: Concepts, indications and findings. *Waste Management*, 32(7):1411–1419.

Ritzkowski, M. and Stegmann, R. (2013). Landfill aeration within the scope of post-closure care and its completion. *Waste Management*, 33(10):2074–2082. Landfill Processes.

Ruyssenaars, P., Coenen, P., Rienstra, J., Zijlema, P., Arets, E., Baas, K., Dröge, R., Geilenkirchen, G., 't Hoen, M., Honig, E., van Huet, B., van Huis, E., koch, W., Lagerwerf, L., te Molder, R., Montfoort, J., Vonk, J., and van Zanten, M. (2020). Greenhouse gas emissions in the netherlands 1990-2018: National inventory report 2020.

Sang, N. N., Soda, S., Sei, K., and Ike, M. (2008). Effect of aeration on stabilization of organic solid waste and microbial population dynamics in lab-scale landfill bioreactors. *Journal of Bioscience and Bioengineering*, 106(5):425–432.

Scharff, H. (2014). Landfill reduction experience in the netherlands. *Waste Management*, 34(11):2218–2224.

Schrott, L., Otto, J.-C., Götz, J., and Geilhausen, M. (2013). 14.2 fundamental classic and modern field techniques in geomorphology: An overview. In Shroder, J. F., editor, *Treatise on Geomorphology*, pages 6–21. Academic Press, San Diego.

Silpa, K., Yao, L., Bhada-Tata, P., and Van Woerden, F. (2018). What a waste 2.0 : A global snapshot of solid waste management to 2050. *Urban Development*.

Soudarissanane, S., Lindenbergh, R., Menenti, M., and Teunissen, P. (2011). Scanning geometry: Influencing factor on the quality of terrestrial laser scanning points. *ISPRS Journal of Photogrammetry and Remote Sensing*, 66(4):389–399.

Stonex (2021). Datasheet stonex S10N gnss system. https://www.stonex.it/project/s10-gnss-receiver.

Tallysman (2022). Gnss positioning techniques. https://www.tallysman.com/gnss-positioning-techniques/.

Tan, K. and Cheng, X. (2016). Correction of incidence angle and distance effects on tls intensity data based on reference targets. *Remote Sensing*, 8(3).

The EU Space Programme (2021). What is gnss? https://www.euspa.europa.eu/european-space/eu-space-programme/what-gnss.

The Sustainable Landfill Foundation (2022). Natural biodegradation research programme on dutch landfills. https://duurzaamstorten.nl/en/#duurzaamstorten.

Trimble (2020). Datasheet trimble R8 gnss system. https://geospatial.trimble.com/sites/geospatial.trimble.com/files/2020-10/Datasheet%20-%20Trimble%20R8s%20GNSS%20-%20English%20US%20-%20Screen.pdf.

Turney, S. (2022). Pearson Correlation Coefficient (r) | Guide & Examples. https://www.scribbr.com/statistics/pearson-correlation-coefficient/.

van Meeteren, M., Timens, D., and Uwe Heyer, K. (2009a). Feasibility study sustainable emission reduction at the existing landfills kragge and wieringermeer in the netherlands, specific report: Current status of landfill wieringermeer.

van Meeteren, M., van Vossen, W., and Heyer, K. (2009b). Feasibility study sustainable emission reduction at he existing landfills in the netherlands, specific report: Preliminary design and cost-estimate of the technical measures infiltration and aeration to enhance stabilization at the landfill wieringermeer.

van Turnhout, A. G., Oonk, H., Scharff, H., and Heimovaara, T. J. (2020). Optimizing landfill aeration strategy with a 3-d multiphase model. *Waste Management*, 102:499–509.

Vereniging Afvalbedrijven (2014). Deelplan van aanpak verduurzamingspilot op stortplaats wieringermeer.

Vereniging Afvalbedrijven (2015). Project plan sustainable landfill management braambergen.

Vincent, S. G. T., Jennerjahn, T., and Ramasamy, K. (2021). Chapter 3 - environmental variables and factors regulating microbial structure and functions. In Vincent, S. G. T., Jennerjahn, T., and Ramasamy, K., editors, *Microbial Communities in Coastal Sediments*, pages 79–117. Elsevier.

Vosselman, G. and Maas, H., editors (2010). *Airborne and terrestrial laser scanning*. CRC Press, United Kingdom.

Webredactie CITG (2020). Emissies van afvalstortlocaties beter begrijpen. https://www.tudelft.nl/2020/citg/emissies-van-afvalstortlocaties-beter-begrijpen.

Williams, B., Halloin, C., Löbel, W., Finklea, F., Lipke, E., Zweigerdt, R., and Cremaschi, S. (2020). Data-driven model development for cardiomyocyte production experimental failure prediction. In Pierucci, S., Manenti, F., Bozzano, G. L., and Manca, D., editors, *30th European Symposium on Computer Aided Process Engineering*, volume 48 of *Computer Aided Chemical Engineering*, pages 1639–1644. Elsevier.

Winkless, L. (2016). Why do we need more positioning satellites? https://360.here.com/2016/07/13/why-do-we-need-more-positioning-satellites/.

Zhang, W., Qi, J., Wan, P., Wang, H., Xie, D., Wang, X., and Yan, G. (2016). An easy-to-use airborne lidar data filtering method based on cloth simulation. *Remote sensing*, 8(6):501.

Šašak, J., Gallay, M., Kaňuk, J., Hofierka, J., and Minár, J. (2019). Combined use of terrestrial laser scanning and uav photogrammetry in mapping alpine terrain. *Remote Sensing*, 11(18).

A Photographs

Figure A.1: Leica GZT21 HDS Black and White scanning target for registering the individual TLS scanning locations.

Figure A.2: Controllers for the RIEGL RiCOPTER UAV.

Figure A.3: Riegl RiCOPTER UAV used for aerial laser scanning.

Figure A.4: Trimble R7 GNSS base installed on a nearby parking area.

Figure A.5: Smokestacks used for the registration process.

Figure A.6: Structural elements of the building on the right side of the photograph used for the registration process.

Figure A.7: Smokestack on the left, and containers in center of the photograph used for the registration process.

Figure A.8: Scaffolding and aeration infrastructure used for the registration of same-day ALS and TLS scans.

Figure A.9: Example of ground settlement beacon obscured by soil, vegetation and other objects. Beacon is in the bottom left of the photograph, as marked on the green tube.

B Tables

Table 13: GNSS measurements performed by Afvalzorg of the 28 settlement plates installed on the Wieringermeer landfill. * Frozen soil during measurement, instead measured on 10-04-2018. ** No measurement.

Settlement measurement plates IDS, heights relative to NAP														
Wieringermeer														
Plate	Coordinates		**26/07/2017**	**27-02.2018**	**12/10/2018**	**22/02/2019**	**28/08/2019**	**05/03/2020**	**19/09/2020**	**31/03/2021**	**08/09/2021**	**17/03/2022**	**09/06/2022**	**Settlement**
Nr:	x	y	z	z	z	z	z	z	z	z	z	z	z	z
1	133710.12	531548.076	6.88	6.77	6.58	6.55	6.49	6.43	6.36	6.28	6.21	6.12	6.07	0.82
2	133763.993	531547.454	7.60	7.53*	7.52	7.50	7.47	7.46	7.45	7.43	7.40	7.34	7.32	0.28
3	133812.343	531547.701	8.63	8.52	8.37	8.35	8.30	8.22	8.12	8.04	7.97	7.89	7.87	0.76
4	133850.986	531547.596	10.76	10.73	10.74	10.71	10.70	10.69	10.69	10.71	10.69	10.69	10.68	0.08
5	133709.935	531518.423	7.45	7.38	7.28	7.27	7.19	7.15	7.04	6.90	6.84	6.74	6.70	0.75
6	133744.967	531517.885	11.28	11.22	11.20	11.19	11.16	11.19	11.16	11.17	11.16	11.14	11.13	0.15
7	133776.579	531517.817	11.22	11.18	11.16	11.14	11.14	11.13	11.12	11.15	11.13	11.11	11.11	0.11
8	133807.124	531517.64	10.70	10.65	10.57	10.55	10.55	10.54	10.53	10.54	10.52	10.50	10.50	0.20
9	133851.124	531516.948	10.69	10.64	10.66	10.62	10.62	10.62	10.60	10.62	10.59	10.59	10.59	0.10
10	133710.373	531491.64	7.30	6.98	6.70	6.65	6.54	6.48	6.39	6.31	6.23	6.18	6.15	1.16
11	133744.738	531490.72	10.64	10.62	10.55	10.55	10.51	10.51	10.48	10.47	10.44	10.38	10.35	0.29
12	133776.482	531491.294	10.76	10.68*	10.54	10.50	10.48	10.45	10.44	10.45	10.44	10.43	10.43	0.34
13	133806.459	531491.363	10.56	10.51	10.49	10.48	10.49	10.49	10.47	10.48	10.46	10.46	10.44	0.13
14	133851.048	531490.824	10.72	10.66	10.69	10.64	10.64	10.65	10.63	10.66	10.64	10.64	10.63	0.10
15	133710.44	531464.5	7.45	7.24	7.02	6.94	6.82	6.73	6.53	6.40	6.35	6.27	6.24	1.20
16	133744.816	531464.45	10.37	10.29	10.16	10.23	10.21	10.18	10.16	10.16	10.14	10.09	10.08	0.29
17	133775.795	531464.219	10.42	10.36	10.32	10.27	10.25	10.25	10.23	10.23	10.21	10.21	10.20	0.22
18	133806.797	531464.437	10.21	10.17	10.27	10.11	10.11	10.12	10.09	10.11	10.10	10.07	10.07	0.14
19	133850.901	531464.026	10.37	10.32	10.33	10.27	10.25	10.25	10.24	10.23	10.24	10.22	10.20	0.17
20	133710.108	531437.394	7.19	7.09	6.97	6.90	6.80	6.73	6.58	6.48	6.41	6.32	6.28	0.91
21	133745.073	531437.407	10.00	9.93	9.94	9.89	9.86	9.89	9.87	9.88	9.85	9.81	9.82	0.19
22	133776.99	531437.293	10.13	10.07	10.04	10.00	9.97	9.96	9.94	9.95	9.95	9.92	9.90	0.22
23	133807.214	531436.879	10.03	9.98	9.99	9.94	9.93	9.93	9.91	9.90	9.88	9.86	9.82	0.22
24	133710.277	531410.574	6.81	6.72	6.63	6.58	**	6.48	6.43	6.34	6.33	6.25	6.19	0.62
25	133744.866	531409.693	9.88	9.80	9.79	9.75	9.72	9.71	9.72	9.71	9.72	9.66	9.65	0.23
26	133776.169	531410.166	9.52	9.46	9.44	9.36	9.31	9.27	9.20	9.14	9.09	9.04	8.98	0.53
27	133709.985	531379.832	6.90	6.85	6.84	6.79	6.74	6.74	6.71	6.67	6.65	6.61	6.56	0.35
28	133750.55	531387.313	7.01	6.94	6.85	6.78	6.71	6.66	6.57	6.51	6.49	6.44	6.39	0.62

Table 14: GNSS measurements performed by Afvalzorg of the 110 gas wells installed on the Wieringermeer landfill, height measurement from 14/01/2021.

Well number	X-coordinate	Y-coordinate	Z-coordinate
1	133709.493	531547.781	6.511
2	133725.807	531548.438	6.644
3	133738.186	531548.476	6.777
4	133750.804	531548.267	7.261
5	133763.459	531548.264	7.482
6	133775.823	531548.094	7.695
7	133787.561	531548.318	7.838
8	133800.506	531548.287	7.868
9	133812.853	531548.226	8.231
11	133709.424	531531.908	7.166
12	133726.066	531531.911	11.116
13	133738.403	531531.897	11.107
14	133750.723	531531.766	10.906
15	133763.148	531531.679	10.988
16	133775.640	531531.715	11.162
17	133787.853	531531.720	11.147
18	133800.464	531531.750	11.149
19	133812.919	531531.699	11.020
21	133709.486	531517.929	7.164
22	133725.791	531517.811	10.918
23	133738.391	531518.433	11.142
24	133750.658	531518.252	11.196
25	133763.277	531518.056	11.324
26	133775.600	531518.042	11.489
27	133788.128	531518.122	11.387
28	133800.007	531517.974	11.195
29	133812.860	531518.063	10.530
31	133709.291	531504.534	6.611
32	133725.747	531504.562	10.483
33	133738.222	531504.692	10.812
34	133750.879	531504.538	10.708
35	133763.197	531504.611	10.844
36	133775.436	531504.506	10.782
37	133788.065	531504.456	10.817
38	133800.405	531504.677	10.754
39	133812.858	531504.561	10.926
41	133709.443	531491.094	6.452
42	133725.481	531491.115	10.369
43	133738.391	531491.179	10.541
44	133750.953	531490.996	10.691
45	133763.235	531491.052	10.683
46	133775.568	531491.185	10.647
47	133787.988	531491.330	10.762
48	133800.438	531491.140	10.586
49	133812.776	531491.127	10.699
51	133709.370	531477.552	6.820
52	133725.850	531477.612	10.457
53	133738.447	531477.581	10.627
54	133751.007	531477.553	10.545
55	133763.364	531477.657	10.653
56	133775.743	531477.608	10.545
57	133788.236	531477.592	10.595
58	133800.475	531477.577	10.384
59	133812.841	531477.679	10.497
61	133709.282	531464.139	6.445
62	133725.830	531464.027	10.302
63	133738.488	531464.157	10.447
64	133750.833	531464.069	10.421
65	133763.378	531464.187	10.397

66	133774.923	531464.055	10.404
67	133788.221	531463.598	10.488
68	133800.236	531464.106	10.422
69	133812.844	531464.065	10.303
71	133709.324	531450.497	6.714
72	133726.052	531450.642	9.969
73	133738.496	531450.651	10.310
74	133750.825	531450.559	10.223
75	133763.301	531450.703	10.110
76	133775.556	531450.687	10.351
77	133788.074	531450.689	10.304
78	133800.320	531450.648	10.232
81	133709.037	531436.983	6.525
82	133725.976	531437.217	10.007
83	133738.485	531437.110	10.158
84	133750.861	531437.145	10.014
85	133763.333	531437.003	9.904
86	133775.643	531437.088	10.109
87	133787.816	531436.995	10.227
88	133800.333	531437.086	10.042
91	133709.294	531423.716	6.476
92	133725.762	531423.457	9.912
93	133738.397	531423.281	10.040
94	133750.895	531423.682	9.911
95	133763.361	531423.731	9.754
96	133775.644	531423.623	9.996
97	133787.998	531423.482	9.894
98	133800.452	531420.370	9.784
99	133812.857	531423.023	9.876
101	133709.258	531410.121	6.460
102	133725.959	531410.114	9.883
103	133738.638	531409.967	9.933
104	133750.813	531410.197	9.738
105	133763.385	531406.418	9.501
106	133775.536	531410.023	9.382
107	133787.932	531414.095	9.592
108	133801.056	531402.693	6.543
109	133812.801	531406.894	6.812
111	133709.402	531396.140	6.825
112	133725.886	531396.136	9.712
113	133738.421	531399.763	9.975
114	133751.013	531386.546	6.593
115	133763.242	531390.095	6.711
116	133776.112	531393.996	6.620
117	133788.158	531397.900	6.490
121	133709.389	531380.096	6.852
122	133726.217	531379.546	6.837
123	133738.522	531383.251	6.757
P1	Not measured		
P2	133816.546	531456.184	10.307
P3	Not measured		
P4	Not measured		
P5	Not measured		
P6	133826.544	531446.146	10.116
P7	Not measured		
P8	133816.425	531436.073	10.084
P9	Not measured		

Table 15: ALS M3C2 results from different radii to quantify variability in landfill height around the settlement plates, from Section 5.3.1.

ALS	x	y	GNSS Elevation	M3C2 Radii ->	0.25 m	0.5 m	1 m	2 m	3.5 m	5 m	7.5 m	10 m	15 m	20 m
1	133710.1	531548.1	6.1213	**Plate 1**	0.084	0.094	0.1	0.1	0.08	0.061	0.022	-0.032	-0.16	-0.3
2	133764	531547.5	7.3394	**Plate 2**	0.11	0.12	0.13	0.13	0.13	0.13	0.13	0.12	0.11	-0.095
3	133812.3	531547.7	7.8942	**Plate 3**	0.082	0.11	0.12	0.12	0.11	0.095	0.07	0.058	0.059	0.084
4	133851	531547.6	10.69	**Plate 4**	0.056	0.076	0.095	0.11	0.12	0.12	0.086	0.056	0.023	0.0035
5	133709.9	531518.4	6.7403	**Plate 5**	0.07	0.079	0.091	0.091	0.1	0.11	0.12	0.12	0.13	0.13
6	133745	531517.9	11.1444	**Plate 6**	0.049	0.071	0.082	0.068	0.056	0.047	0.026	-0.001	-0.056	-0.12
7	133776.6	531517.8	11.1145	**Plate 7**	0.088	0.09	0.11	0.11	0.11	0.11	0.088	0.071	0.044	0.011
8	133807.1	531517.6	10.5049	**Plate 8**	0.074	0.085	0.086	0.086	0.091	0.11	0.14	0.17	0.25	0.3
9	133851.1	531516.9	10.5906	**Plate 9**	0.054	0.071	0.083	0.09	0.088	0.084	0.073	0.068	0.053	0.042
10	133710.4	531491.6	6.175	**Plate 10**	0.083	0.081	0.088	0.089	0.092	0.1	0.13	0.16	0.24	0.32
11	133744.7	531490.7	10.3814	**Plate 11**	0.029	0.033	0.054	0.066	0.06	0.055	0.054	0.055	0.051	0.047
12	133776.5	531491.3	10.4342	**Plate 12**	0.096	0.091	0.088	0.088	0.083	0.079	0.065	0.061	0.077	0.11
13	133806.5	531491.4	10.4626	**Plate 13**	0.031	0.062	0.072	0.075	0.078	0.082	0.081	0.079	0.068	0.064
14	133851	531490.8	10.6383	**Plate 14**	0.04	0.053	0.07	0.0883	0.084	0.083	0.074	0.064	0.047	0.031
15	133710.4	531464.5	6.271	**Plate 15**	0.07	0.068	0.095	0.096	0.1	0.11	0.11	0.12	0.14	0.19
16	133744.8	531464.5	10.0918	**Plate 16**	0.046	0.05	0.061	0.071	0.077	0.08	0.089	0.1	0.12	0.13
17	133775.8	531464.2	10.2095	**Plate 17**	0.05	0.082	0.096	0.12	0.1	0.098	0.097	0.1	0.11	0.11
18	133806.8	531464.4	10.0706	**Plate 18**	0.11	0.19	0.2	0.17	0.15	0.14	0.13	0.13	0.14	0.15
19	133850.9	531464	10.2247	**Plate 19**	0.064	0.08	0.089	0.092	0.092	0.094	0.096	0.1	0.094	0.09
20	133710.1	531437.4	6.3224	**Plate 20**	0.14	0.12	0.14	0.14	0.15	0.15	0.14	0.11	0.07	0.05
21	133745.1	531437.4	9.8138	**Plate 21**	0.063	0.08	0.084	0.08	0.078	0.078	0.074	0.072	0.079	0.091
22	133777	531437.3	9.9179	**Plate 22**	0.066	0.088	0.11	0.11	0.12	0.11	0.086	0.066	0.041	0.033
23	133807.2	531436.9	9.8563	**Plate 23**	0.045	0.057	0.075	0.079	0.079	0.072	0.056	0.048	0.044	0.04
24	133710.3	531410.6	6.2508	**Plate 24**	0.1	0.1	0.1	0.1	0.11	0.11	0.11	0.12	0.14	0.17
25	133744.9	531409.7	9.6565	**Plate 25**	0.055	0.075	0.081	0.08	0.064	0.061	0.041	0.027	0.017	0.017
26	133776.2	531410.2	9.0423	**Plate 26**	0.07	0.072	0.081	0.084	0.085	0.08	0.056	0.023	-0.055	-0.14
27	133710	531379.8	6.6137	**Plate 27**	0.038	0.051	0.063	0.058	0.057	0.054	0.032	0	-0.09	-0.21
28	133750.6	531387.3	6.4413	**Plate 28**	0.049	0.056	0.064	0.063	0.058	0.052	0.049	0.051	0.061	0.073

Table 16: TLS M3C2 results from different radii to quantify variability in landfill height around the settlement plates, from Section 5.3.1.

TLS	x	y	GNSS Elevation	M3C2 Radii ->	0.25 m	0.5 m	1 m	2 m	3.5 m	5 m	7.5 m	10 m	15 m	20 m
1	133710.1	531548.1	6.1213	**Plate 1**										
2	133764	531547.5	7.3394	**Plate 2**										
3	133812.3	531547.7	7.8942	**Plate 3**										
4	133851	531547.6	10.69	**Plate 4**					0.3208	0.3168	0.2979	0.4445	0.3149	0.2845
5	133709.9	531518.4	6.7403	**Plate 5**	0.236	0.231	0.228	0.193	0.1990	0.1705	0.1843	0.1738	0.2387	0.3980
6	133745	531517.9	11.1444	**Plate 6**	0.172	0.19	0.195	0.192	0.1860	0.1639	0.1434	0.1188	0.0274	-0.0593
7	133776.6	531517.8	11.1145	**Plate 7**	0.213	0.205	0.212	0.224	0.1993	0.1846	0.1651	0.1595	0.1306	0.0889
8	133807.1	531517.6	10.5049	**Plate 8**			0.257	0.307	0.2915	0.2642	0.2989	0.3276	0.4280	0.4641
9	133851.1	531516.9	10.5906	**Plate 9**		0.22	0.213	0.205	0.2077	0.1926	0.1662	0.1515	0.1345	0.1233
10	133710.4	531491.6	6.175	**Plate 10**			0.264	0.166	0.2305	0.1974	0.1382	0.1692	0.2329	0.3106
11	133744.7	531490.7	10.3814	**Plate 11**		0.128	0.129	0.142	0.1309	0.1246	0.1276	0.1278	0.1238	0.1165
12	133776.5	531491.3	10.4342	**Plate 12**	0.165	0.165	0.166	0.163	0.1506	0.1456	0.1309	0.1247	0.1380	0.1633
13	133806.5	531491.4	10.4626	**Plate 13**	0.155	0.151	0.150	0.140	0.1450	0.1474	0.1454	0.1405	0.1259	0.1203
14	133851	531490.8	10.6383	**Plate 14**		0.163	0.172	0.175	0.1779	0.1781	0.1690	0.1563	0.1401	0.1268
15	133710.4	531464.5	6.271	**Plate 15**	0.0751	0.0846	0.096	0.105	0.1180	0.1313	0.1302	0.1324	0.1639	0.2158
16	133744.8	531464.5	10.0918	**Plate 16**	0.0576	0.0757	0.084	0.095	0.1016	0.1049	0.1139	0.1239	0.1473	0.1554
17	133775.8	531464.2	10.2095	**Plate 17**	0.107	0.116	0.124	0.148	0.1325	0.1248	0.1226	0.1283	0.1371	0.1398
18	133806.8	531464.4	10.0706	**Plate 18**	0.122	0.133	0.136	0.147	0.1493	0.1484	0.1503	0.1552	0.1673	0.1763
19	133850.9	531464	10.2247	**Plate 19**		0.198	0.195	0.192	0.1864	0.1878	0.1916	0.1886	0.1772	0.1755
20	133710.1	531437.4	6.3224	**Plate 20**	0.145	0.147	0.164	0.169	0.1865	0.1889	0.1756	0.1493	0.1004	0.0762
21	133745.1	531437.4	9.8138	**Plate 21**	0.0697	0.0801	0.097	0.094	0.0934	0.0945	0.0885	0.0862	0.0930	0.1065
22	133777	531437.3	9.9179	**Plate 22**	0.125	0.124	0.132	0.132	0.1320	0.1244	0.1025	0.0822	0.0622	0.0552
23	133807.2	531436.9	9.8563	**Plate 23**	0.0477	0.066	0.078	0.086	0.0875	0.0807	0.0646	0.0583	0.0569	0.0562
24	133710.3	531410.6	6.2508	**Plate 24**	0.0853	0.0974	0.095	0.102	0.1101	0.1135	0.1153	0.1142	0.1393	0.1707
25	133744.9	531409.7	9.6565	**Plate 25**	0.0808	0.0916	0.091	0.082	0.0729	0.0645	0.0449	0.0311	0.0200	0.0223
26	133776.2	531410.2	9.0423	**Plate 26**	0.0584	0.0768	0.088	0.093	0.0947	0.0878	0.0687	0.0355	-0.0374	-0.1156
27	133710	531379.8	6.6137	**Plate 27**		0.101	0.106	0.096	0.0768	0.0507	-0.0043	-0.0214	-0.0673	-0.1202
28	133750.6	531387.3	6.4413	**Plate 28**	0.0952	0.116	0.155	0.143	0.0654	0.0412	0.0306	0.0375	0.0617	0.0812

C Figures

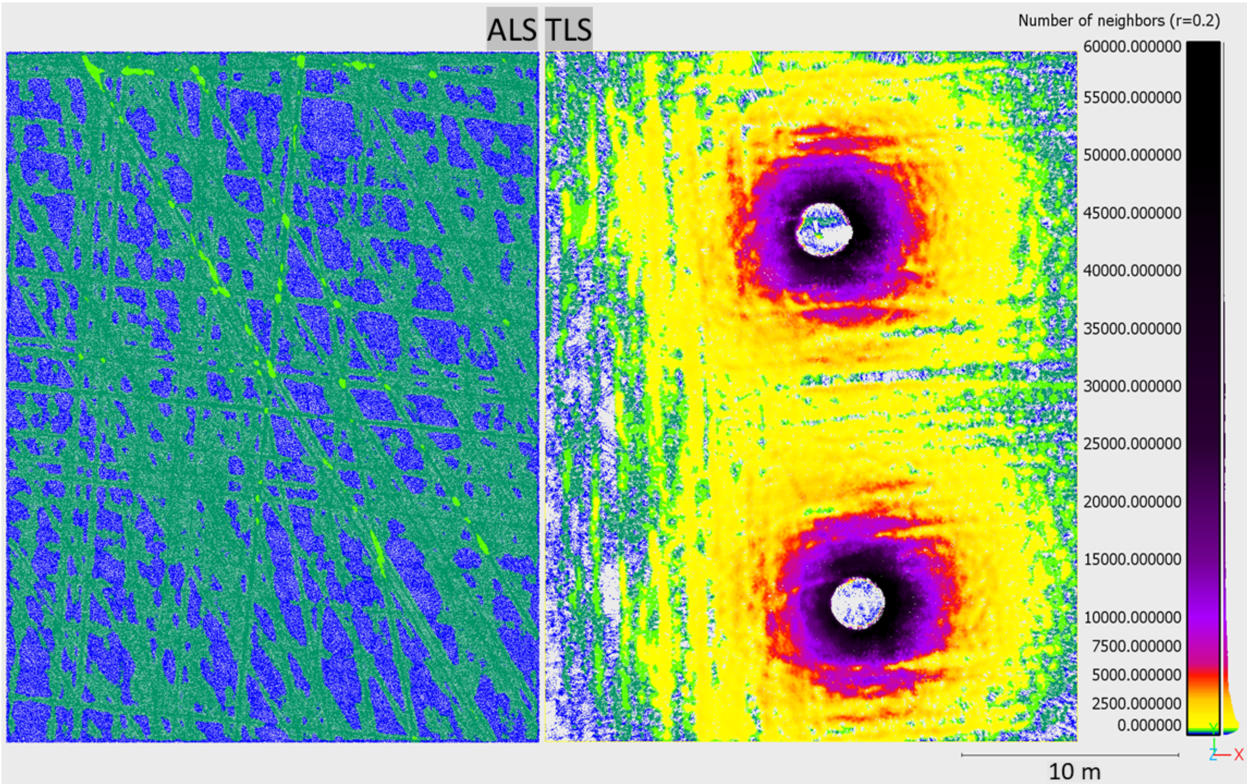

Figure C.1: Alternative to Figure 5.16. Cropped region of Figure 5.14 with adjusted color bar to capture full extent of density.

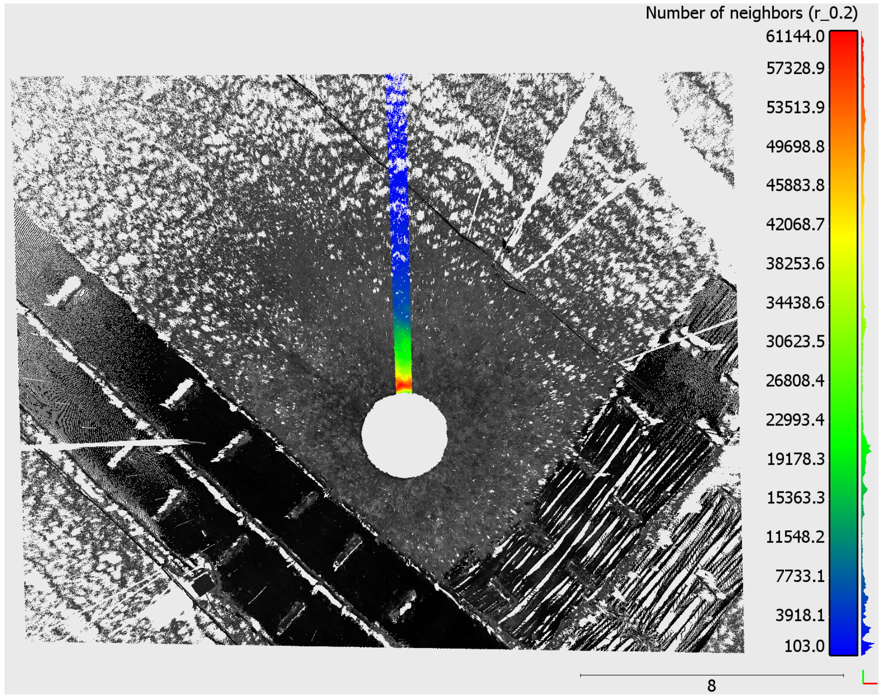

Figure C.2: Cloudcompare version of Figure 5.17. Scale of point cloud in meters.

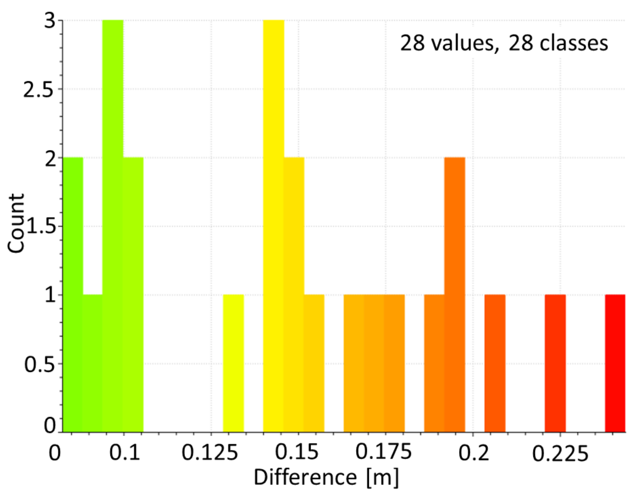

(a) TLS

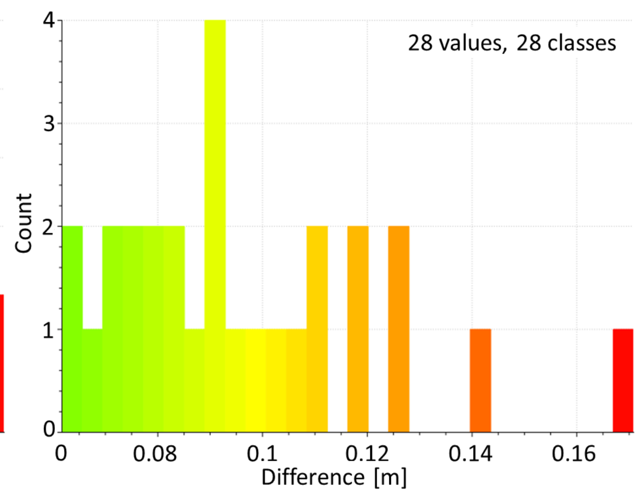

(b) ALS

Figure C.3: Histogram of differences in elevation computed between GNSS and a) TLS b) ALS measurements of the settlement plates.

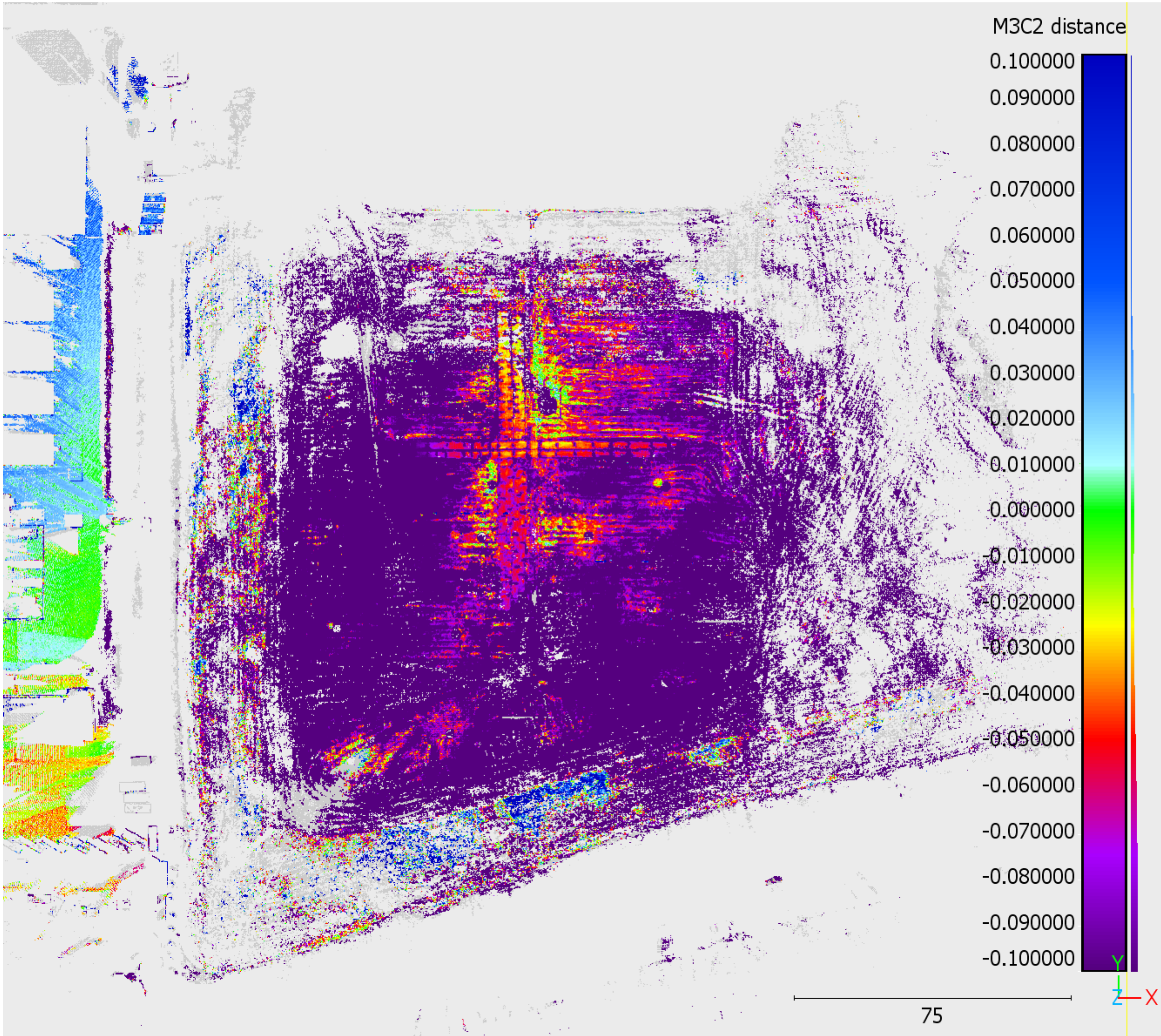

Figure C.4: M3C2 derived settlement between the TLS point clouds of July 2021 and March 2022. Scale of both color bar and point cloud in meters.

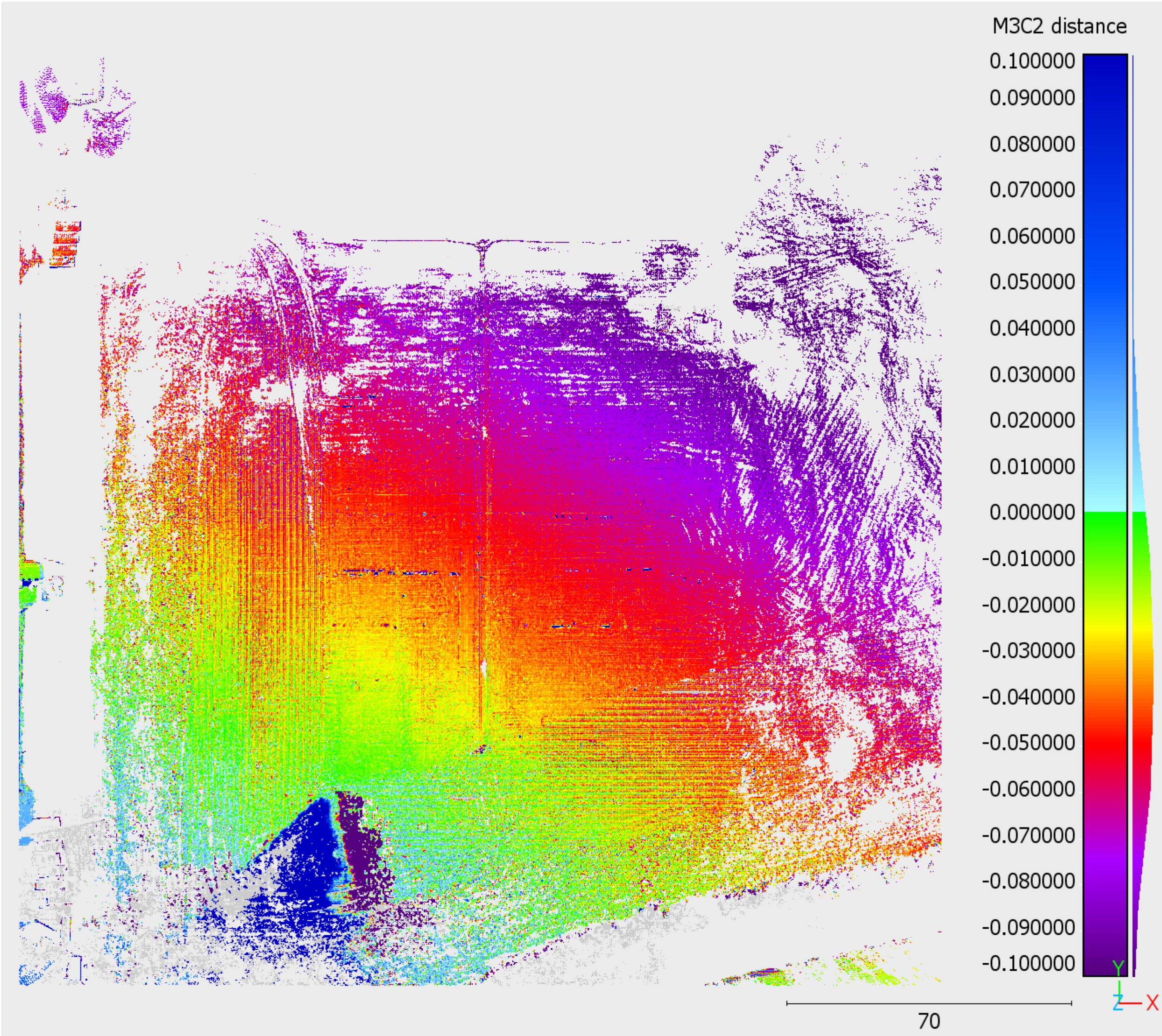

Figure C.5: M3C2 derived settlement between the TLS point clouds of August 2021 and March 2022. Scale of both color bar and point cloud in meters.

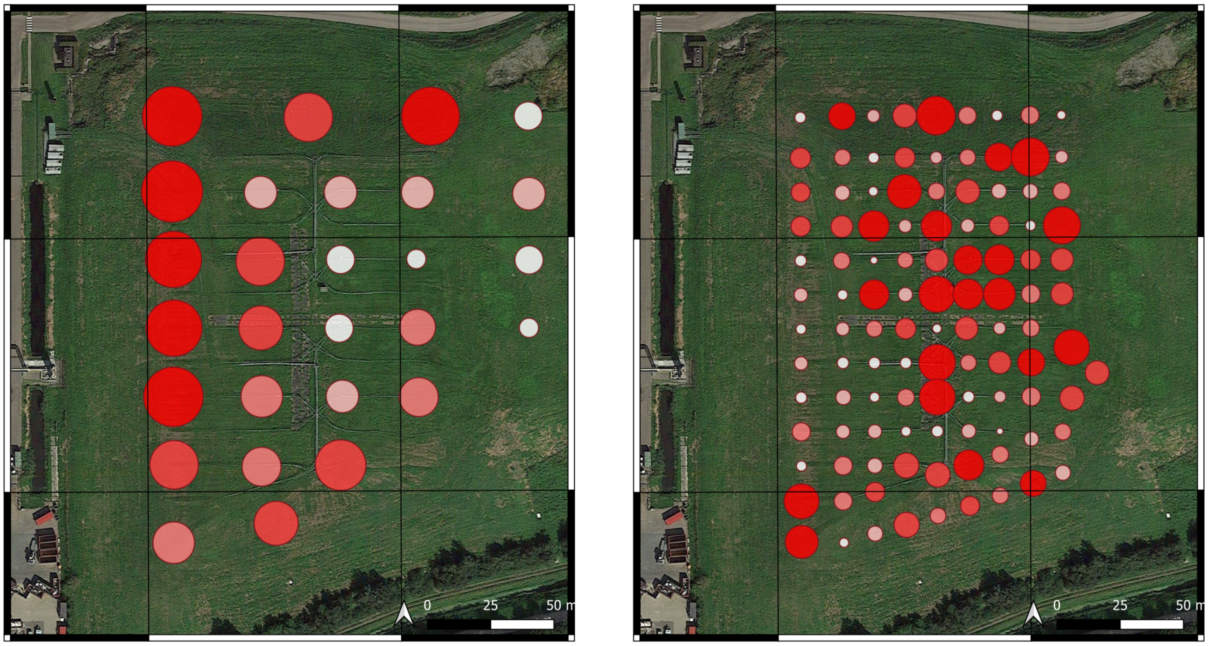

(a) GNSS

(b) Extracted carbon

Figure C.6: Figure C.6a shows the settlement of the plates between March 2021 and March 2022 (from Figure 5.35a). In Figure C.6b Extracted carbon mass between March 2021 and March 2022 in tonnes (from Figure 5.37). Both figures show the same data, on the left annotated and on the right circle size is scaled to the carbon mass value. Same figures as those found in Figure 5.38.

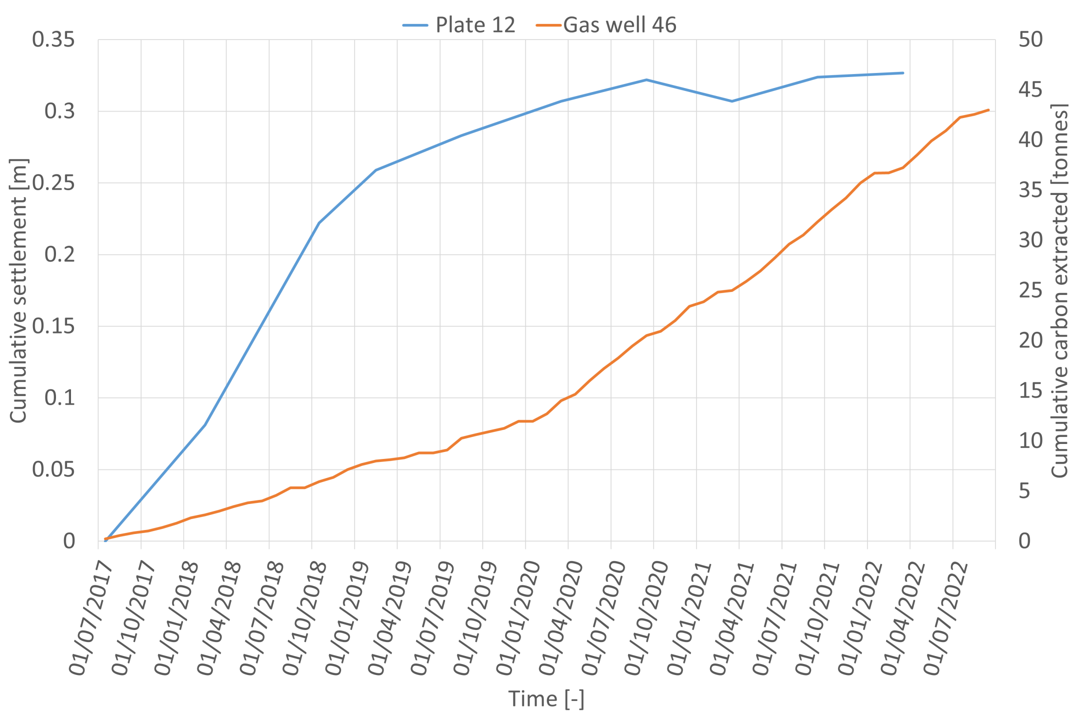

Figure C.7: Cumulative extracted carbon mass and GNSS settlement at plate 12 and well 46 between August 2017 and March 2022. Settlement in meters, carbon mass in tonnes.

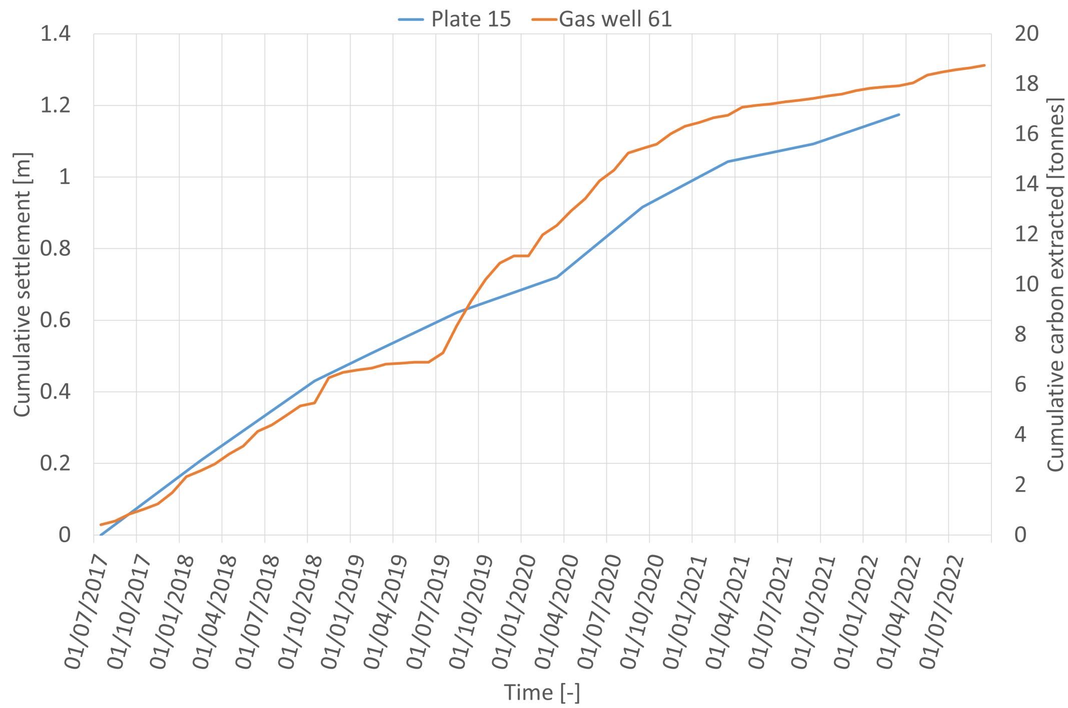

Figure C.8: Cumulative extracted carbon mass and GNSS settlement at plate 15 and well 61 between August 2017 and March 2022. Settlement in meters, carbon mass in tonnes.

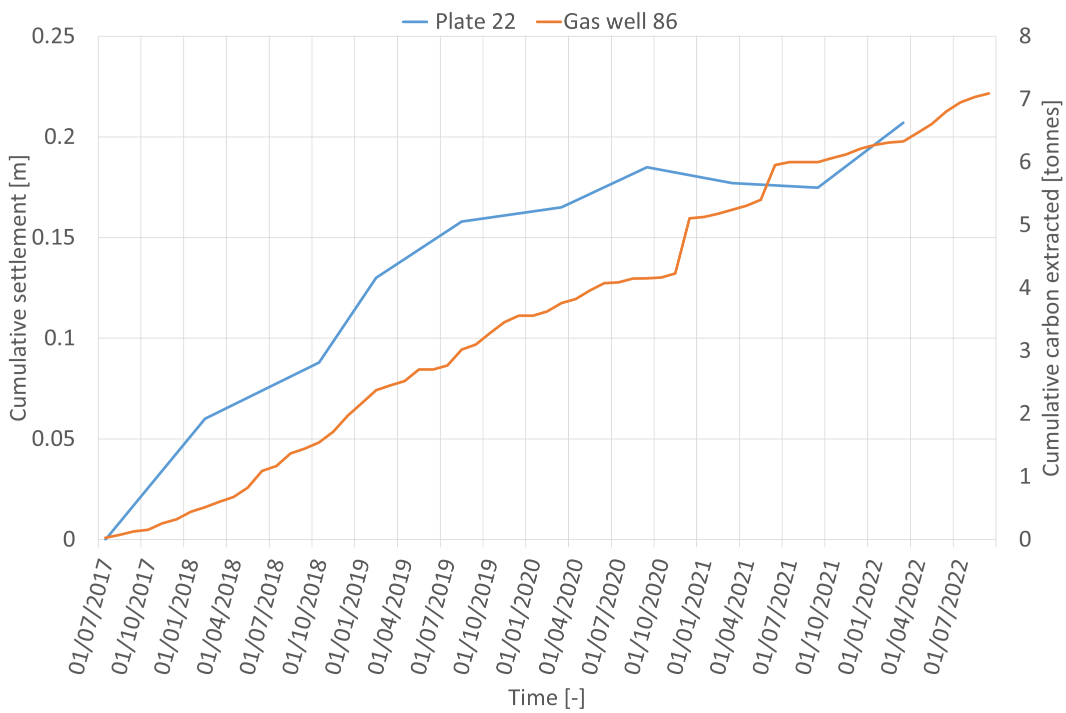

Figure C.9: Cumulative extracted carbon mass and GNSS settlement at plate 22 and well 86 between August 2017 and March 2022. Settlement in meters, carbon mass in tonnes.

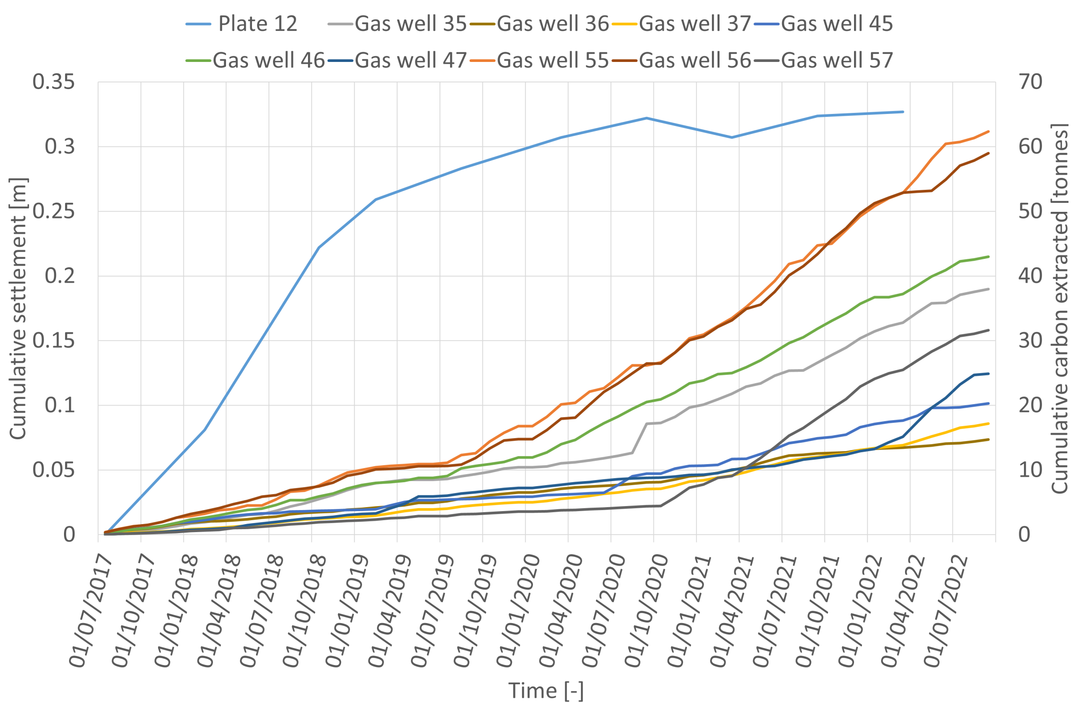

Figure C.10: Cumulative extracted carbon mass and GNSS settlement at plate 22 and the 9 closest wells between August 2017 and March 2022. Settlement in meters, carbon mass in tonnes.

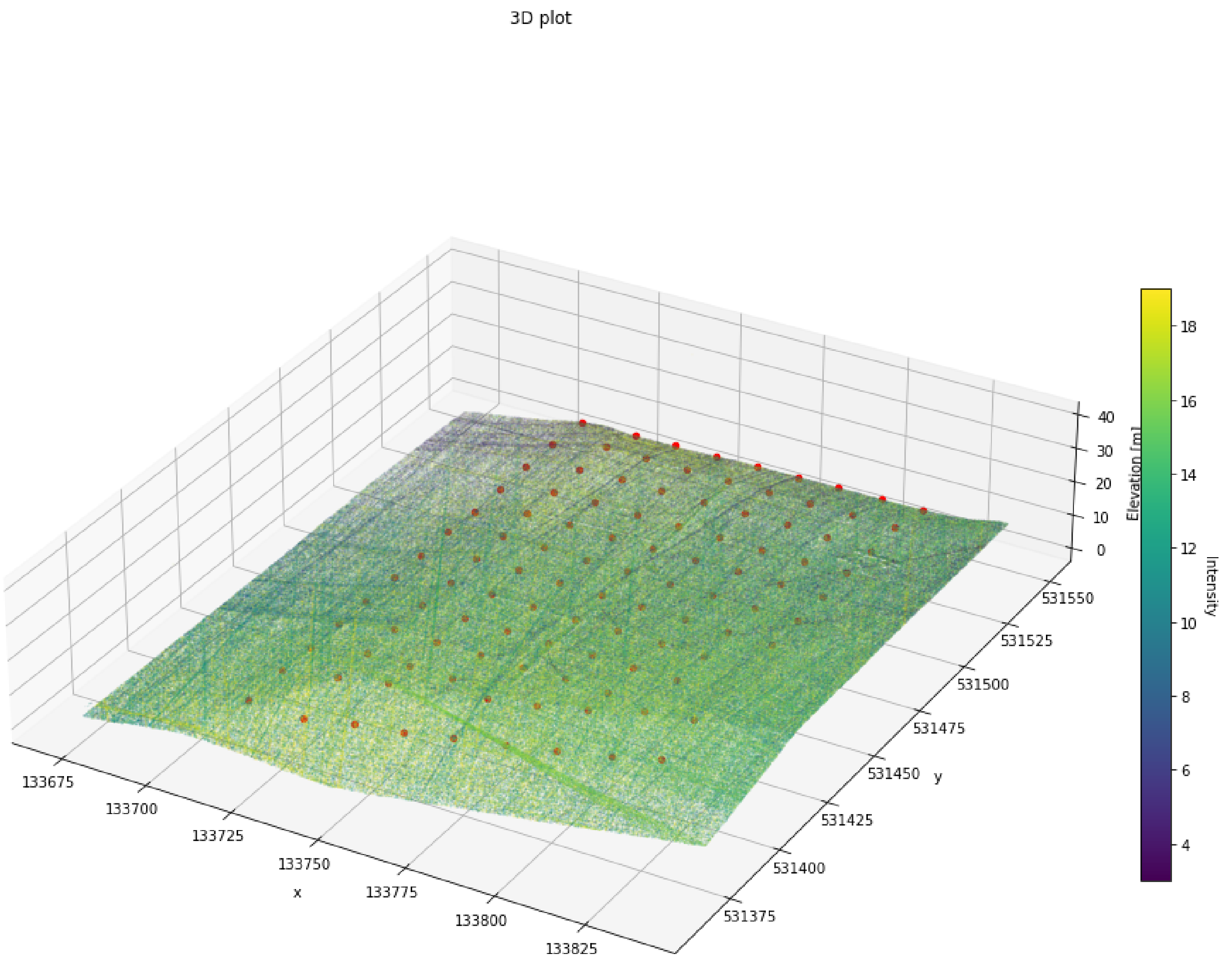

Figure C.11: ALS March 2022 point cloud plotted in 3D in Python, the red dots represent the gas wells.

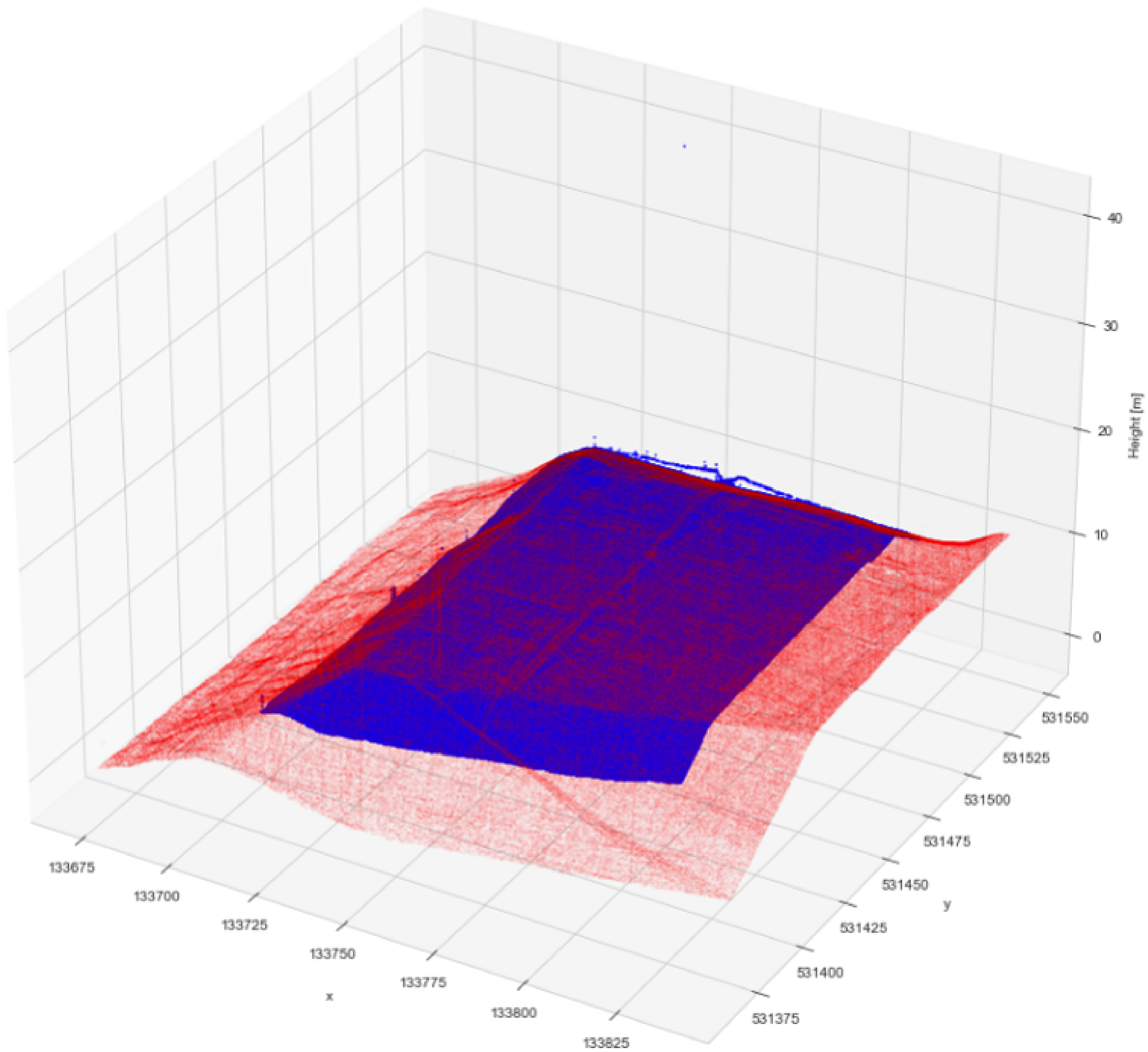

Figure C.12: Cropped ALS LiDAR data in blue, original data in red.

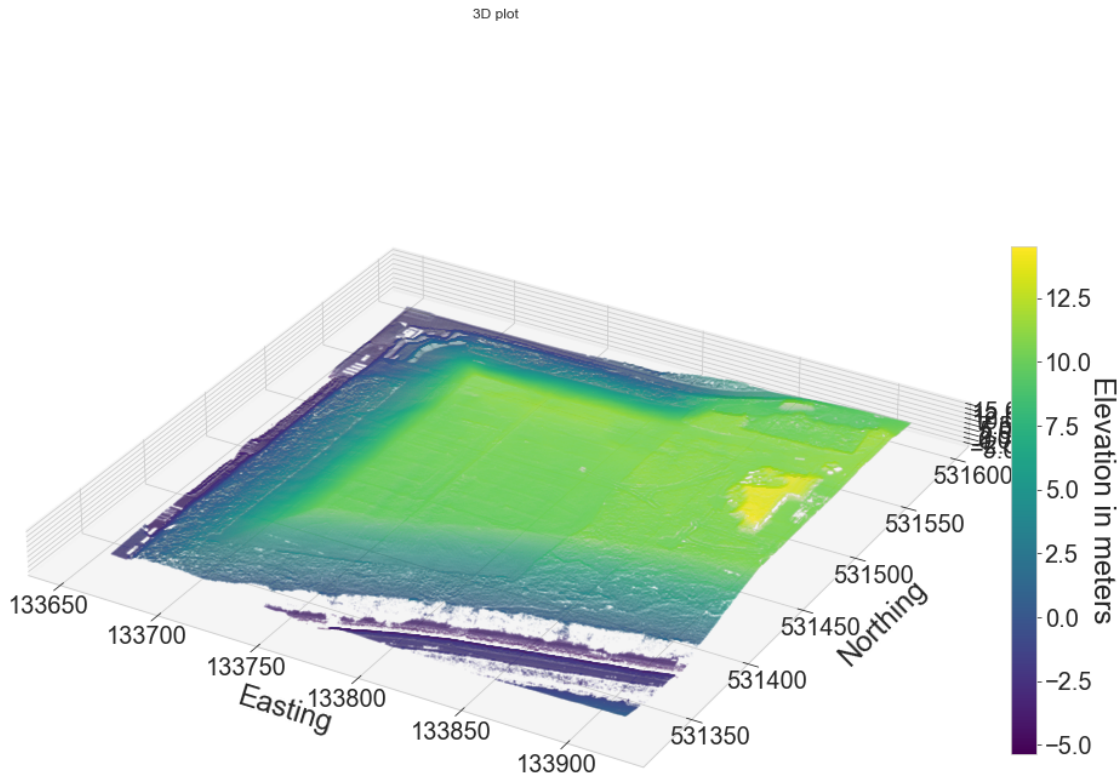

Figure C.13: ALS March M3C2 2022 point cloud plotted in 3D in Python.

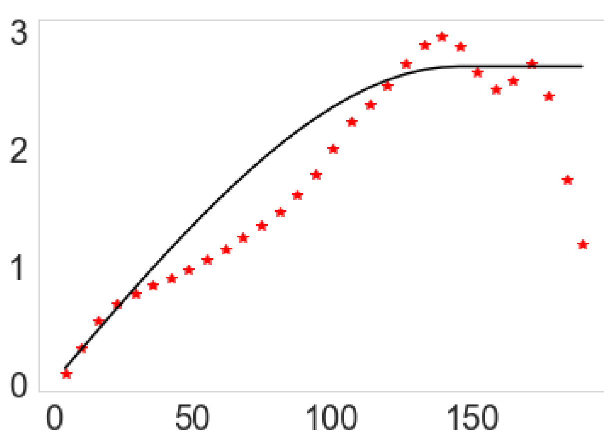

Figure C.14: Example of variogram from ALS M3C2 settlement data, used for Ordinary Kriging interpolation. Variance [-] on vertical axis and distance [m] on horizontal axis.